

Numerical modeling of dynamically manipulated wind turbine wakes

Muscari, C.

DOI

[10.4233/uuid:602af271-f14f-48c4-b92c-cd684679465b](https://doi.org/10.4233/uuid:602af271-f14f-48c4-b92c-cd684679465b)

Publication date

2025

Document Version

Final published version

Citation (APA)

Muscari, C. (2025). *Numerical modeling of dynamically manipulated wind turbine wakes*. [Dissertation (TU Delft), Delft University of Technology, Politecnico di Milano]. <https://doi.org/10.4233/uuid:602af271-f14f-48c4-b92c-cd684679465b>

Important note

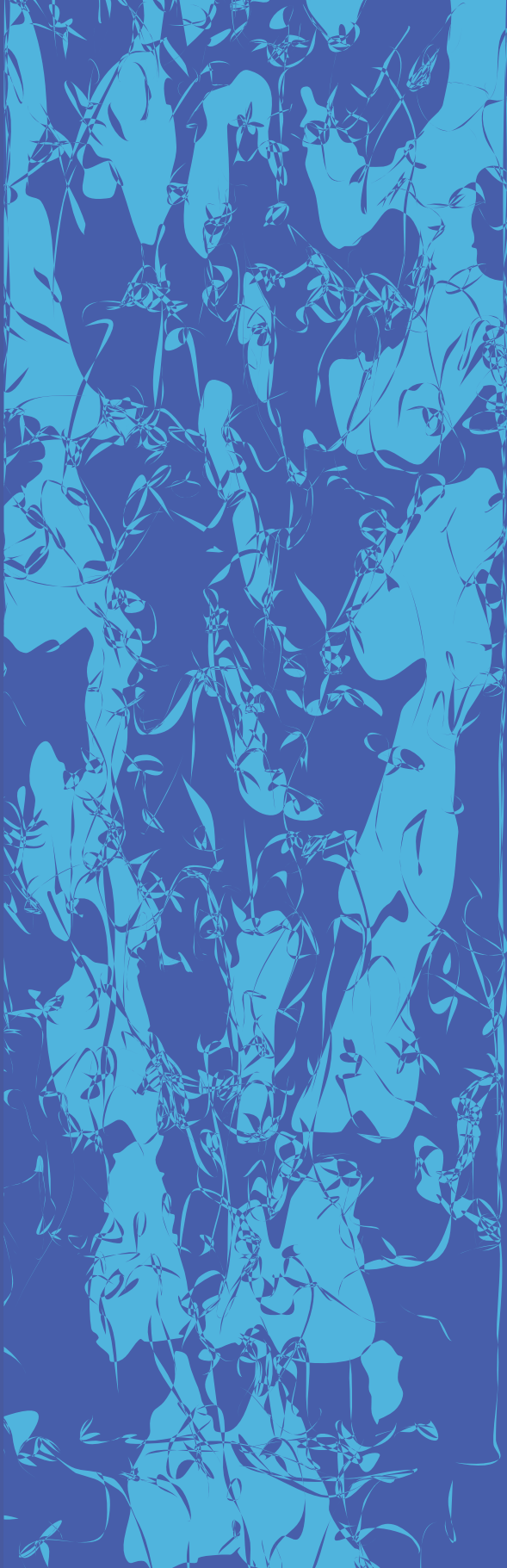
To cite this publication, please use the final published version (if applicable).
Please check the document version above.

Copyright

Other than for strictly personal use, it is not permitted to download, forward or distribute the text or part of it, without the consent of the author(s) and/or copyright holder(s), unless the work is under an open content license such as Creative Commons.

Takedown policy

Please contact us and provide details if you believe this document breaches copyrights.
We will remove access to the work immediately and investigate your claim.



Numerical Modeling of dynamically manipulated wind turbine wakes

Claudia Muscari

Propositions

accompanying the dissertation

NUMERICAL MODELING OF DYNAMICALLY MANIPULATED WIND TURBINE WAKES

by

Muscari CLAUDIA

1. Current CFD-CSD frameworks, which are predominantly based on tightly coupled iterative solvers, are not efficient enough to justify their use in wind turbine power-maximization control research. [Chapter 2 of this thesis]
2. The actuator line model has revolutionized the numerical modeling of wind turbines. However, to fully leverage its potential, we should incorporate the physical effects of the smearing function. This will ultimately make the difference between trustworthy and useless results. [Chapter 3 of this thesis]
3. Although wakes are high-dimensional and nonlinear dynamical systems, for wind farm wake mixing techniques, their dynamics can be described by low-dimensional linear models with acceptable accuracy. [Chapters 4 and 5 of this thesis]
4. The optimum pitching frequency for the helix depends on the inflow conditions and on the positioning of downstream turbines.[Chapter 5 of this thesis].
5. To move past political hesitation driven by re-election concerns, independent agencies should have the authority to enforce essential climate policies, free from short-term political pressures.
6. In 1967 Ronald Reagan said that tax-payers should not be subsidizing intellectual curiosity. To protect academic freedom from the influence of corporations that prioritize profit over social welfare, I propose they should.
7. Merit is a myth: we like to pretend class, race, and gender don't matter.
8. Policies aimed at increasing diversity in the workplace, such as quotas, have been tested for decades now. Not only we now know that they work, but also why and how. Any further step should have this data as a starting point.
9. Psychological help services provided in the workplace often benefit the employer by helping employees cope with unacceptable conditions. Universities are no exception.
10. The most accurate representation of what life looks like for PhD candidates comes from memes and it is not pretty.

These propositions are regarded as opposable and defensible, and have been approved as such by the promoters prof. dr. ir. J.W. van Wingerden, prof. dr. ir. A. Zasso, prof. dr. ir. A. Viré and prof. dr. ir. P. Schito

NUMERICAL MODELING OF DYNAMICALLY MANIPULATED WIND TURBINE WAKES

NUMERICAL MODELING OF DYNAMICALLY MANIPULATED WIND TURBINE WAKES

Dissertation

for the purpose of obtaining the degree of doctor
at Delft University of Technology
by the authority of the Rector Magnificus prof. dr. ir. T.H.J.J. van der Hagen,
chair of the Board for Doctorates,
to be defended publicly on
Monday 6 October 2025 at 10:00

by

Claudia MUSCARI

Master of Science in Energy Engineering,
Politecnico di Milano, Italy
born in Soriano Calabro, Italy.

This dissertation has been approved by the candidate's promotor.

Composition of the doctoral committee:

Rector Magnificus,	chairperson
Prof. dr. ir. J.W. van Wingerden,	Delft University of Technology, promotor
Prof. dr. ir. A.C. Viré,	Delft University of Technology, promotor
Prof. dr. ir. A. Zasso,	Politecnico di Milano, Italy, promotor
Prof. dr. ir. P. Schito,	Politecnico di Milano, Italy, promotor

Independent members:

Prof. dr. A. Bianchini,	University of Florence, Italy
Dr. ir. S.P. Mulders,	Delft University of Technology
Prof. dr. S.J. Watson,	Delft University of Technology
Prof. dr. D.A. von Terzi,	Delft University of Technology
Dr. R. Ferrari	Delft University of Technology, reserve member

The doctoral research has been carried out within the framework of the dual doctoral degree agreement between Politecnico di Milano, Italy and Delft University of Technology, the Netherlands



Keywords: Wind Farms, Wake modeling, Actuator line model, helix, DMD

Cover by: Claudia Muscari

An electronic version of this dissertation is available at
<http://repository.tudelft.nl/>.

'Alle volte uno si crede incompleto ed è soltanto giovane '

Italo Calvino

INDEX

Summary

Samenvatting

1	Introduction	
1.1	Energy Scenario	2
1.2	Wind Turbines' Wakes	4
1.3	Wind Farm Control	5
1.4	Modelling for wind farm control	8
1.5	Thesis objectives and outline	11
2	The influence of wind blade flexibility on the wake	
2.1	Introduction	16
2.2	Methods	17
2.3	The Model Turbine and the Experimental Data	20
2.4	Numerical Setup	22
2.5	Results	28
2.6	Conclusions	38
3	The EVM: An improved approach to velocity sampling in actuator line models	
3.1	Introduction	40
3.2	Methods and Tools	42
3.3	Numerical Setup	45
3.4	Results	48
3.5	Conclusions	57
4	A data-driven comparison of the pulse and the helix	
4.1	Introduction	60
4.2	Methods	61
4.3	Simulation	64
4.4	Analysis	65
4.5	Conclusions	69
5	An analysis of the helix wake and its properties via dynamic mode decomposition	
5.1	Introduction	72
5.2	Methodology	74
5.3	Numerical environment	76
5.4	Results	80
5.5	Conclusions	87
6	Conclusions and Recommendations	
6.1	Conclusions	90
6.2	Future works recommendations	91

Bibliography

Acronyms

Curriculum Vitæ

List of Publications

Acknowledgments

SUMMARY

Wind plays a fundamental role in the energy transition and, by 2050, is expected to be the main energy source in the European Union. Trends in the field include increasing the dimension of the rotors and clustering into wind farms. The area of fluid downstream of a wind turbine is called a wake and is mainly characterized by a wind velocity deficit and increased turbulence intensity. Therefore, clustering wind turbines calls for an effort to better understand wake dynamics and account for wake interaction in order to maximize the power production and the turbines' lifetime.

Wind Farm control is the branch of wind energy that pursues these objectives by coordinating the turbines' actions. Shifting from greedy control (operating each turbine at its individual optimum) to more sophisticated strategies significantly increases the energy yield and reduces structural loads.

This thesis focuses on dynamic induction control for power maximization.

Dynamic induction control consists of periodically varying the induction factor, generally by means of blade pitch actuation, in order to enhance the mixing in the wake and accelerate the velocity recovery. The two techniques currently dominating the field are the pulse and the helix. They rely on sinusoidal excitations of the blades' collective and individual pitch, respectively. Despite a large number of numerical and experimental tests and, as of late, linear stability analyses, incomplete knowledge of the physics of manipulated wakes prevents the community from embedding dynamic induction control into analytical control-oriented models. This thesis addresses this gap. The thesis objective was formalized as:

"Development of numerical methods reliably modeling wind turbine wake dynamics as a tool for optimized solutions of wind farm control."

The research work was conducted over two main phases: preparation of the numerical framework and characterization of dynamically manipulated wind turbine wakes. The first sub-question related to the development part was:

When does the accuracy obtainable by coupling high fidelity computational fluid dynamics and computational structural dynamics models justify the increased computational cost?

This question is motivated by the trend of increasing rotor dimensions: the bigger the blades become, the higher their flexibility and its effect on the aero-servo-elastic performance of the rotor. To answer the question, we tested the coupling between the state-of-the-art high-fidelity framework for wind turbines and farms aerodynamics SOWFA and the linear structural model from the FAST suite, ElastoDyn. The object of the simulations was a wind tunnel scaled model (1:75) of the DTU 10MW turbine. The reference data was obtained during the UNAFLOW project (2018). Experiments were carried out in the PoliMi Wind Tunnel boundary layer section with different operational parameters. The study did not result in general guidelines but gave a good indication of whether or not we needed to account for flexibility effects in the next research steps. In particular, we concluded that if tip deflections remain under 4.2% of the blade length, flexibility has no noticeable effect on the wake description. This notion guided the first methodological choice not to consider blade flexibility in the following. A further step in the definition of the framework was to focus on the turbine model and ascertain its capability to deliver reliable results. The actuator line model has been the go-to approach for wind turbines and (small) wind farm simulations in academic contexts for more than a decade.

The second research question in this thesis was:

What are the limitations of actuator line models for wind turbines, and how can we address them?

The motivation for asking and answering this question is that using different actuator line models and, sometimes, even different users using the same model can lead to very different results. No consensus has been reached over important issues, such as evaluating the free-stream velocity and choosing the width of the smearing function used to project volume forces into the computational domain. The thesis discusses how these issues are connected and proposes an alternative approach to velocity sampling. From comparison with the pre-existing methods, the conclusion is that the results obtainable with our approach are more independent of the smearing function width and better match a reference power curve. However, the thrust curve, which, for its connection to the wake, is very important for wind farm applications, is not as closely matched. A more high-level conclusion is that, even if the actuator line guarantees the best trade-off between accuracy and computational efficiency for the simulation of wind turbine wakes, its formulation should be revised at its core. The insight coming from the development phase converged into the subsequent characterization study. However confident we can be in our high-fidelity computational framework, it is clear that it cannot be directly used for the optimization of wind farm control strategies as this should, ideally, happen in real-time.

This motivates the final question which is:

Can we leverage the amount of data obtainable from the high fidelity simulations to characterize manipulated wake behavior and embed this knowledge into control-oriented models?

High-fidelity actuator line simulations were ran in both idealized and realistic atmospheric conditions and with both standard turbine-level control and dynamic induction control. Wake velocity and pressure data was collected over a significant time range to produce a proper data base. The data was organised into snapshot matrices and fed to a dynamic mode decomposition (DMD) algorithm. DMD splits the data into purely spatial modes, scalar amplitudes, and purely temporal signals. This makes it suitable for the identification of dominant frequencies. Its applications to fluid dynamics in general and wind energy, in particular, include diagnostic and future state prediction.

With this approach, a reduced order model is obtained, which, for the analysed cases, is able to reconstruct the full flow field with a maximum 9% relative root mean square error, with only two modes. This is sufficient to answer positively to the formulated research question, but the analysis of the derived wake dynamic modes leads to the following additional conclusions.

As in previous studies, the helix proves to be a more effective power maximization technology than the pulse (given the same signal parameters), particularly in its counter clock-wise variant. The dominant modes are characterized by a frequency equal to the pitch excitation one and its harmonics. Temporal amplitude and spatial decay of the helix modes are a function of turbulence intensity. Using the helix always leads to farm power gains for neutral stability of the atmospheric boundary layer and turbulence intensity levels that are representative of offshore operation. The optimal frequency is in a distinct Strouhal number range (0.25 to 0.4) but ultimately depends on both the inflow and the considered downstream distance. The thesis, finally, discusses a few hypothesis on how the helix triggers wake destabilization.

To sum up, this thesis contributes to the state of the art of wind farm control by providing a reliable (stable and accurate) numerical framework for high-fidelity simulations and advancing the understanding of dynamic induction control techniques such as the helix and the pulse.

SAMENVATTING

Wind speelt een fundamentele rol in de energietransitie, en zal naar verwachting in 2050 de belangrijkste energiebron in de Europese Unie zijn. Trends op het gebied van windenergie zijn onder andere het vergroten van de afmetingen van de turbines en het clusteren ervan in windparken. Het gebied stroomafwaarts van een windturbine wordt het zog genoemd, en wordt voornamelijk gekenmerkt door een verminderde windsnelheid en een verhoogde turbulentie. Het clusteren van windturbines vraagt daarom om een goed begrip van de zogdynamica en om rekening te houden met zoginteracties, om zo de energieproductie en de levensduur van de turbines te maximaliseren.

Het regelen van windparken is de tak van windenergie die deze doelstellingen nastreeft, door de operatie van de turbines te coördineren. Door over te stappen van greedy control (waarbij elke turbine op zijn individuele optimum werkt) naar geavanceerdere strategieën wordt de energieopbrengst aanzienlijk verhoogd en de mechanische belasting van de turbines verlaagd.

Dit proefschrift richt zich op het dynamisch regelen van de inductie, om zo het vermogen van een windpark te optimaliseren. Dynamische regeling van de inductie bestaat uit het periodiek variëren van de inductiefactor, over het algemeen door de invalshoek van de turbinebladen te regelen, om de menging in het zog te verbeteren en zo de verminderde windsnelheid versneld te herstellen. De twee technieken die momenteel het veld domineren zijn de pulse en de helix. Deze berusten op sinusvormige aansturing van respectievelijk de collectieve of de individuele invalshoek van de turbinebladen. Ondanks een groot aantal numerieke en experimentele onderzoeken en, sinds kort, lineaire stabiliteitsanalyses, verhindert de beperkte kennis van de fysica van deze zogmanipulaties de vakgemeenschap om dynamische inductieregeling in te bedden in analytische modellen die toegepast kunnen worden in regeltechniek. Deze dissertatie pakt dit hiaat aan. De doelstelling van deze dissertatie is geformaliseerd als:

“Ontwikkeling van numerieke methoden die op betrouwbare wijze de zogdynamica van windturbines modelleren als hulpmiddel voor het optimaal regelen van windparken.”

Het onderzoek is uitgevoerd in twee fasen: de ontwikkeling van een numeriek raamwerk en de karakterisering van dynamisch gemanipuleerde windturbinezoggen. De eerste deelvraag met betrekking tot het ontwikkelingsgedeelte was:

Wanneer rechtvaardigt de nauwkeurigheid die verkregen kan worden door het koppelen van high-fidelity numerieke stromingsleer en numerieke mechanicamodellen de benodigde rekenkracht?

Deze vraag is ingegeven door de trend van toenemende rotorafmetingen: hoe groter de bladen worden, hoe groter hun flexibiliteit en het effect daarvan op het aero-servo-elastische gedrag van de rotor. Om deze vraag te beantwoorden hebben we de koppeling getest tussen het state-of-the-art high-fidelity raamwerk voor windturbines en aerodynamica van windparken SOWFA en het lineaire constructiemodel uit de FAST suite, ElastoDyn. Deze simulaties betroffen een geschaald windtunnelmodel (1:75) van de DTU 10MW turbine. De referentiegegevens zijn afkomstig van het UNAFLOW-project (2018). Deze experimenten zijn uitgevoerd in de atmosferische grenslaagtunnel van PoliMi met verschillende operationele parameters. Het onderzoek heeft geen algemene richtlijnen opgeleverd, maar gaf wel een goede indicatie of we in de vervolgstappen rekening moesten houden met het effect van elastische deformaties. We konden met name concluderen dat als de doorbuiging van de tip onder 4,2% van de bladlengte blijft, flexibiliteit geen merkbaar effect heeft op het

zog. Deze conclusie vormde de leidraad voor de eerste methodologische keuze, om geen rekening te houden met flexibiliteit van de bladen. De volgende stap in de definitie van het numerieke raamwerk was om te focussen op het model van de windturbine, en na te gaan of dit model in staat is om betrouwbare resultaten te produceren. Het actuator line model is al meer dan tien jaar de meest gebruikte methode voor de simulatie van windturbines en van (kleine) windparken in academische toepassingen. De tweede onderzoeksvraag in dit proefschrift was:

Wat zijn de beperkingen van actuator line modellen voor windturbines, en hoe kunnen we deze aanpakken?

De motivatie voor het stellen en beantwoorden van deze vraag is dat het gebruik van verschillende actuator line modellen, en soms zelfs het gebruik van hetzelfde model door verschillende gebruikers, kan leiden tot zeer verschillende resultaten. Er is geen consensus over belangrijke configuraties, zoals het evalueren van de snelheid van de vrije luchtstroom en het kiezen van de breedte van de verdelingsfunctie die gebruikt wordt om de krachten op luchtstroming te projecteren. Deze dissertatie bespreekt hoe deze kwesties met elkaar samenhangen en stelt een alternatieve methode voor om de snelheid te evalueren. Uit vergelijking met de reeds bestaande technieken is de conclusie dat de resultaten die met onze alternatieve methode worden verkregen onafhankelijker zijn van de breedte van de verdelingsfunctie en beter overeenkomen met een referentie vermogenscurve. De stuwkrachtcurve, die vanwege de verbinding met het zog erg belangrijk is voor windparktoepassingen, komt echter minder goed overeen. Een algemene conclusie is dat, zelfs als het actuator line model de beste afweging tussen nauwkeurigheid en rekeninefficiëntie garandeert voor de simulatie van windturbinezoggen, de formulering ervan in de kern moet worden herzien. De inzichten die uit deze ontwikkelingsfase voortkwamen, gingen over in de daaropvolgende karakteriseringsstudie. Hoe zeker we ook kunnen zijn van ons high-fidelity raamwerk, het is duidelijk dat het niet direct gebruikt kan worden voor de optimalisatie van regelstrategieën voor windparken, omdat dit idealiter in real-time zou moeten gebeuren.

Dit motiveert de laatste vraag:

Kunnen we gebruik maken van de gedetailleerde gegevens die verkregen kunnen worden met high-fidelity simulaties om gemanipuleerd zoggedrag te karakteriseren en deze kennis in te bedden in modellen die toegepast kunnen worden in regeltechniek?

High-fidelity actuator line simulaties zijn uitgevoerd in zowel geïdealiseerde als realistische atmosferische omstandigheden en met zowel standaardregeling op turbineniveau als dynamische inductieregeling. Gegevens over de snelheid en druk in het zog zijn verzameld over een aanzienlijk tijdsbestek om een adequate database op te bouwen. De gegevens zijn georganiseerd in snapshotmatrices en ingevoerd in een algoritme voor dynamic mode decomposition (DMD). DMD splitst de gegevens op in ruimtelijke modes, scalaire amplitudes en signalen als functie van tijd. Dit maakt het geschikt voor de identificatie van dominante frequenties. De toepassingen in stromingsleer in het algemeen, en windenergie in het bijzonder, omvatten diagnostiek en voorspelling van toekomstige toestanden.

Op deze manier wordt een gereduceerd model verkregen, dat met slechts twee modes in staat is voor de geanalyseerde gevallen het volledige stromingsveld te reconstrueren, met een relatieve RMS fout van maximaal 9%. Dit is voldoende om de onderzoeksvraag positief te beantwoorden, maar de analyse van de afgeleide dynamische zogmodes leidt tot de volgende aanvullende conclusies.

Net als in eerdere studies blijkt de helix een effectievere technologie voor het maximaliseren van het vermogen dan de pulse (gegeven dezelfde signaalparameters), vooral in de tegen de klok in gaande variant. De dominante modes worden gekarakteriseerd door een frequentie die gelijk is aan die van de excitatie van de invalshoek en de hogere harmonischen daarvan. De tijdsafhankelijke ontwikkeling van de amplitudes en het ruimtelijke verval van modes zijn afhankelijk van de

turbulentie-intensiteit. Het gebruik van de helix leidt altijd tot vermogenswinst op parkniveau, voor een neutrale stabiliteit van de atmosferische grenslaag en turbulentie-intensiteitsniveaus die representatief zijn voor offshore-operaties. De optimale frequentie ligt in een specifieke range van Strouhalgetallen (0,25 tot 0,4), maar is afhankelijk van zowel de instroom als van de beschouwde stroomafwaartse afstand. Tot slot worden in dit proefschrift enkele hypothesen besproken over hoe de helix het zog destabiliseert.

Samenvattend draagt dit proefschrift bij aan de huidige state-of-the-art op het gebied van windparkregeling door een betrouwbaar raamwerk te bieden voor high-fidelity simulaties en door het bevorderen van het begrip van dynamische inductie-regeltechnieken zoals de helix en de pulse.

1

INTRODUCTION

'I believe that someone who lacks a delusional sense of significance will wilt in the face of repeated experiences of multiple small failures and rare successes, the fate of most researchers.'

Daniel Kahneman

This introduction presents the concepts necessary to understand the main objectives of the thesis. After presenting the role of wind in the current energy scenario, we characterize wind turbine wakes and introduce the field of wind farm control, both of which will be central to the rest of the dissertation. After detailing the basics of atmospheric boundary layer aerodynamics, we complete the introduction by clarifying the thesis' goals.

1.1 ENERGY SCENARIO

Climate scientists have shown that humans are responsible for virtually all global warming over the last 200 years [1]. The catastrophic consequences are before everyone's eyes: intense droughts, water scarcity, severe fires, rising sea levels, flooding, melting polar ice, unusually intense storms, and increased endangerment of biodiversity, and this is just the beginning.

Although EU greenhouse gas net emissions decreased by around 3% in 2022, continuing the overall downward trend of the past 30 years, member states are still far from reaching the EU's targets for 2030 and 2050. The states are required to periodically deliver national energy and climate progress reports (NECPRs), which are summarized in a State of the Energy Union Report. The first of such reports came out this year [2]. Its main take is that the pace of emissions reduction needs to increase much faster (around three times the pace maintained in the last decade) to achieve a 55% emissions reduction by the end of this decade.

Energy production from renewable sources is playing and will continue to play a big role in attaining this ambitious goal. In 2021, the EU reached a share of 21.8% of renewable energy consumption. In 2020 the share was slightly higher, 22%, but this can be explained with a higher energy consumption in correspondence to the lifting of COVID restrictions. Focusing on electricity generation, the most important source remains hydro, with 348 TWh in 2021, followed by onshore wind, solar, solid biomass, biogas, and offshore wind.

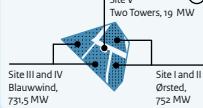
Wind is a clean and abundant resource, and the technology to harness it is mature and competitive. The wind energy industry is the fastest-growing one in the renewables landscape, with big, ambitious projects being developed all over the globe. The objective is to reach at least 260 GW of offshore wind energy by 2050. The Dutch government aims at 21 GW worth of offshore wind farms in operation by 2030 [3], covering 75% of the current electricity consumption in the Netherlands. Figure 1 is a representation of the government's roadmap. In 2020, the first turbines of the 731 MW Borssele III wind farm were connected to the electricity network. To give an idea of the investment that this plan entails, the Prinses Amalia wind farm (visible in Figure 1 as the small blue dot in the Hollandse Kust farm) cost approximately 390 million euros.

For wind energy technology to fulfill the prominent role it's expected to have in the coming decades, turbines should become more efficient, cost less, and last longer, and wind resource exploitation should be optimized. This is more easily said than done since, once you broaden the focus, the problem becomes complex and needs a multi-disciplinary approach, especially when it comes to offshore applications and wind farms. For this reason, a wind energy scientist can be an aerodynamicist but also a meteorologist, a control engineer, an acoustic and an electrical one, to mention a few.

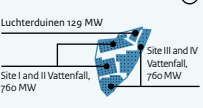
Although wind is abundant, favorable locations for wind turbines are not. A proper location should not only have strong, uniform wind but also be far enough from inhabited centers and respond to logistic necessities related to transport, installation, maintenance, and connection to the grid. In this context, the strategic arrangement and clustering of wind turbines into farms play a pivotal role in maximizing efficiency. Once we cluster the turbines, it is vital to account for wake interaction. In fact, when a turbine is positioned downstream with respect to another, it will extract less energy because of the wind velocity deficit and experience higher loads because of increased flow turbulence.

Offshore Wind Energy Roadmap 21 GW

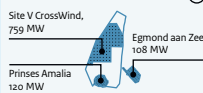
Borssele



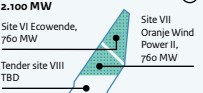
Hollandse Kust Zuid



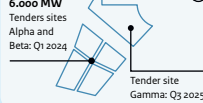
Hollandse Kust Noord



Hollandse Kust West



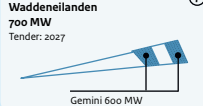
IJmuiden Ver



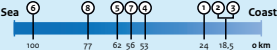
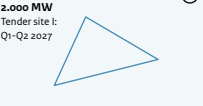
Nedenwiek



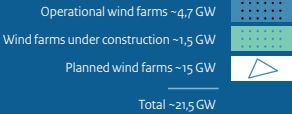
Ten noorden van de Waddeneilanden



Doordewind



Legend



April 2024

Figure 1: Overview of the locations of wind farms to in the Dutch Offshore Wind Energy Roadmap ([4])

1.2 WIND TURBINES' WAKES

The extraction of energy from wind across a turbine rotor produces an aerodynamic wake region downstream of the rotor. Figure 2 is the picture of the Horns Rev 2 wind farm in Denmark. The wakes of the turbines are clearly visible. This offshore wind farm was inaugurated in 2009, and, at the time, it was the largest in the world.



Figure 2: Horns Rev 2, offshore wind farm in the North Sea, picture by Henrik Krogh

We can define wakes as high-dimensional, nonlinear, dynamical systems characterized by multi-scale phenomena in both space and time. The wake region is generally associated with the following characteristics:

- velocity deficit (the rotor slows the wind down);
- pressure differential (the energy extraction at the rotor can be seen as a pressure drop);
- expanding area (the wake area on a plane parallel to the rotor grows with the streamwise position of the plan);
- rotation of the wake field (the wake can be seen as a complex vortex system);
- increased turbulence (the rotor poses an obstacle to the flow and increases its turbulence).

When we look at the wake, a distinction can be made between near-wake (up to two diameters downstream) and far-wake regions. In the near wake, it is still possible to discriminate the rotor properties; the far wake dynamics, instead, is mostly dominated by convection and turbulent diffusion, and its study is relevant mostly in wind farm situations.

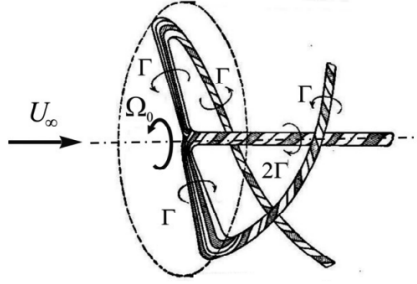


Figure 3: Joukowski's vortex model of a propeller based on a rotating horse-shoe vortex

Another way to look at wakes is as a complex system of helical vortices: two rotating horseshoe vortices generated at the tip and straight root vortices [5]. A representation borrowed from Joukowski's 1912 article is shown in Figure 3. Additionally, a trailing vortex sheet is generated by the circulation distribution variation along the blade span. Since wake flow has higher turbulence and lower energy content (because of the velocity deficit), when a turbine is fully or partially in the wake of another, it will produce less power and undergo additional loads.

1.3 WIND FARM CONTROL

When wind turbines are installed in clusters, because of wake interaction, the optimal strategy for both power production maximization and load minimization generally does not coincide with optimizing individual turbine output. Wind farm control (WFC) is the branch of wind energy that abandons this individual (greedy) approach to see the farm as a whole.

The desired behavior of the resulting system is, in general, a minimization of the levelised cost of energy (LCoE). From a control perspective, two - often conflicting - objectives can be individuated: load mitigation and power maximization. This thesis focuses on the latter.

Power maximization control in wind farms is a set of strategies and techniques aimed at optimizing the energy production of a wind farm by adjusting the operation of individual wind turbines or the entire farm as a whole. The primary goal of power maximization control is to capture as much wind energy as possible while ensuring the safe and efficient operation of the wind turbines. From a 2020 expert elicitation [6], three distinct strategies emerge.

Wake Steering

Wake steering aims at reducing or eliminating the operation of downstream turbines in the wake of upstream ones. It can be yaw-based or tilt-based, but yaw-based wake steering is significantly more popular. It is based on the fact that changing the yaw angle of the upstream turbine changes the direction and magnitude of the thrust force. As a consequence, the wake direction also changes, and the interaction with the downstream turbines is reduced. It made a first appearance in Clayton and Filby [7], was then extensively tested numerically [8, 9], on model turbines [10] and in the field [11] and is now officially on the market [12]. Figure 4 gives a simplified representation of how the technique works.

Static Induction Control

Axial induction control consists of derating upstream turbines to reduce loading and increase power production for downstream ones. First references to this technique date back to the eighties [13, 14].

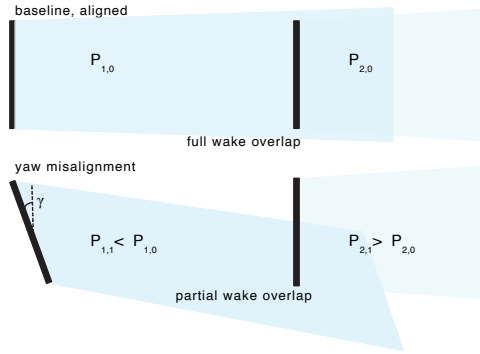


Figure 4: Simplified representation of how static yaw of the upstream wind turbine can increase the combined power gain

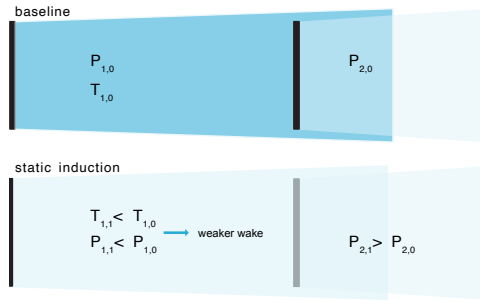


Figure 5: Simplified representation of how static induction control increases the power available to the downstream turbine by de-rating the upstream one.

The derating is usually achieved by increasing the pitch or reducing the tip-speed ratio (TSR) of the upstream turbines, for example acting on torque. This reduces the power and the magnitude of rotor thrust which, in turn, reduces the axial induction factor and increases the wake velocity. Figure 5 gives a simplified representation of how the technique works. While early results, coming from simplified wake models, were very promising [15, 16], Campagnolo et al., among others, found poor gains in dedicated wind tunnel tests [17]. In these cases, because of how strongly the gains depend on the specific power curve, it could be argued that a scaled model is not representative. However, in 2021 a full-scale field experiment was performed at Sedini wind farm in Italy, showing gains within statistical uncertainty [18].

Dynamic Induction Control

In recent years, strategies involving time-varying control inputs have started gaining interest from the wind energy community. The main goal of these strategies is to promote the mixing of the wake with the surrounding airflow so that the inflow to the downstream turbines has a higher energy content. A seminal paper by Goit and Meyers [19] presents a procedure for optimizing thrust set points over time and its results and is the basis for the development of two relevant dynamic induction control (DIC) techniques known as the pulse [20] and the helix [21].

With the pulse, [22], wake mixing is induced by superimposing a sinusoidal signal on a wind turbine's collective blade pitch angles. The characterization of the excitation signal is usually done in terms of Strouhal number, which is defined as follows:

$$St = \frac{f_e D}{U_\infty} \quad (1)$$

where f_e is the excitation frequency, D is the diameter and U_∞ is the free-stream velocity.

The helix [21] uses individual pitch control (IPC) to achieve the same wake recovery effects as the pulse, with lower fluctuations in power production and wake velocity. Instead of inducing an early wake breakdown by dynamically varying the thrust magnitude, IPC acts on its direction. This way, it imposes yaw and tilt moments on the rotor to force wake meandering [23]. These moments are excited with a low frequency sinusoidal signal with a certain phase offset, resulting in a moment rotating with a $1/f_e$ period. A multi-blade coordinate (MBC) transformation projects the blade loads in a non-rotating reference frame. The resulting velocity field is helicoidal, hence the name of the strategy. If the phase offset between tilt and yaw angles is equal to $\pi/2$, the helix rotates in counter clock-wise (CCW) direction; if it is equal to $3/2\pi$, the helix rotates in clock-wise (CW) direction. The preliminary tests in Frederik et al. [21] show that the CCW-helix leads to faster wake recovery than CW-helix.

Control strategies based on a dynamically varying induction factor proved to increase the power production of small to medium-sized wind farms by enhancing wake mixing. With the unbounded optimal signal found in Goit and Meyers [19], DIC was able, in numerical simulations, to increase power gains up to 21% with respect to greedy control.

Since 2015, the pulse and the helix have been tested numerically at all fidelity levels except for fully resolved computational fluid dynamics (CFD).

The first experimental investigation of DIC was described in Frederik et al. [24], with dedicated tests performed in the boundary layer test section of the Milan wind tunnel. Three G1 wind turbine models [17] were placed in the test section, aligned, and at a five-diameter distance from each other. In the experiments, two different inflow conditions and different DIC amplitudes and frequencies were tested. The inflow turbulence was generated via roughness elements, recreating typical onshore (low-turbulence) and offshore (high-turbulence) conditions. The downstream turbines were used as sensors to measure thrust and power. A total power increase of up to 4% was reported for the high-turbulence case. In van der Hoek et al. [25], pulse was applied to a single MoWiTO-0.6 model turbine [26]. In this case, the focus was on the wake, which was captured with three-dimensional particle image velocimetry (PIV). A decrease in wake velocity deficit and increased turbulence levels were shown. It was also possible to visualize and comment on the effect of DIC on the breakdown of the tip vortices, which is strictly related to the wake re-energizing process [27].

Experimental studies of the helix were performed by Heckmeier and expanded on by van der Hoek et al. [28]. The model turbine considered in van der Hoek et al. [28], was again the MoWiTO-0.6. The layout consisted of two aligned models at a five-diameter distance from each other. As in [25], 3D-PIV was used to look at the wake, and additional information was gained through the downstream turbine. In the tested conditions, the individual pitch signal affected the stability of the tip vortices system, accelerating its breakdown and increasing the entrainment of kinetic energy in the wake. On a global scale, gains reached up to 15% of the total power output. While these results look very promising, the studies they came from were limited to small farms and relatively low turbulence intensity of the inflow, resulting in very stable wakes. Testing more complex conditions can be expensive, even numerically: generating synthetic turbulence with precursor simulations or introducing complex terrain configurations significantly increases the computational cost of already heavy simulations. Before blindly committing resources to intensive testing, it makes sense to try and better understand the physics behind DIC techniques with carefully chosen simplified models.

1.4 MODELLING FOR WIND FARM CONTROL

If we want to model a wind farm to optimize its control strategy, we need three different models: an inflow model, a turbine model, and a wake flow model.

1.4.1 Inflow models

Wind turbines and wind farms cannot be studied without some notions about the atmosphere they operate in. We call the atmospheric boundary layer (ABL) the lowest layer of the atmosphere. It can be defined as the part of the troposphere in which the presence of the earth's surface has a non-negligible influence and frictional forces play a role.

The Earth's surface is where turbulence is generated in the atmosphere. It acts as a sink for atmospheric momentum and also influences heat and moisture levels. Understanding this is crucial for accurately describing wind patterns around wind turbines. In the ABL, we observe differences in momentum, turbulence, and concentrations of heat and moisture when compared to the free atmosphere above. Based on these atmospheric variables, we can distinguish three types of ABL:

- convective boundary layer (CBL) if the heat input from the surface dominates;
- stable boundary layer (SBL) if the surface is cooling the atmosphere;
- neutral ABL if the shear is the dominant phenomenon.

The vertical structure of the ABL is also affected by the geometrical and physical properties of the surface. The simplest structure is found over flat, horizontally homogeneous terrain with uniform soil type and a uniform distribution of roughness. For this kind of surface, the evolution of the ABL follows a diurnal cycle: CBL during day and SBL at night. The ABL will be neutral when clouds, wind, and precipitation cancel the effect of radiation.

As wind turbines grow bigger and taller, their hub heights exceed the surface layer, which is the only part of the ABL where simple power laws or logarithmic profiles are a valid description. A more sophisticated way to generate inflow conditions is to run so-called precursor simulations. Precursor simulations are performed in a domain without wind turbines over a time span that is sufficient for the turbulence to develop correctly. The volume field is then used to initialize the wind farm simulation (successor), and data planes are used as inflow boundary conditions.

1.4.2 Wind turbine models

While the blade element momentum (BEM) method [29] is still extensively used for preliminary design and simplified analysis of the operation of wind turbines, it is not accurate enough to well describe either flow-blade interaction nor wake development and, most of all, it does not give acceptable results when dealing with the complex three-dimensional flow fields a real turbine undergoes, especially in wind farms.

In the context of CFD, the most well-known and widely studied approaches are:

- fully resolved wind turbine rotor (FRW): the rotor geometry is entirely reproduced. It is the most accurate but its computational cost makes it industrially irrelevant ;
- actuator disk model (ADM): a hybrid CFD-analytical model where the rotor is seen as a disk;
- actuator line model (ALM), [30]: a hybrid CFD-analytical model where the blades are singly modeled as lines;

The second and third models descend directly from the BEM method. The turbine does not physically exist in the domain, but it is modeled by computing the forces through tabulated data or an aeroelastic code, which is then introduced as a body force in the Navier-Stokes equations. These parametrized forces are distributed smoothly to avoid singular behavior and numerical instability. A fundamental

difference between the two is that while ADM is suitable only for steady calculations, ALM, having to reproduce the rotation of the blades, has an unsteady formulation.

ACTUATOR DISK The concept of an actuator disk was already present in the basic aerodynamic description of wind turbines. The difference between this approach and the BEM method is that the solution of Navier-Stokes (NS) equations replaces the annular independence. Comparisons with experiments have proved that ADM gives good results for asymmetric flow conditions and can provide useful information regarding phenomena such as dynamic inflow and turbulent wake states. The biggest limitation of this model is that, since the force distribution is uniform on the disk, the influence of the blade is taken as an integrated quantity in the azimuthal direction.

ACTUATOR LINE The ALM model was developed in order to overcome the limitations of the axisymmetric ADM. The main difference is that the forces, instead of being distributed uniformly on the disk, are applied to the flow field along rotating lines corresponding to the individual rotor blades. They can be modeled in a way that allows them to respond dynamically to changing conditions, and when a structural code is used, they can be flexible as real blades. This allows us to describe the wake's dynamics better and capture the tip vortices and their influence on the induced velocities. However, finer phenomena, such as those involving the blade boundary layer, cannot be captured. That's the main disadvantage with respect to the FRW but also what makes it so computationally convenient. Moreover, large eddy simulations (LES), which have been reported to present issues in the treatment of the near-wall region, can now be used more freely. Two crucial aspects of the ALM that differentiate the many models available are:

- The sampling of the freestream velocity;
- The projection of the body force;

We will discuss both issues extensively in Chapter 3.

Structural modelling

As rotors get bigger, it is becoming more important to account for aero-elastic effects. Recently, fluid-structure interaction (FSI) frameworks, which contain an aerodynamic part that determines wind loads and a structural part that describes the dynamic response of the structure, have gained much interest. At the high-fidelity extreme of the structural dynamics spectrum, we find computational structural dynamics (CSD) methods. Structural models used in the aero-elastic modeling of wind turbine blades can be roughly categorized into 3D finite elements method (FEM) and 1D equivalent models. If appropriately constructed, the 1D beam model is much faster than 3D FEM and provides accurate results. Wind turbines are slender structures, meaning that they have one principal dimension much larger than the other two. Therefore, they can be efficiently modeled using 1D models. The beam axis is defined along the spanwise direction, and a cross-section perpendicular to this axis varies along the span. The most often used beam model is the Euler-Bernoulli linear beam model. The blade is modeled as a flexible cantilever beam with distributed mass and stiffness. The slender beam is subjected to extensional, torsional, and bending loads, neglecting the shear deformations. In the modal approach, the flexible bodies' deflection shape is described as a linear combination of a set of modes shapes, which are usually obtained from a finite element pre-processor.

The normal mode superposition is an effective way to reduce the degrees of freedom and, therefore, reduce the problem's size. However, the modal approach's flexibility is restricted by the type and number of degrees of freedom (DOFs) allowed in the structure, leaving aside the possibility to include the torsional eigenmodes.

1.4.3 Wake flow models

While in this thesis, we focus on high-fidelity modeling based on LES, in the context of wind farm control, it is important to have an overview of wake models in general. Wake models have very

different levels of complexity and fidelity and have different purposes. The high-fidelity ones are computationally expensive and are mostly used for validation. The low-fidelity models are mostly control-oriented ones. Figure 6 presents a general overview, table 1 goes in more details.

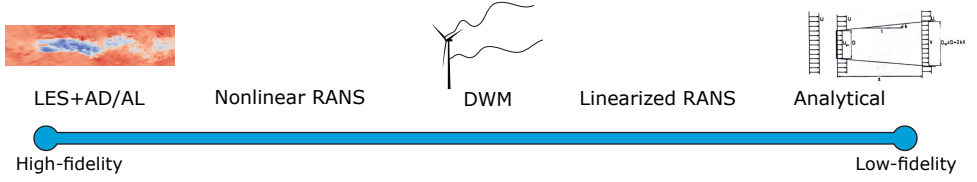


Figure 6: Overview of wake models, from high-fidelity (on the left side) to low-fidelity (on the right side)

On the high-fidelity side of the spectrum, we find CFD, from LES (combined with ALM and ADM) to Reynolds averaged Navier Stokes (RANS). On the opposite side, we find analytical models. The most famous one is the Jensen model [31], which is based on global momentum conservation and on the assumption of linear expansion of the wake. FLORIS [32] is a control-focused wind farm simulation software that incorporates many of these wake models. In addition to the Jensen model, it contains the Gaussian model [33], and the Curl model [34].

In between, we have the dynamic wake meandering (DWM) model [35], which considers the wake as a passive tracer driven by the large-scale turbulence structures in the atmospheric boundary layer. An interesting example of a mid-fidelity model is Fuga [36], a fast engineering tool based on the linearized RANS equations. What makes it fast is that it uses a system of look-up tables to construct the velocity field behind a turbine.

Experiments and numerical results obtained with high-fidelity models can help improve the low-fidelity ones. Incorporating knowledge of the physics of DIC into control-oriented models is one of the main objectives of this thesis.

Table 1: Overview of wake models

	Low fidelity	Medium fidelity	High fidelity
Model type	Kinematic models	Flow field models	Flow field models
Fundamentals	Parametric	2D NS	3D NS
Models	Jensen, FLORIS, Frandsen, ..., FLORI-Dyn	DWM, WFSim, Ainslie...	SOWFA, WakeFarm, UT-DWF, SP-Wind, ...
Flow dimension	2D	2D	3D
Dynamic/Static	Static, Dynamic	Dynamic	Dynamic
Turbine model	ADM	ADM/ALM and/or an aerodynamic package (e.g., FAST)	ADM/ALM and/or an aerodynamic package (e.g., FAST)
Comp. effort	Order of seconds on a desktop PC	Order of minutes on a desktop PC	Order of days on a cluster of 10^2 CPUs
Model accuracy	Low – medium	Medium – high	High – very high

1.5 THESIS OBJECTIVES AND OUTLINE

When we first zoomed out to understand how to tackle the very specific physical problem posed by helicoidal wakes, there was no obvious linear path to be followed in the exploration. Consideration of previous knowledge on the topic allowed us to restrict the wide range of options. The benefits of DIC techniques are less relevant the higher the turbulence intensity. These techniques are also labor-intensive for actuators, and we expect fewer adjustments to be necessary in more uniform inflows. For these reasons DIC should be implemented in offshore wind farms. Knowing this reduces the variety of atmospheric conditions that we will be dealing with. It also individuates a turbine scale since, for offshore turbines, the trade-off between technical feasibility, transportation, and maintenance is more shifted towards the choice of bigger rotors.

These considerations pertain to the object of our study, but the range of methodologies that are potentially applicable to it is also wide. The first important choice is to approach the topic numerically. This is very often the case in aerodynamics since the cost and the logistics of experiments can easily become prohibitive. Numerical approaches wildly vary in specifics and fidelity. While there are established methods for well-documented issues, very often, for new applications, the choice will not be easy, and model development might be necessary. This is also something we specifically chose to address.

If we sum up this discussion, we can give a short definition of the thesis objective:

Thesis goal: Development of numerical methods reliably modeling wind turbine wakes as a tool for optimized solutions of dynamic wind farm control.

Our contribution to this wide challenge was to give answers, as confidently as possible, to three main research questions. Figure 7 illustrates them briefly. Each question is further broken up into sub-questions (the engineering way) and examined in the following of this dissertation. The first two questions are methodological and are two aspects of the bigger question of how we can best support wind farm control with high-fidelity modeling.

We mentioned the fact that DIC is beneficial to turbines with bigger rotors. This means long, flexible blades. While our focus is on the wake of the wind turbines and not on their structural behavior, wake dynamics and rotor aero-elasticity influence each other in a complex way that the simple analytical models often used to describe one or the other can not account for. For example, purely aerodynamic models like BEM do not account for the blade's built-in curvature and sweep, for their flexing out-of-plane causing further interaction with the generated vorticity, for non-linear deflection (including torsion and bend-twist coupling) that further complicate the physics.

FSI models account for all of these effects, but they are very computationally expensive. We deemed it necessary to evaluate the necessity of resorting to them. Therefore, the first research question is posed as follows.

Research Question 1: When does the accuracy in the wake modeling obtainable with a computational fluid and structural dynamics (CFD-CSD) coupling justify the increased computational cost?

Further discussion on the issue, methodology, and results of this evaluation are presented in **Chapter 2**. These results lead to a choice regarding the turbine structural modeling. The following step was to isolate the turbine aerodynamics.

The ALM is the go-to approach for high-fidelity wind turbine simulations. It reduces the cost of CFD by modeling the rotor blades (and the tower and the nacelle, if necessary) as lines for which each point represents a section of the blade that exchanges with the fluid a body force computed analytically and projected onto the domain with a projection function. The ALM can be very reliable, but there is no consensus on how important parameters such as the value of the projection function width ϵ should be set and how the angle of attack should be evaluated.

We gave our own assessment of and contribution to the state of the art of ALM in **Chapter 3**, which answers the question:

Research Question 2: What are the limitations of actuator line models (ALM) for wind turbines, and how can we address them?

The techniques described in section 1.3 of this introduction are quite novel, so there is a multitude of open questions. A lot of gaps could be filled with control-oriented models, but these should be addressed with some further understanding of the physics that leads to accelerated wake recovery. The third research question was:

Research Question 3: Can we leverage the amount of data obtainable from LES simulations to find out how DIC works and embed this knowledge into control-oriented models?

Chapter 4 and **Chapter 5** cover data-driven modeling of DIC-manipulated wakes, shedding some light on the coherent structures introduced in the wake and discussing the influence of the particular excitation signal and the inflow conditions.

Each chapter was previously written as a journal paper; it has its own introduction and conclusion, and some concepts will be repeated so that the chapter can be read independently from the others. However, the work has been carried out in the order of presentation, and, as specified, methodological results from the first two chapters informed choices made in the third. Final conclusions from this dissertation and suggestions for future works are given in **Chapter 6**.

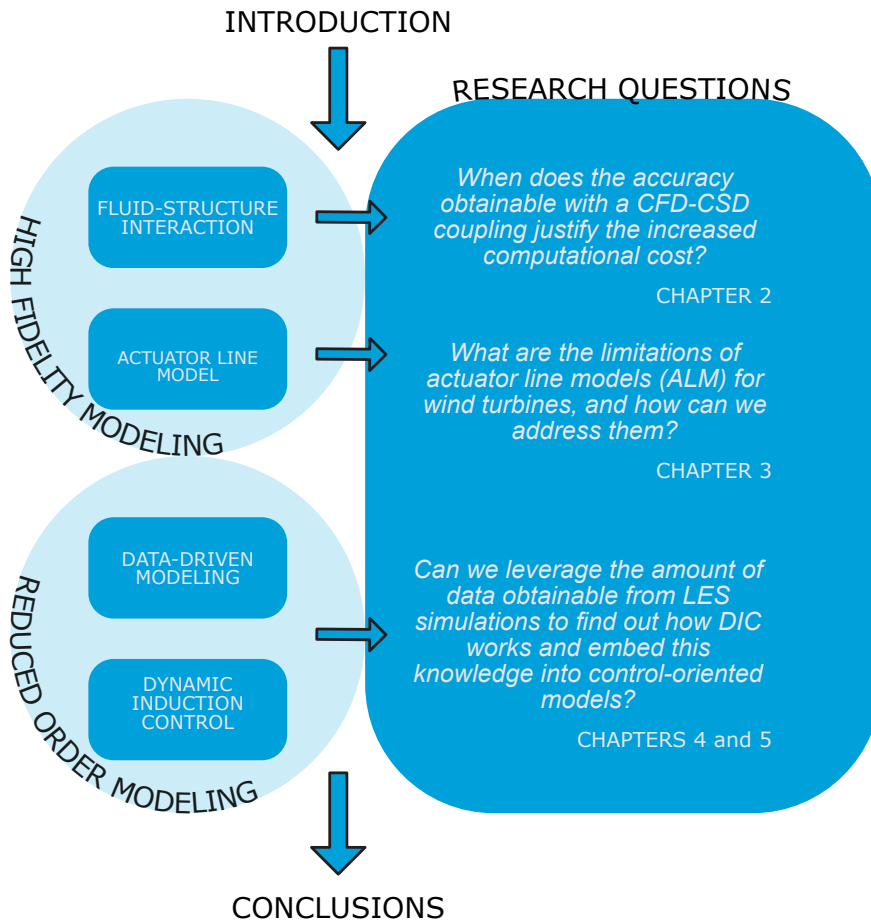


Figure 7: Thesis outline

2

THE INFLUENCE OF WIND BLADE FLEXIBILITY ON THE WAKE

This is the essence of intuitive heuristics: when faced with a difficult question, we often answer an easier one instead, usually without noticing the substitution.

Daniel Kahnemann

In this chapter, we test a FSI method based on the SOWFA+OpenFAST framework. The linear structural module of FAST is coupled to SOWFA's Actuator Line simulations to perform the aeroelastic analysis of a wind tunnel scaled model (1 : 75) of the DTU 10 MW turbine. The objective is to give a quantitative description of the influence of turbine stiffness on wake flow by varying the model's structural properties.

The simulations are performed in below-rated and above-rated operating conditions. Turbulence is generated by positioning disturbing elements at the inlet, analogously to what was done in the reference wind tunnel tests. Results show that flexibility starts to considerably impact the wake velocity deficit when the tip deflection is somewhere between 4% and 12% of the blade length.

Based on these results, an indication is given of when the accuracy obtainable with the CFD-CSD coupling justifies the increased computational cost.

2.1 INTRODUCTION

In the Introduction, we showed how the most obvious way to increase power production at a wind turbine level is to increase blade size, which, of course, affects flexibility. The main consequence is the coupling of the considerable deflections with the unsteady aerodynamic loads as documented in Ahlström [37].

Although aero-elastic stability has typically not been a key design driver for rotor blades up to now, the situation might change for future highly flexible and large rotors. The turbines of the future are not only bigger but also installed closer and closer together. An accurate enough modeling of wake dynamics is necessary at a wind farm level to optimize layout, operation, and control. Wake dynamics and rotor aero-elasticity are strongly coupled and influence each other in a complex way that the simple analytical models often used to describe one or the other can not account for.

Current aerodynamic theories do not accurately describe the interaction between a highly variable inflow and the unsteady aerodynamics of the moving and deforming blades. Blades moving through air shed vorticity normally convected downstream and away from a relatively stiff structure. When the blades flex out-of-plane, the rotor interacts with its vorticity, calling the design assumptions' accuracy into question. Additionally, the structural dynamics of blades incorporating composite materials, built-in curvature and sweep, and large non-linear deflection (including torsion and bend-twist coupling) further complicate the physics and the assessment of stability.

Recently, fluid-structure interaction (FSI) frameworks, which contain an aerodynamic part that determines the wind loads and a structural part to describe the dynamic response of the structure, gained much interest. At the high-fidelity extreme of the FSI spectrum, we find computational fluid and structural dynamics (CFD-CSD) methods. In Hsu and Bazilevs [38], the FSI framework consisted of a low-order arbitrary Lagrangian-Eulerian variational multi-scale (ALE-VMS) flow solver and modeling of the rotor blades as thin composite shells. Results were obtained for a single blade. Yu and Kwon [39] combined an unstructured mesh computational fluid dynamics (CFD) solver and a finite elements method (FEM)-based computational structural dynamics (CSD) solver to predict unsteady aerodynamic loads and aeroelastic deformations. More recently, Sayed et al. [40] presented an explicit coupling between a unsteady Reynolds averaged Navier Stokes (URANS) solver and a structural solver based on non-linear Timoshenko beam elements. Their results showed an increase of rotor power and thrust by 1% and 0.3%, respectively, due to the large edgewise deformation that significantly increases the contribution of the radial force to the total torque of the turbine.

None of these studies explicitly focused on the wake. However, the information on thrust variation (going from rigid to flexible model) given by Sayed et al. [40] for a 180 m diameter wind turbine gives us an idea of the numbers we are dealing with (thrust force and wake development are strongly related). Finally, in Ma et al. [41], an effort in this direction is made by developing a low computational cost method combining the actuator line model (ALM) and finite-element beam theory and using it to study velocity and vorticity distribution in the far wake. They conclude that neglecting blade flexibility leads to a slight underestimation of velocity recovery and that no appreciable improvements were attained when considering non-linear effects.

In Rodriguez et al. [42], the stability of tip vortices shed from flexible rotors is studied with an aeroelastic free-vortex wake method. The main results were the validation of their framework and the observation that the wakes of flexible rotors experience an early breakdown due to an initial transient of flap-wise deflection and are not influenced by the torsional response.

A big limitation of all the presented studies was that the used frameworks were not validated on experimental data (which is poor or nonexistent for big rotors) and that, even though all the used methods are very computationally expensive, no clear indication as to when their use is essential was given.

The present study aims to address the latter issue by introducing flexibility effects not by considering a big rotor but rather by changing the structural properties of the blade. We considered the scaled model of the DTU 10 MW turbine [43] and tested three structural models under turbulent inflow in two different operating conditions.

This chapter is outlined as follows. The applied methodology for the aerodynamic and structural

parts is discussed in section 2.2. The turbine and the data are described in section 2.3. Finally, after discussing the Numerical Setup and the Inflow in sections 2.4 and 2.4.4, the results are presented and discussed in section 2.5, where we also elaborate on the consequences of neglecting non-linear effects.

2.2 METHODS

This section presents and discusses the adopted models for the aerodynamic and structural parts. For both, there will be a theoretical introduction first and then a description of the software. The aerodynamic part is dealt with using the actuator line model, the go-to strategy for high-fidelity wind turbine modeling. For the structural part, an Euler-Bernoulli beam model will be used.

2.2.1 Aerodynamic Model

The ALM [44], descends directly from the blade element momentum (BEM) method. The turbine does not physically exist in the domain but is modeled by computing the forces through tabulated data or an aero-elastic code and then directly introduced as body forces in the Navier-Stokes (NS) equations.

The ALM represents each blade as a radially varying force line. The actuator line is discretized by means of a number of points. For each point, the so-called free-stream velocity is sampled, and velocity magnitude and angle of attack are computed. The lift and drag coefficients are determined from airfoil data and used to calculate the forces which have to be corrected for 3D effects. A popular correction is based on the Glauert formulation [45], which multiplies the forces of each blade section by a function F_{tip} , based on the local section radius r :

$$F_{tip} = \frac{2}{\pi} \cos^{-1} \left(e^{-g \frac{B(R_{tip}-r)}{2r \sin(|\phi|)}} \right) \quad (2)$$

where B is the number of blades, R_{tip} is the tip radius, ϕ is the flow angle, and g is an empirical correction function. In order to apply the correction to the root, a very similar equation is used:

$$F_{root} = \frac{2}{\pi} \cos^{-1} \left(e^{-g \frac{B(r-R_{root})}{2r \sin(|\phi|)}} \right) \quad (3)$$

where R_{root} is the root radius. In practical terms, F_{tip} and F_{root} reduce the forces on blade sections to zero at the tip and root while having small effects near the blade center.

The force per unit volume is calculated and inserted as a source term in the NS equations for the corresponding cell:

$$\vec{f} = \frac{\vec{L} + \vec{D}}{V_{cell}} \quad (4)$$

where L and D are the blade point lift and drag and V_{cell} is the volume of the cell containing the blade point. Since the blade surface is not modeled, the model does not replicate finer flow features such as the boundary layer and the separation at high angles of attack. However, the wake development and interaction with the atmospheric boundary layer can be captured, resolving the turbulent eddies up to the blade chord scale. Two crucial aspects of the ALM that differentiate the many ALM models available are:

- the free-stream velocity sampling;
- the projection of the body force.

Although not straightforward, the correct definition of free-stream velocity is fundamental to obtaining accurate results. The projection issue concerns how the computed body forces are applied back to the domain.

The most physical solution would be to apply them in the singular cell containing the airfoil pressure center, but mathematically speaking, this could be very problematic since the sharp gradient generated could lead to strong spurious oscillations in the actuator line vicinity. The solution is to apply some kind of smearing function to distribute the force in multiple cells, avoiding the sharp gradients altogether. The one we use for this study was proposed by Sorensen and Shen [44], and it is a three-dimensional Gaussian function, isotropic in blade width and fixed in width along the blade span.

SOWFA

Simulator for Offshore Wind Farm Applications (SOWFA) is an open-source extension of OpenFOAM developed by the national renewable energy laboratory (NREL). It is a set of solvers, boundary conditions, and actuator-type turbine models specific for wind farm applications. SOWFA allows the reproduction of a range of different atmospheric conditions, and the wind turbine wakes, and the interaction between them. Further information can be found in Churchfield et al. [46].

2.2.2 Structural Model

Structural models used in the aero-elastic modeling of wind turbine blades can be roughly categorized into 3D FEM and 1D equivalent models. If appropriately constructed, the 1D beam model is much faster than 3D FEM and provides accurate results. Wind turbines are slender structures, meaning that they have one principal dimension much larger than the other two. Therefore, they can be efficiently modeled using 1D models. The beam axis is defined along the span-wise direction, and a cross-section perpendicular to this axis varies along the span. The beam models can be divided into linear and non-linear ones. A very comprehensive review on this topic can be found in Hansen et al. [47]. This study is mainly performed with a linear model. This is mainly motivated by the fact that the non-linear structural module of OpenFAST is not integrated into the coupling. However, some considerations in that regard are presented at the end of section 2.5.

The most used linear beam model is the Euler-Bernoulli beam model. The blade is modeled as a flexible cantilever beam with distributed mass and stiffness. The slender beam is subjected to extensional, torsional and bending loads, neglecting the shear deformations. In the modal approach, the flexible bodies' deflection shape is described as a linear combination of a set of modes shapes, which are usually obtained from a finite element pre-processor. Following Jonkman [48], at any point on the structural element, the lateral deformation can be expressed as

$$u(z, t) = \sum_{i=1}^n \phi_i(z) q_i(t) \quad (5)$$

where ϕ_i and q_i are the normal mode shape and the generalized coordinate of the i -th normal mode. Alternatively, these deflections could be expressed using n other functions, $\varphi_j(z)$, not unique to each normal mode:

$$u(z, t) = \sum_{j=m}^{n+m-1} \varphi_j(z) q_j(t) \quad (6)$$

According to the Rayleigh-Ritz method, each normal mode shape can be obtained combining the n shapes functions with the constant proportionality coefficient $C_{i,j}$:

$$\phi_i = \sum_{j=m}^{n+m-1} C_{i,j} \varphi_j \quad (7)$$

The linear structural solver used in this work considers polynomial shape functions:

$$\varphi_j(z) = \left(\frac{z}{Z}\right)^j \quad (8)$$

The coefficients $C_{i,j}$ can be found by solving:

$$(-\omega_i^2 \underline{\underline{M}} + \underline{\underline{K}}) \underline{\underline{C}}_i = \underline{\underline{0}} \quad (9)$$

where $\underline{\underline{M}}$ and $\underline{\underline{K}}$ are the $n \times n$ mass and stiffness matrix, respectively. ω_i is the i -th natural frequency.

The normal mode superposition is an effective way to reduce the degrees of freedom and, therefore, reduce the problem's size. However, the modal approach's flexibility is restricted by the type and number of degrees of freedom (DOFs) allowed in the structure, leaving aside the possibility to include the torsional eigenmodes.

OpenFAST

OpenFAST is the latest version of Fatigue, Aerodynamics, Structures, and Turbulence (FAST), a multi-physics, multi-fidelity tool for simulating the coupled dynamic response of wind turbines developed at NREL. In Jonkman et al. [49], its use and code structure are detailed. It is a framework written in Fortran 2003 that couples computational modules for aerodynamics, hydro-dynamics for offshore structures, control and electrical system dynamics, and structural dynamics to enable coupled non-linear aero-hydro-servo-elastic simulation in the time domain. It can simulate a variety of wind turbine configurations, both onshore and offshore, taking into account numerous physical phenomena. The modules used in this study are:

- **AeroDyn**, the aerodynamic module that enables the aeroelastic simulation on both the tower and the blades. It can run in BEM method mode or in the coupled mode with SOWFA. When coupled with SOWFA, this module performs the blade element part of the BEM, while the CFD software performs the momentum part, as already explained.
- **InflowDyn**, is the module that provides the wind inflow information to AeroDyn. When OpenFAST is coupled with the CFD software, it is replaced by SOWFA.
- **ElastoDyn**, the linear structural-dynamics module. It is based on the modal approach. It takes the aerodynamic loads as input and returns the wind turbine's accelerations, velocities, and reaction loads. It allows the user to activate up to 24 degrees of freedom.
- **BeamDyn**, the non-linear time-domain structural-dynamics module based on geometrically exact beam theory (GEBT). It supports the full geometric non-linearities and large deflection with bending, torsion, shear, and extensional degrees of freedom. It takes the complete mass and stiffness matrices as input to model anisotropic composite materials, twisted and pre-coned configurations.

2.2.3 Coupling

When SOWFA runs coupled with OpenFAST, the blade element theory calculations are performed by its AeroDyn module. The actuator line CFD model replaces the momentum part of BEM. For this reason, the two software continually exchange information, and a typical run follows the steps below:

1. SOWFA feeds OpenFAST inflow information at blade elements;
2. The aerodynamic forces are computed by look-up table;
3. OpenFAST computes the turbine structural and system response;
4. The modified aerodynamic forces are fed back to the CFD.

When the ElastoDyn and BeamDyn modules are also active in FAST, the fed-back forces also account for the blade deflection.

2.3 THE MODEL TURBINE AND THE EXPERIMENTAL DATA

This section describes the laboratory-scale model turbine considered for the study and the experimental data that will be used for comparison.

2.3.1 The Turbine

The chosen turbine is the (1 : 75) scaled model of the DTU 10 MW wind turbine that was developed during the *H2020 project Life50+* by Bayati et al. [50]. The scaling parameters reflect the desire to find an optimal compromise between maximizing the dimensions for lowering the Reynolds mismatch and limiting the dimensions to limit the blockage ratio, around 8%. The main characteristics of the turbine are gathered in Table 2.

Table 2: Turbine Characteristics

Blade number	3
Diameter	2.38 m
Tower height	1.98 m
Shaft Tilt	-5°

Aerodynamic Characteristics

The aerodynamic design has been carried out with the aim of matching the reference thrust and torque coefficients, the scaled first blade flap-wise frequency, and the correct blade weight. In order to reach these goals, the PoliMi model uses completely different airfoils, twist and chord distributions.

AIRFOIL GEOMETRY One of the most critical aspect in the model blade design is the airfoil selection. The Reynolds numbers obtainable in the wind tunnel impose the choice of different airfoils along the blade with respect to the full-scale model, as shown in Figure 8. In Equation 10, ρ is the air density, U is the wind speed, c is the blade chord length and μ is the air dynamic viscosity.

$$Re = \frac{\rho U c}{\mu} \quad (10)$$

In order to match the aerodynamic performance at lower Reynolds numbers, the entire blade is designed using the *SD7032* airfoil. Only in the area near the blade root the blade section shape is interpolated with the circular section, thus allowing a smooth transition to the circular blade root section.

BLADE GEOMETRY The scaled model chord and twist distributions are different from the full-scale one. The chord has been changed to match the scaled rotor thrust, and the twist has been designed considering the different zero lift values of the airfoil used. Chord, twist, and thickness distributions along the blade for the two models are shown in Figures 9 and 10.

Structural Characteristics

The wind tunnel model has been designed to study both aerodynamic and aero-elastic performance. Therefore, proper structural scaling has been taken into account. The resulting wind turbine can be used to conduct aero-elastic research, as it is the main goal of this work.

The blade has been built with a single high-modulus carbon fiber layer of 0.3 mm thickness in order to match the mass target and preserve the high stiffness required. The first flap-wise frequency

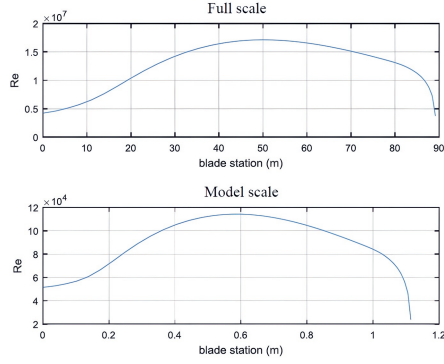


Figure 8: Reynolds number distribution for the full-scale DTU 10 MW and for the scaled model

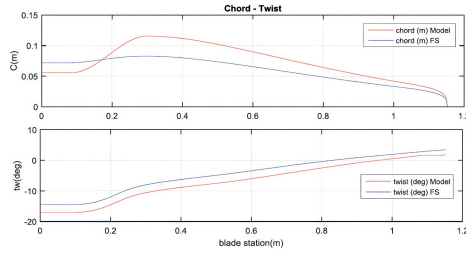


Figure 9: Chord and twist distributions for the full-scale DTU 10 MW (FS) and for the scaled model

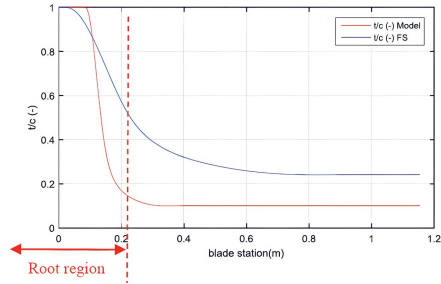


Figure 10: Thickness distributions for the full-scale DTU 10 MW (FS) and for the scaled model

is around 15 Hz, approximately the value required to preserve the structural characteristics of the full-scale turbine.

The tower is a 1.54 m long pole of constant cylindrical cross-section. It is made up of carbon fiber, resulting in very light and stiff, with its first natural frequency around 11 Hz. The model is built in carbon fiber, providing the best compromise between mass density and stiffness.

2.3.2 The Experimental Data

The experimental data obtained during the UNAFLOW project [51] was available and we used it to justify some of our modeling choices. The test campaign has been carried out in the PoliMi Wind Tunnel boundary layer section. The section has a 36 m length, 14 m width, and 4 m height, allowing for very low blockage effects in the tests. The operational parameters reported in Table 3 were considered. Rotor speed and collective pitch angle were fixed.

Table 3: Operational parameters

Condition	Wind speed	Rotor speed	tip-speed ratio (TSR)	Pitch Angle, θ
Rated 2	4.0 m/s	241 rpm	7.5	0°
Above rated	6.0 m/s	265 rpm	5.5	12.5°

At Rated 2, the wind turbine is operated at the optimum full-scale value of TSR, and the power coefficient is the maximum one. In the above-rated condition, the TSR is lower, and the collective pitch angle is increased to preserve rated power. Experiments were carried out in smooth flow, and the turbulence intensity across the test section height was approximately 2%.

Several quantities were measured during the experiments. The undisturbed wind velocity was measured by a pitot tube 7.15 m upstream of the rotor at hub height. The tower-top forces were measured by a six-component force transducer. In a few selected test cases, the wake of the wind turbine was scanned by triaxial hot-wire probes. In an even smaller sample of test cases, particle image velocimetry (PIV) measurements were carried out to describe the wake flow structure.

The absence of sensors on the blades limits our analysis to a comparison of the wake. The measurements of the velocity in the wake provided for the comparison in this study refer to the condition that in Table 3 is called *Rated2*. The thrust coefficient has been provided as a function of the tip-speed ratio to consider different conditions in the simulations.

2.4 NUMERICAL SETUP

This section is about the case setup. Subsection 2.4.1 describes the domain and its discretization, then in 2.4.2, 2.4.3 and 2.4.5 the choices in terms of time step, boundary conditions and numerics are justified.

2.4.1 Space Discretization

The considered computational domain is 14 m wide, 3.8 m high, and 58 m long, with the reference system located 10 rotor diameters downstream of the inlet, at the turbine location. The length has been increased from the 35 m of the actual wind tunnel to 58 m to allow a complete turbulence development and to avoid numerical instabilities within the flow.

The actuator line does not require a complete description of the blade's geometry, making the mesh simple and composed of only hexahedral cells. The basic mesh is built using the OpenFOAM's *blockMesh* utility, with 464 cells in the stream-wise direction, 112 in the cross-stream direction, and 32 in the vertical direction.

SOWFA guidelines indicate that at least 20 cells should cover the rotor diameter to resolve the wake reasonably. Thus, three cylindrical refinement zones extending from some distance upstream of the rotor to the domain end are introduced to better describe the area around the rotor and in the wake. Each refinement split every cell within the selected zone into eight sub-cells. This number allows for a good trade-off between accuracy and computational effort. It also makes sense to have an increasingly fine mesh going from the far wake to the near wake to the rotor disk.

Section 2.4.6 further details the mesh choice by considering the experimental data. We must add turbulence generators inside the domain since we want to consider a turbulent case. The full-scale DTU 10MW model is designed for offshore applications. The wind tunnel configuration that mimics the neutral offshore atmospheric boundary layer uses 14 type-B spires placed side by side and 1 m from each other, 1 m downstream of the test chamber inlet. A type-B spire consists of an equilateral trapezoid with a 2.0 m height, and the widths of the bottom and top edges of 0.26 m and 0.1 m, respectively. Two precursor simulations are performed to analyze the wind turbine in rated and above-rated conditions. The spires described above have been placed 1 m downstream of the porosity zone. The 1 m long porosity zone takes into account the pressure losses within the wind tunnel closed-loop circuit since it is not entirely replicated here. Expressly, the porosity coefficients are set to produce one unit dynamic pressure drop. The spires are modeled through a top-bottom meshing strategy without adding layers around their surfaces. In fact, it is not necessary to accurately resolve their boundary layer if their purpose is just to generate a turbulent flow.

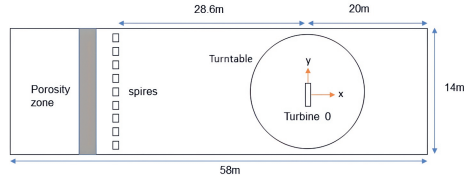


Figure 11: Numerical wind tunnel configuration. The reference system is centered at the turbine location.

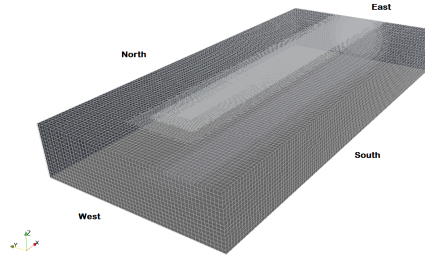


Figure 12: Mesh layout and patches

2.4.2 Time Discretization

The time step must be set correctly to avoid numerical instabilities in the simulation both for the fluid model and the structural solver. The structural solver has less strict requirements concerning the CFD since it runs stably up to $\Delta t = 0.01$ s. However, the structural calculation must be performed at least once during a CFD interval, so the same flow time step is used. The parameter used to check the stability of the CFD solution is the Courant–Friedrichs–Lewy number (CFL), defined as:

$$CFL = \frac{U \Delta t}{\Delta x} \quad (11)$$

Typically, it has to be less than one to prevent the flow from crossing more than one cell every time step. However, scaled wind turbines rotate very fast, so a different definition is introduced:

$$CFL_{tip} = \frac{\omega R \Delta t}{\Delta_g} \quad (12)$$

where ω is the wind turbine rotational speed, R is the blade radius and $\Delta_g = \sqrt[3]{\Delta_x \Delta_y \Delta_z}$ is the equivalent cell dimension. The correct value of this parameter should prevent the tip from crossing more than one cell per time step and guarantee an equal number of force calculations per rotor revolution. In fact, if the time step is too large, the forces can be computed asymmetrically or only in specific positions, introducing oscillations of the loads or vibrations of the structure.

A precursor simulation is run for 130 s to stabilize the main flow quantities and have the correct turbine inflow. Velocity and turbulence values reach a quasi-stable condition at around 90 s. The information needed for the successor simulations is gathered starting from 95 s. The time step is set to $\Delta t = 0.001$ s, maintaining a CFL_{tip} under 2.5 all over the simulation. A small time step is crucial if the intention is to resolve the turbulence field accurately. Further reducing the Δt would require too much CPU time.

2.4.3 Boundary conditions

The simulation boundary conditions are summarized in Table 4.

Table 4: Boundary conditions

Patch	U	p	k	nuSgs
west	fixedValue	zeroGradient	fixedValue	fixedValue
east	inletOutlet	fixedValue	zeroGradient	zeroGradient
lower	uniformFixedValue	zeroGradient	zeroGradient	zeroGradient
upper	uniformFixedValue	zeroGradient	zeroGradient	zeroGradient
north	uniformFixedValue	zeroGradient	zeroGradient	zeroGradient
south	uniformFixedValue	zeroGradient	zeroGradient	zeroGradient

Two precursor simulations are performed considering different undisturbed velocities at the inlet. Specifically, the values $U_\infty = 3.0$ m/s and $U_\infty = 5.0$ m/s are imposed on the west patch to obtain the desired below-rated and above-rated conditions, respectively. The precursor is an atmospheric boundary layer (ABL) simulation performed on an empty domain to generate initial conditions and time-dependent inflow boundary conditions for the main simulation. It should run long enough to generate statistically steady atmospheric turbulence. The hub velocities obtained using these values are around 3.6 m/s for the first case and around 6 m/s for the second case.

The above-rated condition differs from that of the experimental test campaign but still represents an above-rated condition. The outlet pressure is set to 0 Pa (*east patch*). When considering uniform cases, slip condition on the walls is computationally advantageous compared to the no-slip since there is no need to reproduce the wall's viscous effect. Since our case is turbulent, the wind tunnel walls must be modeled, considering the friction they exert on the flow. For this reason, we have *uniformFixedValue* conditions. Friction is responsible for the viscous effects near the walls, which generate the turbulence required to match the actual chamber conditions.

2.4.4 Inflow

The atmospheric boundary layer is a complex turbulent flow influenced by many factors. An accurate reproduction of the ABL should match the following characteristics:

- variation of the wind speed with height;
- variation of the turbulence intensity with height;

- variation of the integral scales with height;
- turbulent spectra coherent with the $5/3$ law.

The wind tunnel environment allows for generating only a neutral ABL since the effect of the temperature is not reproduced. Moreover, the flow is confined by the walls, and the complete logarithmic evolution of a real ABL is not obtainable. The simulation of such a turbulent flow inside a wind tunnel is a tedious task and would require further investigation of the CFD parameters. Additionally, the required computational cost is very high, and only a limited time has been reproduced. Further increasing the solution time would probably yield a more developed turbulent flow. Figure 13 illustrates the inlet mean velocity vertical profile at different lateral positions for the below-rated and above-rated cases, respectively. The obtained velocity profiles agree with the PoliMi's Wind Tunnel profile for those particular conditions.

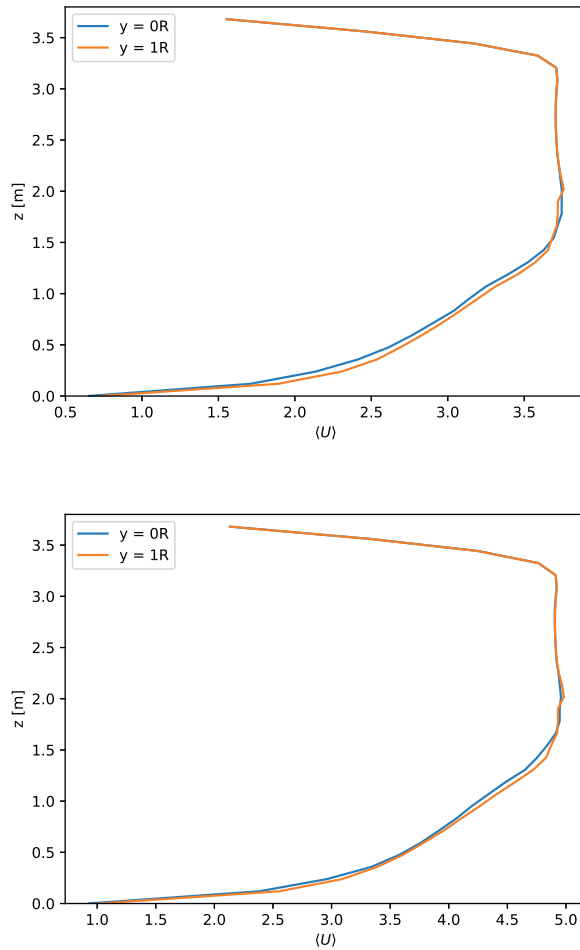


Figure 13: Mean streamwise velocity profile at vertical coordinates equal to 0 and to the radius - Below (on the top) and Above rated (on the bottom) condition

The turbulence spectra are reported in Figure 14. The inertial range follows the 5/3 law for both cases, indicating a correct simulation of the turbulent field.

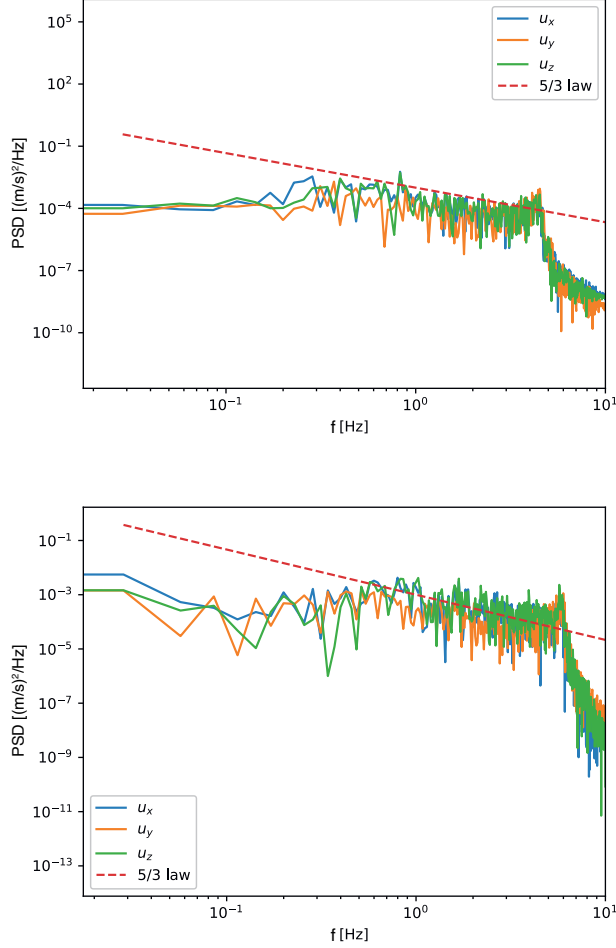


Figure 14: Energy spectrum at the hub $(x,y,z) = (0,0,0)$, rated (on the top) and above rated (on the bottom) conditions

2.4.5 Solver and Numerical Schemes

The solver used for the simulations is *pisoFoamTurbine.ALMAAdvancedOpenFAST*, which was written specifically to perform the coupled simulations and has been validated in various studies (Johlas et al. [52], Shaler and Jonkman [53]). The selected force projection is the most common, first defined by Sorensen and Shen [44]: a three-dimensional Gaussian function, isotropic in width and fixed along the blade span. As the guidelines prescribe, ϵ is twice the cell dimension in the rotor area. Glauert's correction [54] is used for tip losses.

The Pressure-Implicit with Splitting of Operators (PISO) loop performs one outer corrector and three inner correctors. The pressure solver used is the preconditioned conjugate gradients (PCG) method with GAMG preconditioner and preconditioned bi-conjugate gradients (PBiCG) with DILU preconditioner for velocity and turbulence variables.

The discretization schemes used are the *backward* second-order implicit method for the time, second-order unbounded *Gauss linear* for the gradients, and the divergence terms except for the velocity divergence, for which we blend first and second order, and *Gauss linear uncorrected* for the Laplacian terms. The Laplacian and surface-normal gradient schemes use orthogonality correctors. The turbulence structures are resolved by employing a large eddy simulations (LES) with a one-equation eddy viscosity SGS model. We also consider porosity with the fixedCoeff model already present in OpenFOAM.

2.4.6 Experimental data and mesh choice

We performed a comparison between our numerical results and the presented experimental data. The comparison does not constitute a validation of the framework, but it was useful to motivate some of our choices. In particular, it is impossible to reach grid independence when using actuator line models because of the coupling between the force projection width, ϵ , and the mesh dimension. Thus, to select the characteristics of the grid to be used in the rest of the study, we use the experimental velocity profile at 2.3 rotor diameters downstream of the wind turbine.

We run simulations on three different grids. The structural properties are the ones of the scaled model (carbon). The simulations are carried out with the same ϵ . The velocity profiles are normalized with respect to a reference velocity taken at hub height $1D$ upstream of the turbine.

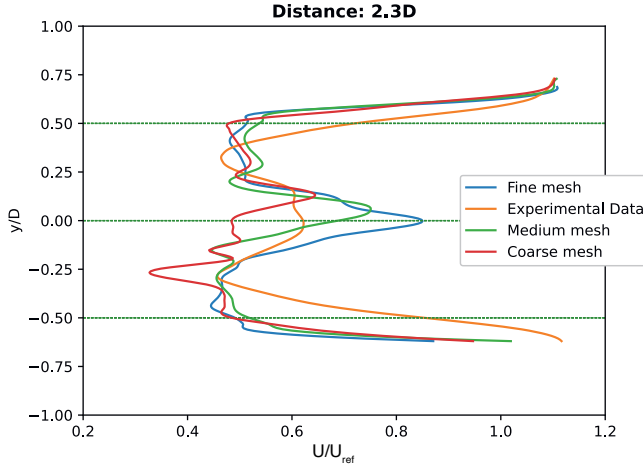


Figure 15: Streamwise mean velocity horizontal profile. U_{ref} is the undisturbed velocity.

Referring to Figure 15, it is difficult to visually choose which model creates wake profiles best in agreement with the experiments. Therefore, the root mean square (RMS) of the absolute error between the computed and the measured wake profiles, and the relative error are taken to quantitatively describe the two models. We express them as:

$$\epsilon_{RMS} = \frac{\sqrt{\sum_{i=1}^N (U_{computed}^i - U_{measured}^i)^2}}{N} \quad (13)$$

where N is the number of locations at which the wake profile is measured, and

$$\epsilon_{rel} = \frac{U_{measured}^i - U_{computed}^i}{U_{measured}^i} \quad (14)$$

The wake error statistics are reported in Table 5.

Table 5: Space discretization

	Coarse mesh	Intermediate Mesh	Fine mesh
Local refinements	2	3	4
Total number of cells	1140524	868933	11449914
Rotor equivalent cell dimension, Δ_g	0.0628	0.0314	0.0157
Cells on the rotor	38	76	152
ϵ_{RMS}	0.028	0.028	0.032
Mean ϵ_{rel}	0.146	0.089	0.06

The intermediate and fine grids show a more symmetric profile, with the accelerated central region almost in line with the hub position (represented by the green dashed line in the center). The errors in this area are related to the fact that the nacelle has not been modeled in the simulations, so the flow is not decelerated.

The uniform Gaussian force distribution spreads the forces well beyond the blade tip and root, representing the blade longer than it is. For this reason, the numerical velocity profiles are more extensive than the experimental ones. We can also observe how the numerical simulations over-predict the blade roots vortices. The description of the deficit in the root area is also affected by the fact that we are not modeling the nacelle. The coarse mesh over-predicts the velocity deficit, especially in the lower part, while the medium and fine grids are very close to the experimental values. The wind turbine performance are reported in Table 6.

Table 6: Rotor performance

	Power [W]	$\Delta error\%$	Thrust [N]	$\Delta error\%$
Experiment	90.996		40.431	
<i>Medium mesh</i>				
$\epsilon = 2\Delta_g$	93.622	+2.89%	38.443	-4.92%
$\epsilon = 1.25\Delta_g$	97.639	+7.3%	38.803	-4.03%
<i>Fine mesh</i>				
$\epsilon = 2\Delta_g$	98.280	+8.04%	38.882	-3.83%
$\epsilon = 1.25\Delta_g$	109.395	+20.26%	40.111	-0.79%

When constructing the fine mesh, it was decided to limit the refined area to the near wake. Extending it to the end of the domain, as in the other cases, would have led to a huge number of cells and unacceptable simulation times. Still, we went from one day and a half on the intermediate mesh to four days on the refined one. This choice limited the gain in accuracy that might have justified the additional effort. Therefore, we decided to perform the rest of the study with a grid based on the intermediate one. This grid is described in Section 2.4.1.

2.5 RESULTS

The two structural models described in Table 7 are simulated using OpenFAST's BEM with ElastoDyn structural module. Intending to investigate the effect of different structural stiffness on the wind

turbine wake flow, in addition to carbon fiber, we consider E-glass composite by changing the mass density and stiffness in the blade structural model.

Table 7: Blades construction materials

Material	Mass density [g/cm ³]	Young Modulus [GPa]
Carbon fiber	1.7	220
E-glass	2.55	70

The tip out-of-plane deflection for the Elastic E-glass is 4.24% of the blade length as opposed to the 1.91% of the blade length we had with the elastic carbon. The flexibility obtained is enough to replicate the increasing size of future wind turbines and evaluate the effect of this variation on the wake flow.

An additional simulation was performed with extreme flexibility under below-rated conditions, obtaining a mean tip displacement of 12.1% of the blade length. It is an extreme case, very far from the previous ones, and more points are necessary to conclude on a point where the advantage of using the coupling is higher than the cost. It should also be pointed out that the linear structural solver could encounter limitations at these deformation levels due to the small displacement assumption it is based on. The wake evolution, structural response, and rotor performance are evaluated under the two wind conditions obtained with the precursor. The wind turbine operational parameters for the below-rated and above-rated conditions are reported in Table: 8. In Table 8, θ indicates the pitch angle.

Table 8: Wind turbine operational parameters

	V_{hub} [m/s]	ω [rpm]	TSR	θ [°]
Below Rated	3.71	241	8.07	0
Above Rated	5.03	265	6.24	12.5

2.5.1 Below Rated Condition

Larsen et al. [55] found that the effective rotor area changes with the blade deformations. These effects cause a reduction in power output under conditions between the cut-in and cut-out wind speeds. In contrast, the effects under the above-rated conditions are related to the pitch angle setting and control techniques. Figure 17 shows the stream-wise mean velocity profiles at different positions downstream of the wind turbine. The velocity deficit and the recovery rate are underestimated within a turbulent flow field when the blade deformations are neglected. Significant variations are visible in the near wake up to 4D from the turbine and in the far wake at 8D. These effects are appreciable only when considering deflections above 4% of the blade length. Indeed, the extreme flexible case has the most significant velocity deficit in the near wake and the lowest in the far wake. At 6D, all the turbine configurations show a similar horizontal profile, but at 8D, the horizontal velocity deficit is lower for the two more flexible rotors. This behavior indicates that the recovery rate increases with the increase of blade elasticity. Figure 16 shows the mean streamwise velocity difference from the rigid case in a horizontal plane passing through the hub center. With the increasing blade flexibility, velocities grow at the wake's outer edge and decrease at the center in the near wake. The wake recovery seems to start earlier for the rigid and carbon cases, but the recovery rate is faster for more elastic blades in the far wake.

The rotor performance are reported in Table 9 and illustrated in Figure 18.

The resulting output values do not change very much for the rigid, Carbon, and E-glass cases. The effect of the flexibility on these parameters becomes essential only in the extreme elastic case.

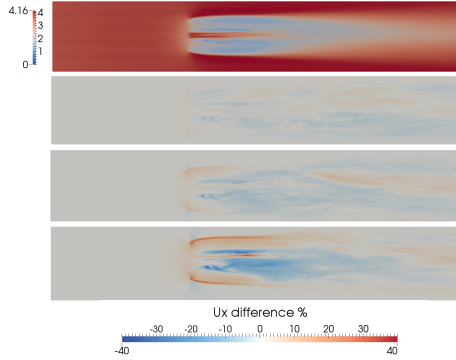


Figure 16: Streamwise mean velocity contour - velocity difference with respect to the rigid case (top contour) on a horizontal plane passing through the hub center for Elastic Carbon, Elastic E-glass and Extreme Elastic (from top to bottom) for below rated conditions

Table 9: Rotor performance below rated condition

	Power [W]	$\Delta\%^*$	Thrust [N]	$\Delta\%^*$	Torque [Nm]	$\Delta\%^*$
Experiment**	74.468		37.432			
Rigid	78.322		36.118		3.103	
Elastic Carbon	78.200	-0.16%	36.123	+0.01%	3.099	-0.13%
Elastic E-glass	77.877	-0.57%	36.046	-0.20%	3.086	-0.55%
Extreme Elastic	74.706	-4.62%	35.082	-2.87%	2.960	-4.61%

* Difference with respect to the rigid configuration

** Experimental data refers to a smooth wind tunnel condition

However, the trend already found in the literature [55] is confirmed; the rotor performance decrease with the increase in blade tip deflections. Large deformations affect the wind turbine's power and thrust output due to the change in effective rotor area.

The structural deflections, flap-wise forces, and flap-wise moment are listed in Table 10. The mean flap-wise shear forces are little affected by the flexibility, while the range between maximum and minimum values decreases for more elastic blades. Also, the blade flap-wise root moments decrease along with the increasing elasticity.

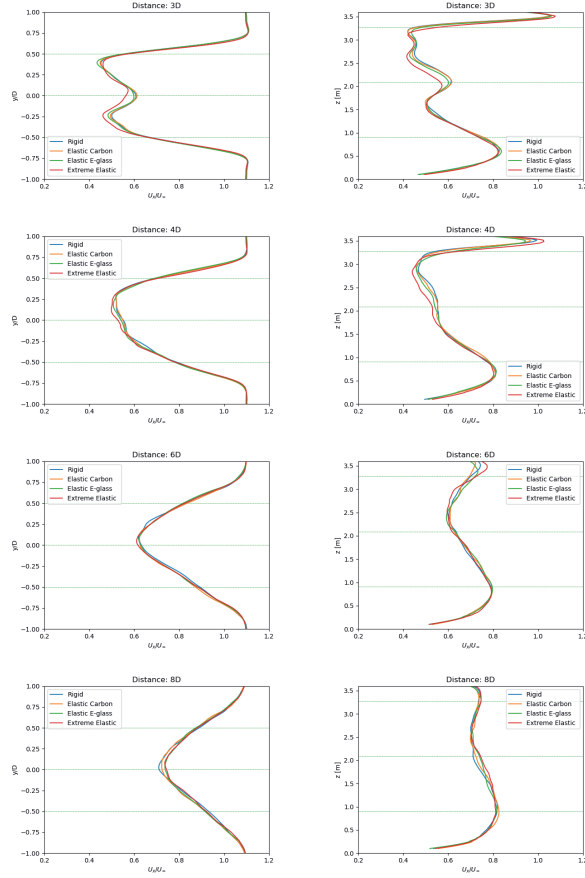


Figure 17: Streamwise mean velocity horizontal profile (left) and vertical profile (right) at different distances downstream the turbine (below rated conditions)

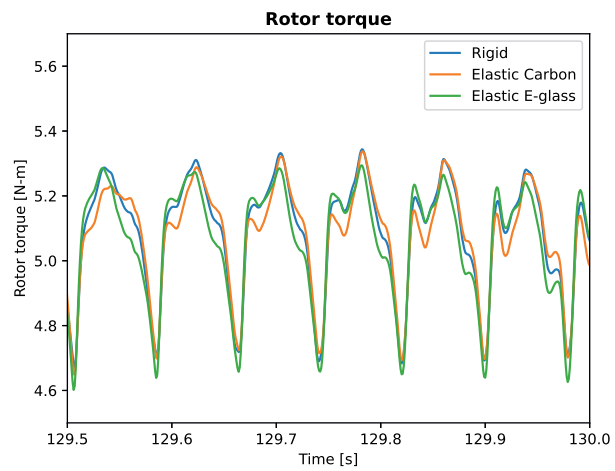
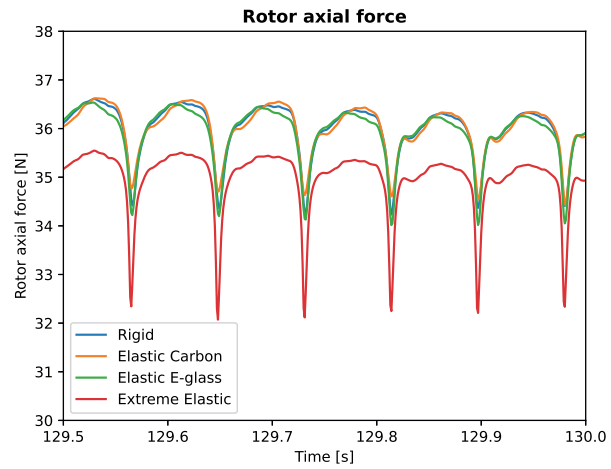


Figure 18: Rotor performance - Below rated condition

Table 10: Structural Deformations, Forces and Moments (below rated conditions)

	Rigid	Elastic Carbon	Elastic E-glass	Extreme Elastic
Tip Out-of-plane Deflection [m]				
Mean	0.0000	0.0226	0.0503	0.1435
% Blade R		1.91%	4.24%	12.11%
Maximum	0.0000	0.0261	0.0576	0.1529
Minimum	0.0000	0.0168	0.0394	0.1246
Blade Root Flapwise Shear Force [N]				
Mean	12.2	12.2	12.3	11.9
Maximum	12.9	14.3	13.8	12.9
Minimum	10.2	9.7	10.1	10.6
Blade Root Flapwise Moment [Nm]				
Mean	9.1	8.5	7.3	5.0
Maximum	9.5	10.0	8.2	5.4
Minimum	7.5	6.6	5.8	4.4

2.5.2 Above Rated Condition

Ma et al. [41] found that the underestimation of velocity and vorticity recovery rate becomes more pronounced with higher inlet velocities and more considerable tip deflections. Here, the pitch settings are set according to the values yielded from the controller used in the experimental tests. Therefore, the load and tip deflection are damped by pitch regulation techniques. The pitch angle used in this work is not the optimal value that would result from applying a controller directly to the simulated wind turbine. However, the effects of the variation are still visible. The resultant tip deformations are 1.75% and 3.79% of the blade length for the Carbon and E-glass rotors, respectively.

These values are smaller than the low wind correspondent ones, meaning that the pitch regulation effectively reduces the blade deflections. The extreme elastic case was not analyzed for the above-rated conditions. Table 11 and Figure 19 show the results in terms of performance.

Table 11: Rotor performance above rated condition

	Power [W]	$\Delta\%^*$	Thrust [N]	$\Delta\%^*$	Torque [Nm]	$\Delta\%^*$
Experiment**	120.643		36.326			
Rigid	134.211		36.113		5.066	
Elastic Carbon	133.928	-0.21%	36.082	-0.09%	5.055	-0.22%
Elastic E-glass	133.188	-0.76%	35.945	-0.47%	5.027	-0.77%

* Difference with respect to the rigid configuration

** Experimental data refers to a smooth wind tunnel condition

The power, thrust, and torque output are substantially the same for the three cases. The differences are in the temporal signals of these quantities shown in Figure 19, where the flexibility slightly changes the peaks' shapes. Figure 20 illustrates the wake deficit profile at different positions downstream of the turbine. The horizontal and vertical profiles for the rigid, Carbon, and E-glass rotors are nearly identical both in shape and magnitude.

Comparing Table 10 and 12, the flap-wise forces and moments are reduced passing from the below-rated to the above-rate conditions for the rigid, Carbon and E-glass cases. This means that pitch regulation is an efficient load-alleviation method.

Table 12: Structural Deformations, Forces and Moments (above rated conditions)

	Rigid	Elastic Carbon	Elastic E-glass
Tip Out-of-plane Deflection [m]			
Mean	0.0000	0.0207	0.0449
% Blade R		1.75%	3.79%
Maximum	0.0000	0.0248	0.0558
Minimum	0.0000	0.0148	0.0304
Blade Root Flapwise Shear Force [N]			
Mean	12.4	12.4	12.5
Maximum	13.7	14.5	14.8
Minimum	9.5	9.2	9.0
Blade Root Flapwise Moment [Nm]			
Mean	8.8	8.3	6.8
Maximum	9.6	9.8	8.2
Minimum	6.7	6.0	5.0

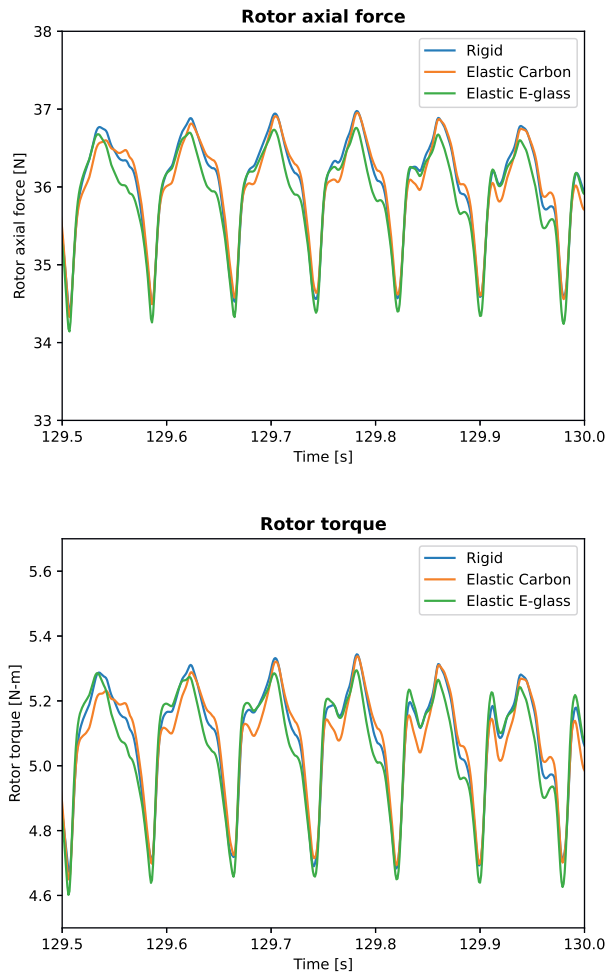


Figure 19: Rotor performance - Above rated condition

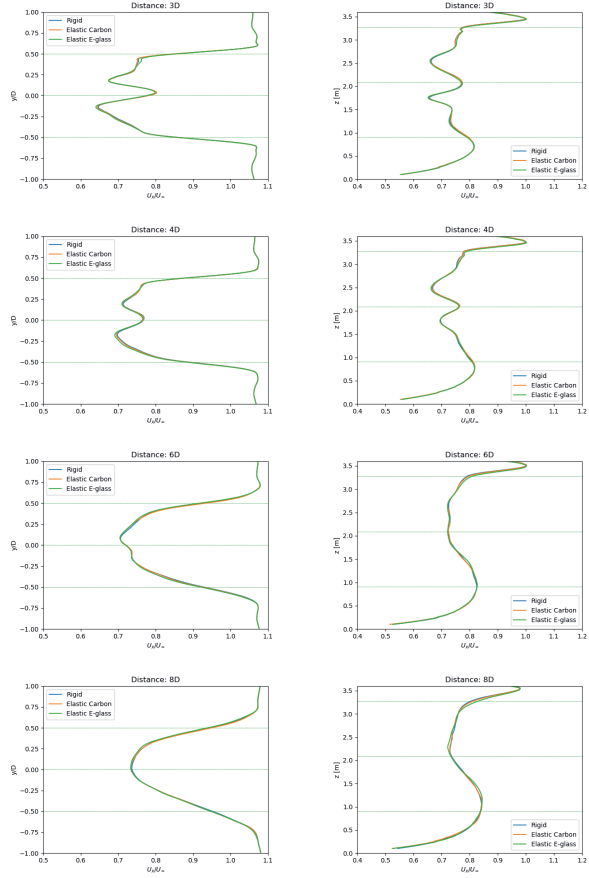


Figure 20: Streamwise mean velocity horizontal profile (left) and vertical profile (right) at different distances downstream the turbine (above rated conditions)

2.5.3 Nonlinear effects

As mentioned in section 2.2, the *BeamDyn* module is not yet integrated into the SOWFA-OpenFAST coupling. To have an idea of what exactly we are neglecting, we performed this analysis with the stand-alone OpenFAST software. The below-rated conditions and the standard material (carbon fiber) were considered. The smooth wind tunnel velocity profile is fed to OpenFAST through a tabulated velocity table.

The structural deflections, flap-wise forces and flap-wise moments are reported in Table 14. The tip deformations are underestimated when the non-linear effects are neglected. However, the difference is only 2% under low wind conditions. ElastoDyn slightly overpredicts the forces and moments, and the range between the maximum and minimum load peaks is greater than the *BeamDyn* one. The rotor performance are listed in Table 13.

Table 13: Rotor performance. Below-rated linear vs non-linear.

	ElastoDyn	BeamDyn	$\Delta\%$
Power [W]	69.71	69.66	-0.1%
Thrust [N]	34.25	34.02	-0.7%
Torque [Nm]	2.76	2.76	0%

Power, Thrust, and Torque are nearly the same for the two solvers. On the other hand, the computational cost of the non-linear structural solver is much higher. The time step required for a stable solution is 0.001 s for ElastoDyn and 0.00001 s for BeamDyn. The resultant execution times are very different; BeamDyn requires several hours to simulate 35 s, while ElastoDyn computes that simulation time in a few minutes. Therefore, it can be concluded that a non-linear solver is unnecessary in a low wind condition of this type.

The main difference between the two structural solvers lies in the number of degrees of freedom computed. ElastoDyn does not consider the torsional deformation at all, which could be extremely important for control algorithm simulations. Indeed, the blade pitch angle would change due to this type of deformation.

Therefore, further investigations considering a complete description of the structural deformation are needed, especially for above wind conditions, where the torsion effects are of primary importance for control purposes.

Table 14: Structural Deformations, Forces and Moments. Below-rated linear vs non-linear.

	ElastoDyn	BeamDyn	$\Delta\%$
Tip Out-of-plane Deflection [m]			
Mean	0.1208	0.1233	+2.1%
Maximum	0.1232	0.1253	+1.7%
Minimum	0.1185	0.1214	+2.4%
Blade Root Flapwise Shear Force [N]			
Mean	12.1	11.4	-5.8%
Maximum	11.7	11.6	-0.9%
Minimum	11.3	11.2	-0.9%
Blade Root Flapwise Moment [Nm]			
Mean	8.0	7.9	-1.3%
Maximum	8.1	8.0	-1.2%
Minimum	7.9	7.8	-1.3%

2.6 CONCLUSIONS

Wind turbine size is continuously increasing to extract more energy at a lower cost. However, larger rotors with enhanced flexibility increase aeroelastic effects that should be considered in an appropriate FSI framework. The simulation of the coupled aerodynamic and structural phenomena is a complex and computationally expensive task. Consequently, it is crucial to understand when it becomes strictly necessary.

Using a CFD-CSD framework, we performed several simulations varying the turbine structural stiffness to get insight into the aeroelastic effects on the wake flow. In this research, we considered two typical operational conditions to evaluate these effects: below-rated and above-rated conditions.

Under the below-rated condition, for the Polimi DTU10MW model, the results show minor differences between the rigid and elastic simulation for both wake flow and turbine performance. The velocity deficit is underestimated if flexibility is neglected for tip out-of-plane deflection starting from 4% of the blade length. However, rotor performance show between variations of 0.20% for the thrust and 0.57% for the power. The differences become even more significant for tip displacement of 12%, yielding variations up to 2.87% for the thrust and 4.6% for the torque. Under the above-rated conditions, the effects are very similar considering a pitch-regulated wind turbine. For tip displacement around 4% the changes in rotor performance are between 0.47 and 0.77%. In conclusion, for the considered model rotor, aeroelastic effects on global performance were negligible up to about 4% tip deflection, while wake differences became more evident at larger deflections. These results should be regarded as case-specific trends rather than general recommendations, and further work with more realistic rotor designs and experimental validation is required. In particular, further analysis should investigate higher tip deflections and account for non-linear effects properly.

3

THE EVM: AN IMPROVED APPROACH TO VELOCITY SAMPLING IN ACTUATOR LINE MODELS

Since all models are wrong, the scientist must be alert to what is importantly wrong. It is inappropriate to be concerned about safety from mice when there are tigers abroad.

George Box

Hybrid models like the Actuator Line are state-of-the-art when dealing with wind turbines numerical modeling. The main issue with these approaches is the estimation of the freestream velocity on the rotor plane. The aim of this thesis was to implement the EVM (a model for an accurate estimation of such velocity) in SOWFA (the main tool for wind farm simulations) and compare it to the local approach in terms of description of both turbine performances and wake development.

3.1 INTRODUCTION

3.1.1 Motivation and challenges

Any technical progress requires the support of data. This data can be obtained via experiments, but for wind energy applications, that is difficult and costly. This is why numerical simulations and, thus, reliable high-fidelity models - usually computational fluid dynamics (CFD) ones based on the Navier-Stokes (NS) equations - are needed.

Given the large Reynolds numbers and the multiple length scales involved, for wind turbines, let alone wind farms, direct numerical simulation (DNS) is unfeasible, and large eddy simulations (LES) on a fully resolved geometry is too computationally demanding to be used extensively.

An alternative to fully blade/turbine-resolved simulations is to parameterize the effect of the turbine on the flow. This can be achieved by means of body forces properly computed and projected into the flow field. The most popular approaches are the actuator disk model (ADM) and the actuator line model (ALM). The latter was introduced in Sorensen and Shen [44] and has since been validated [56], improved [57], discussed and compared to other methods [58] on many occasions.

The ALM can be very reliable, provided the user is particularly cautious in setting the model parameters. In fact, result quality can vary dramatically with grid resolution, projection function width, and velocity sampling method [59]. In particular, the value of the projection function width, ϵ , needs to be tuned, and the definition of the so-called free-stream velocity is ambiguous.

Another notion worth mentioning is the one of tip loss correction, which is needed because, in principle, the ALM is based on one-dimensional momentum theory in which forces are distributed continuously in the azimuth direction, corresponding to an infinite number of blades with no tip loss. The most commonly used correction is named after Prandtl [54], but more advanced options are available [45]. Tip losses are also connected to the regularization kernel in the sense that choices different from the standard 3D Gaussian function could result in a more realistic flow configuration at the tip.

These issues combined commonly result in difficulties in simultaneously predicting turbine power and thrust with this approach, which also impacts the prediction of the wake deficit downstream of the rotor.

3.1.2 Projection function width

A variety of rules for the choice of ϵ have been adopted in the literature. For example, it can be set to twice the cell dimension in the rotor area [59], which is a good rule of thumb only when considering big rotors. Others have tried to relate the value of ϵ to geometric quantities rather than having it as a function of spatial resolution. This can be done, for example, by setting ϵ equal to 0.035 times the rotor diameter [57], which requires very high resolutions or have its value vary along the blade and be equal to a quarter of the airfoil chord at that station [60]. Assuming as ground truth the chord-dependent ϵ definition, Martinez-Tossas and Meneveau [61] obtained, analytically, a sub-filter scale velocity model able to attain optimal accuracy with suboptimal kernel sizes.

3.1.3 Free-stream velocity

The main variable in ALM implementations is the free-stream velocity, used to evaluate the angle of attack and to dimensionalize the aerodynamic forces. We know that the sampled free-stream velocity should contain the deceleration caused by the rotor induction but not the blade-local flow effects [57].

Blade element momentum (BEM) methods normally use the undisturbed flow velocity. This approach is not very accurate, as the effects of induction are neglected, and the distance at which the sampling is done is a tunable parameter. With the whole flow field accessible in hybrid analytical-CFD solvers, the most obvious idea is to sample in the center of the cell containing the actuator line point (local sampling).

This idea is based on the assumption that the actuator line point is located at the center of the bound vortex cross-section, where the effect of the bound vortex itself is null [62]. The validity of this assumption is questionable for two reasons. First of all, a fundamental objection comes from the fact that Biot-Savart and Kutta-Joukowski's laws are formulated in potential flow theory, which can hardly be representative of a wind turbine's operating conditions and does not hold when using kernel functions different than the classic isotropic Gaussian one. Moreover, the lift generated by the bound vortex causes a local velocity angle increase (up-wash) in front of the considered point and a decrease (down-wash) behind it, meaning that there will be a strong gradient in velocity angle and that a small error in the sampling results in significant errors in angle evaluation.

Shives and Crawford [63] showed that this error, in CFD simulations, is always non-zero and that its magnitude depends strongly on grid resolution. They introduced the idea that the velocities induced across an actuator line resemble the ones predictable with a viscous vortex core model. Dag [64] further elaborated on that idea, demonstrating a very good agreement between a Lamb-Oseen [65] vortex core model and ALM swirl velocities. Significant progress was made by Meyer Forsting, Pirrung, and Ramos-García [66], who gave theoretical and practical proof of the fact that smearing the forces in ALM models produces a viscous core in the bound and shed vorticity of the line and suggested a vortex-based correction. In a follow-up paper [67], Meyer Forsting and Troldborg found that the error in the evaluated lift depends on the chord, on ϵ , and on the $\epsilon/\Delta x$ ratio. The subfilter-scale velocity correction presented in Martínez-Tossas and Meneveau [61] and shortly introduced in 3.1.2 can also be seen as a variant of a vortex-based correction. Kleine, Hanifi, and Henningson [68] observed that these methodologies introduce an error dependent on the difference of circulation between time steps and on the weighting/relaxation factors used.

Alternatives to local sampling with and without corrections are numerous and typically involve averaging over multiple cells or time steps. Among these, particularly notable is the Line Average method [69]. It samples the velocity at a number of points equally distributed along a circle centered at a quarter of the local chord. The reasoning is that the induced velocity at opposed circle point cancel each other. This method is simple and has shown good accuracy and robustness in several studies [70, 71]. However, the same considerations apply as with the local approach: potential flow theory does not hold for non-isotropic kernel functions. Other recent examples include the Lagrangian sampling [72] and the integral method [57]. The latter is considered state-of-the-art and will be described in section 3.2.2.

3.1.4 Research objectives and work outline

The gap we would like to fill with this study is to provide an elegant solution to both the mentioned issues at the same time:

1. evaluate the free-stream velocity in a way that is at the same time consistent with the physics and compatible with the numerics;
2. overall, make the turbine model less dependent on the ϵ value.

This is achieved by implementing the effective velocity model (EVM) in Simulator for Offshore Wind Farm Applications (SOWFA), which is currently the state-of-the-art framework for ALM simulations.

The EVM was first introduced in Schito and Zasso [73], implemented on the Politecnico di Milano in-house ALM code, and then used with success in following studies on both vertical axis [74] and horizontal axis [75] wind turbines. The reason for implementing the EVM in SOWFA was that, although the two codes have comparable accuracy and computational speed, SOWFA is more complete (atmospheric boundary layer solver, coupling with Fatigue, Aerodynamics, Structures, and Turbulence (FAST)) and more widely used (which also means more widely tested).

This chapter presents the validation of our implementation of EVM in SOWFA against BEM results and other actuator line models. The performance of our sampling method is assessed against local sampling and integral sampling [57] in predicting rotor performances (power and thrust), reducing

spurious oscillations in the local quantities (axial velocity and angle of attack), and evaluating the wake velocity deficit.

The chapter is organized as follows. Section 3.2 presents SOWFA and its ALM solver, then the EVM and its implementation. Section 3.3 describes the setup of the simulations of the DTU 10 MW turbine used for validation and comparison. Results are shown and discussed in Section 3.4. Finally, conclusions are drawn in Section 3.5.

3.2 METHODS AND TOOLS

This section first briefly introduces the actuator line model and gives a brief overview of SOWFA and its velocity sampling methods. Then, the motivation behind the Effective Velocity Model, the process behind its synthesis, and its implementation are described.

3.2.1 Actuator line model

The ALM was developed in order to overcome the limitations of the axisymmetric ADM, a concept that was already present in the basic aerodynamic description of wind turbines. The biggest limitation of ADM is that, since the force distribution is uniform on the disk, the influence of the blade is taken as an integrated quantity in the azimuthal direction. With the ALM, the forces, instead of being distributed uniformly on the disk, are applied to the flow field along rotating lines that correspond to the individual rotor blades. They can be modeled in a way that allows them to respond dynamically to changing conditions and can account for aeroelasticity when coupled to a structural code. This allows us to describe the wake's dynamics better and capture the tip vortexes and their influence on the induced velocities. However, smaller-scale phenomena, such as those involving the blade boundary layer, cannot be captured. That is the main disadvantage with respect to a fully resolved geometry, but also what makes it so computationally convenient since the description of the blades' boundary layer would require a much more complex mesh. Moreover, LES, which have been reported to present issues in the treatment of the near-wall region [76], can now be used more reliably. Two crucial aspects of the ALM that differentiate the many models available are:

- the sampling of the freestream velocity;
- the projection of the body force;

The sampled free-stream velocity V_{rel}^{2D} (we specified "2D" because, in the model, a two-dimensional airfoil is considered) is necessary to compute the angle of attack α). The variables in the following equations are shown in figure 21.

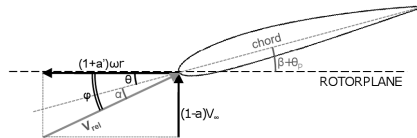


Figure 21: Velocities at the rotor plane

$$\vec{V}_{rel}^{2D} = \vec{V}_\infty - \omega r \vec{t} = V_\infty \vec{n} + (V_\infty - \omega r) \vec{t} \quad (15)$$

$$\vec{L} = \frac{1}{2} \rho (\vec{V}_{rel}^{2D})^2 C_L(\alpha) c \vec{t} \quad (16)$$

$$\vec{D} = \frac{1}{2} \rho (\vec{V}_{rel}^{2D})^2 C_D(\alpha) c \vec{d} \quad (17)$$

$$\phi = \angle \vec{V}_{rel}^{2D} \quad (18)$$

$$\alpha = \phi - \beta, \quad (19)$$

where \vec{V}_∞ is the undisturbed wind speed, ω is the rotor speed in radians/s, r is the radial distance from the hub, \vec{t} and \vec{n} are the tangential and normal vector, respectively, \vec{L} , \vec{D} , C_L and C_D are the lift and drag forces and the lift and drag coefficients, respectively, and ρ is the density of air. The angle ϕ is the flow angle, and β is the twist of the blade. A common choice for evaluating \vec{V}_{rel}^{2D} is sampling it directly in the cell containing the actuator line point.

The projection function is needed to smear the computed force over multiple cells. The most physical solution would be to apply them in the single cell containing the airfoil pressure center. However, this could be mathematically problematic since the sharp gradient generated could lead to strong spurious oscillations in the vicinity of the actuator line. The most common choice is to use a three-dimensional Gaussian smearing function that is isotropic in width and fixed along the blade span [56]. This makes the resultant body-force field around an actuator line appear like a cylindrical cloud surrounding the line. The function can be written as follows:

$$\eta^{RK}(r) = \frac{1}{\epsilon^3 \pi^{\frac{3}{2}}} \exp\left(-\frac{d^2}{\epsilon^2}\right) \quad (20)$$

Where d represents the distance of the considered cell from the application point and ϵ is the width of the Gaussian distribution. In every domain cell, the total inserted force will be equal to the following:

$$f(x) = \sum_i f_i \eta^{RK}|x - x_i| \quad (21)$$

3.2.2 SOWFA

SOWFA [46] is a set of libraries, solvers, boundary conditions, and tools specific to wind turbine simulations and constitutes an extension of OpenFOAM. It was originally developed at the national renewable energy laboratory (NREL) and can be coupled to the structural solver of NREL's wind engineering tool OpenFAST. SOWFA solves the Navier-Stokes equations numerically using, for example, a Pressure-Implicit with Splitting of Operators (PISO) algorithm. The latter is modified with the addition of body forces that parametrize the effect of the wind turbine on the flow using a state-of-the-art ALM, and an atmospheric boundary layer (ABL) solver that allows running precursor simulations to provide a turbulent inflow to wind farm simulations. The linear systems that arise when discretizing the implicit equations are solved using preconditioned iterative solvers.

SOWFA's ALM provides three different sampling methods for the free-stream velocity:

- cellCenter: considering the current point of the actuator line, it uses the value at the nearest neighbor cell center;
- linear: uses linear interpolation from the cell within which the point lies and neighboring cells;
- integral: determines the free-stream velocity using an integral of the velocity field weighted by the force projection function[57].

Concerning the projection function itself, the only option currently implemented is the already described isotropic three-dimensional Gaussian.

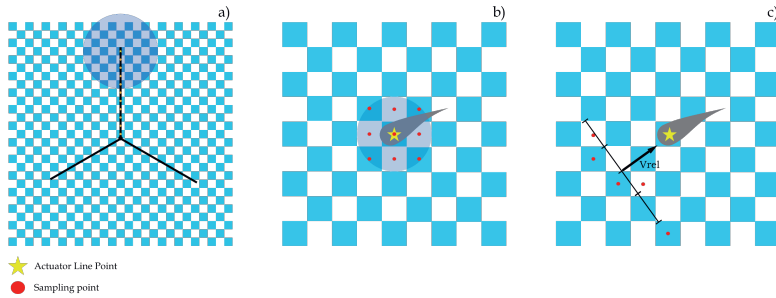


Figure 22: The first sub-figure (a) represents the rotor plane and the blade discretization. The purple circle in sub-figure a is actually a sphere and corresponds to the grey one in sub-figure b. It is centered on a given actuator line point and has a radius equal to ϵ . Sub-figures b and c zoom in on a single actuator line point and show how the sampling happens. In particular, we have a representation of the integral sampling (b) and of the **EVM** sampling (c). In sub-figure b, the sampling points are the centers of the cells intersected by the gray sphere. In sub-figure c, the sampling line is perpendicular to the relative velocity, one cell and a half upstream from the chosen actuator line point and five cells long.

3.2.3 The Effective Velocity Model

The main idea behind the **EVM** is that it is better to evaluate the angle of attack α and the effective velocity on the rotor plane by averaging the velocity sampled on a segment, and thus on multiple points, rather than sampling a single point like in the local approach. The segment is positioned slightly upstream of the rotor and perpendicular to the mean relative velocity direction.

Like the integral approach, the **EVM** is based on spatial averaging. This can be particularly suitable for turbulent cases where the entire unsteady incoming flow information cannot be characterized with a single sample. As explained in 3.1.3, the weakness of the more straightforward local approach comes from the assumption of null vortex-induced velocity in the sampling point.

The synthesis of the **EVM** required a definition of the sampling segment in terms of position (with respect to the considered actuator line point), length, and direction (with respect to both the blade and the incoming flow) and an evaluation of how sampling slightly upstream might change the angle of attack. The model is semi-empirical since these quantities had to be tuned experimentally.

The calibration was done through 2D simulations of a NACA0012 airfoil at different angles of attack. The angle of attack for a blade section typically varies between 0° and 10° , so, for the calibration, $\alpha_\infty = 3^\circ, 6^\circ, 9^\circ$ was considered. It was documented, together with the implementation of the **EVM** in an in-house **ALM** code from Politecnico di Milano, by Bernini and Caccialanza in their Master thesis [77] in Schito and Zasso [73]. It resulted in the following:

- distance: the optimal value for the distance between the sampling line and the actuator line was found to be equal to $1.5 h_{cell}$ where h_{cell} is the characteristic cell dimension. This value was obtained through a comparison between **ALM** and a fully resolved simulation on a test airfoil at fixed wind conditions as the one that minimized the error in the evaluation of the effective velocity;
- direction: the direction of the sampling line is orthogonal to the mean relative velocity direction. This way, spurious contributions coming from the translational motion can be avoided;
- length: the obtained optimal value for the sampling line length is $5 h_{cell}$. The optimization procedure follows the same approach we have seen for the distance, but this time, the focus is on the angular deviation of the flow from the undisturbed one.

- correction for the angle of attack:

$$\begin{cases} v_{\infty} = v_{EVM} \\ \Delta\alpha = \alpha_{EVM} - \alpha_{\infty} = \frac{c}{h_{cell}}(1.2553 - 0.0552C_D)C_L \end{cases} \quad (22)$$

This correction quantifies the distortion induced on the flow by the wind-blade interaction at the sampling distance. The modulus of the velocity does not vary. The angle of attack increases with the intensity of the bound vorticity (so proportionally to the lift coefficient). One thing to be remembered is that the obtained correction is valid only for the chosen configuration of the sampling line. In particular, it is inextricably related to the length of the sampling line.

Bernini and Caccialanza[77], after the calibration and before testing the EVM on a 3D case, demonstrated the effectiveness of the model respectively:

- on a NACA63.4, an asymmetric airfoil (the NACA0012 was symmetric);
- with oscillating inflow conditions;

thus extending its validity. Tests were also done with lift and drag combinations in a wide range without considering specific airfoils.

The 3D case that they presented was based on experiments performed in the Politecnico di Milano wind tunnel on the scaled mode of a Vestas V90 3MW wind turbine [78], which had a rotor diameter of 2 m. The EVM implementation does not change with respect to the 2D case, and at each time step, the incoming velocity for an actuator line point at a given radial position is obtained by averaging the values over the sampling line and correcting the direction as prescribed.

Two meshes with different levels of refinement (0.1 m and 0.05 m) were considered at first, and the coarsest was adopted in the following since differences were negligible. The solver was then tested under different tip-speed ratio (TSR) and a fixed pitch angle. This resulted in angles of attacks near the stall region and higher discrepancies with the experimental results in correspondence with the lowest TSR.

3.3 NUMERICAL SETUP

This section presents the setup used to test and assess the newly implemented method. We describe the reference turbine and the available data; we then detail every step of the CFD setup and the changes for the various tested configurations.

3.3.1 The NREL 5-MW reference turbine and the operating conditions

The "NREL offshore 5-MW baseline wind turbine" [79] (NREL 5-MW) is a reference turbine that was conceptualized including design information from manufacturers and publicly available data from other concepts projects. Researchers in the past decades have widely used it for testing and validating methods. Performance predictions in the original report were obtained with FAST [49], a modular aero-servo-elastic code. This makes simulating the turbine in SOWFA easy since many FAST input files can be easily adapted if not used directly. Table 15 summarizes the main properties of the turbine.

3.3.2 Domain and space discretization

In Martinez-Tossas *et al.* [80], a standard test case for the NREL 5-MW is defined and simulated with four different ALM codes. The considered domain is a parallelepiped with dimensions $24D \times 6D \times 6D$ (with D indicating the turbine diameter), and the turbine hub is positioned $3D$ away from the top, bottom, and inflow plane.

Table 15: NREL 5-MW main geometrical and control parameters

Rating	5 MW
Rotor Orientation, Configuration	Upwind, 3 blades
Control	Variable Speed, Collective Pitch
Rotor, Hub Diameter	126 m, 3 m
Hub Height	90 m
Cut-In, Rated, Cut-Out wind speed	3 m/s, 11.4 m/s 25 m/s
Cut-In, Rated rotor speed	6.9 rpm, 12.1 rpm
Rated Tip Speed	80 m/s
Overhang, Shaft Tilt, Precone	5 m, 5°, 2.5°

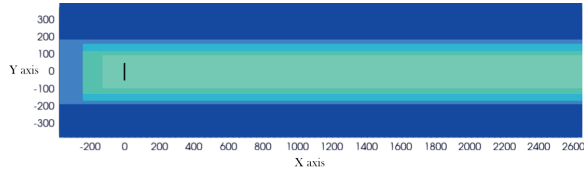


Figure 23: Two-dimensional visualization of the domain with the line in black in the middle representing the turbine and the rectangles representing the refinement areas whose dimensions are indicated in Table 26.

Thanks to the fact that the actuator line does not require the solution of the blade boundary layer, the mesh is almost as simple as it can be: it is obtained with a block mesh and a number of local refinements applied on a cylinder whose base has the same diameter of the turbine and whose length starts from a bit upstream of the turbine and ends at the end of the domain. Each refinement halves the characteristic length of the refined cell.

Developers [46] and users have suggested that there should be at least 20 cells along a rotor radius, which becomes at least 50 if we want to resolve tip/root vortices. The mesh considered for this study has cells with a characteristic dimension of 33.6 m on the outer part of the domain. We applied four refinements to this base mesh, resulting in the characteristics listed in table 26. Table 17 adds details on the refinement zones, and a simple visualization of the domain is given in figure 23.

Table 16: Details on the mesh used for the NREL-5MW Test Case

Global refinements	0
Local refinements	4
Number of cells	9907187
minimum cell dimension [m]	2
Cells along rotor	64

3.3.3 Numerical schemes and boundary conditions

SOWFA describes the flow with an unstructured, collocated variable, finite-volume formulation. The accuracy in time and space is second order. The filtered momentum equation is solved along with an elliptic equation for the pressure that enforces continuity. A Smagorinsky subgrid-scale model with a fixed C_s coefficient is used. We impose a uniform inflow with an 8 m/s wind speed and a zero

Table 17: Details on the refinement zones. The zones are cylindrical, centered at the rotor hub, and extend to the end of the domain. The values on the first line are the ratios between cylinders and rotor diameter, and the ones on the second indicate how far upstream of the rotor plane the zone starts. This distance is expressed in diameters, with $D = 126$ m.

Refinement	1	2	3	4
$\frac{D_{cylinder}}{D_{rotor}}$	1.5	2	2.5	3
Upstream length	2 D	2.5 D	2.5 D	3 D

normal pressure gradient at the inlet. At the outlet, we have zero normal gradient of velocity and fixed pressure. The lower surface-boundary conditions are based on Monin-Obukhov [81] similarity theory, which is standard practice in the atmospheric LES community. The upper boundary is a stress-free, rigid lid, and the lateral boundary conditions are set to zero gradient with no penetration. These boundary conditions are summarized in Table 18.

Table 18: NREL 5MW test case boundary conditions

patch	U	P	k	nuSgs
lower	slip	zeroGradient	zeroGradient	zeroGradient
upper	slip	zeroGradient	zeroGradient	zeroGradient
west	fixedValue	zeroGradient	fixedValue	fixedValue
east	inletOutlet	fixedValue	zeroGradient	zeroGradient
south	slip	zeroGradient	zeroGradient	zeroGradient
north	slip	zeroGradient	zeroGradient	zeroGradient

3.3.4 Time discretization

The time step must be set correctly to avoid numerical instabilities in the simulation.

Here a Courant–Friedrichs–Lewy number (CFL) based on the rotation speed at the tip of the blade is used to choose an appropriate time step. It is defined as

$$CFL_{tip} = \frac{\omega R \Delta t}{\Delta_g} \quad (23)$$

where ω is the wind turbine rotational speed, R is the blade radius and $\Delta_g = \sqrt[3]{\Delta_x \Delta_y \Delta_z}$ is the equivalent cell dimension.

This choice is motivated by the fact that scaled wind turbines rotate very fast. Maintaining this CFL at a value smaller than one should prevent the blade tip from crossing more than one cell per time step and guarantee an equal number of force calculations per rotor revolution [82]. In fact, if the time step is too large, the forces can be computed asymmetrically or only in specific positions, introducing oscillations of the loads or vibrations of the structure. For all the simulations in this study, we consider a time step of $\Delta t = 0.015$ s which always guarantees the respect of the condition.

3.3.5 ALM parameters

Actuator line simulations require some additional knowledge for proper implementation with respect to normal CFD ones. As said in subsection 3.3.4, the time discretization must ensure that the blade tip

does not cross more than one grid cell per time step. The choice of the correct value for the projection function width ϵ is of the utmost importance in an ALM simulation. If the chosen value is too large, the actuator line model will appear to recover an aerodynamic power above the Betz limit, and if it is too low, the predicted power will be well below measurements or BEM calculations.

Turbine quantities such as lift and drag forces depend heavily on the value of ϵ . In the literature, there is no consensus on how to choose it correctly. Churchfield *et al.* [57] claim that a value of 0.035 times the rotor diameter works well for big enough turbines, Shives and Crawford [63] found it to be optimal when the ratio ϵ/c , where c is the local chord, is equal to 0.25, while in many other works, it has to be tuned to the mesh dimension in the rotor area. In this work, when comparing the sampling methods, the choice was to set ϵ as twice the mesh dimension, as suggested in Sorensen and Shen [44]. The choice adopted in the validation will be made explicit and explained in Section 3.4.1. This is somewhat far from the optimum defined in Shives and Crawford [63], but reaching it would require the use of very fine meshes. Other relevant information on the considered simulations is that the chord and twist as a function of the blade radius are linearly interpolated from tabular data. The number of actuator points is 64.

3.4 RESULTS

With the setup described in Section 5.3.3, several simulations were run with different objectives. The operating conditions are the same as those considered in Martinez-Tossas *et al.* [80]. In the validation part, this is also the case for the ALM parameters. The latter are then modified for the comparison of the different sampling methods. In particular, we compare EVM results to the ones obtained with three other popular sampling methods with a $\frac{\epsilon}{\Delta x}$ equal to two. Finally, we keep the base mesh and focus on the sensitivity to the force projection by varying the ϵ over Δx ratio.

3.4.1 Method validation

In Martinez-Tossas *et al.* [80], SOWFA's ALM was validated on the setup described in 5.3.3 against three different CFD codes: EllipSys3D [82], LESGO [83] and SP-Wind [84]. The BEM data from the NREL 5-MW report [79] was used as a reference. All cases were run with a fixed value of $\epsilon = 10$, which is very big. This was done to obtain very smooth results. Close agreement of the results amongst the codes was shown for quantities along the blades and in the near-wake.

Neither the CFD simulations nor the BEM code employed tip corrections. The EVM was also previously validated when implemented in the Polimi ALM code [73]. Thus, our validation of the EVM implementation in SOWFA was done by means of a cross-comparison with the results of Martinez-Tossas *et al.* [80]. Figure 24 shows time-averaged quantities along the blade. The quantities compared are the axial velocity, normalized with respect to the inflow velocity U_∞ , the angle of attack, and lift and drag forces normalized by length ($F_L^* = F_L/wD\rho U_\infty^2$, where w is the width of the current blade section, ρ is the air density, D is the rotor diameter).

We can observe that, for all the codes considered, the trends in terms of angle of attack and forces are correctly reproduced by our implementation. However, the predicted values of axial velocity differ from the other approaches (Figure 24, top left). This is explained by the fact that, while other codes use some version of the local approach, for the EVM, the velocity shown in figure 24 is sampled upstream. Thus it is completely normal for it to be significantly higher. This difference is especially relevant in the middle part of the blade.

It is important to understand that this is not the velocity used to compute the forces: the angle of attack must be corrected to take the fact that we are sampling upstream into account: the presence of a profile induces only a deflection on the incoming flow so, while the absolute value of \vec{V}_{rel}^{2D} will be the same, its axial component will not. We can observe that the angle matches very well the BEM reference, even in the area where the other approaches were not as accurate. Bigger quantitative differences can be spotted in the force prediction, especially the lift. Small differences in the angle of

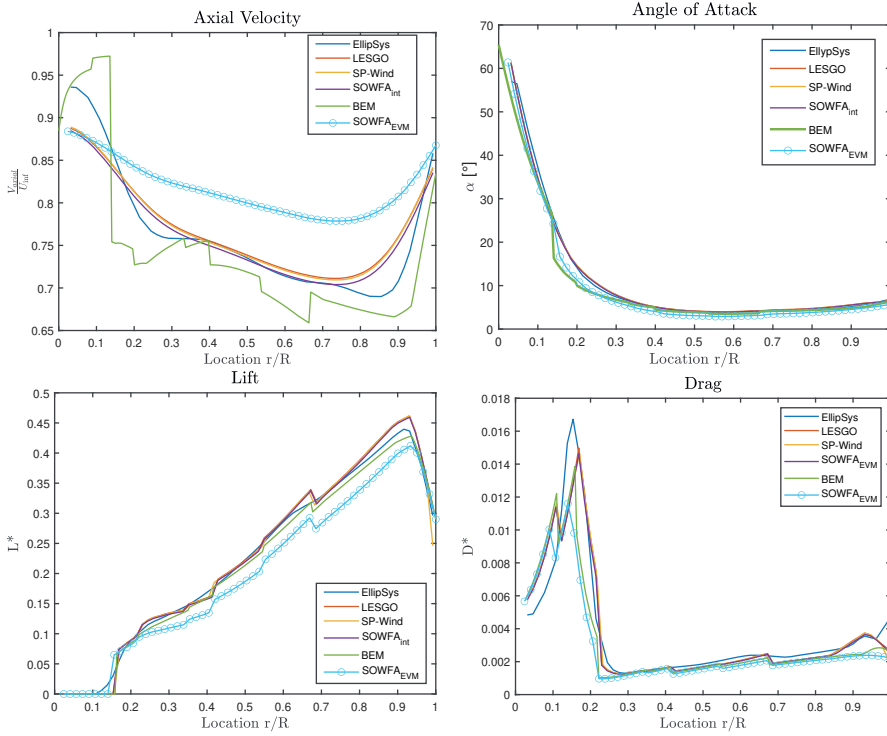


Figure 24: Spanwise evolution of the axial velocity (top left, normalized with the inflow velocity), angle of attack (top right), adimensional lift (bottom left), and drag force (bottom right), evaluated with four different LES codes. The EVM axial velocity is the one sampled upstream and not yet projected with the new angle of attack. All quantities are made non-dimensional. The BEM results are included as a reference.

attack result in a significant over-prediction of forces for the traditional methods in the second half of the blade span and in a consistent under-prediction for the EVM along the whole span. Apart from the different sampling, one justification for the significant quantitative differences is that the EVM gives results that are less dependent on the ϵ value (as will be proved in Section 3.4.3).

3.4.2 Comparison between different sampling methods

It is interesting to assess the EVM against the other sampling methods available in SOWFA. To do that, we consider the same setup, but we set the ϵ value to a more reasonable $2\Delta x$. Figure 25 shows the time evolution of the angle of attack evaluated with the four methods on three different points: one located at the blade's root, one in the mid section, and one on the tip.

The time-dependent signal is periodic because of the asymmetry of the rotor plane: the nacelle is tilted, and the blades are pre-coned.

Looking at figure 25, and in general, in time-varying plots, we recognize spurious oscillations. We can observe that, as we move along the blade, they increase in frequency and decrease in amplitude (the blade passes through more cells). These oscillations are always present in ALM simulations; they depend strongly on the spatial discretization and chosen sampling method. In that sense, all sampling methods perform better than the cell-centered one: the linear because of interpolation, the EVM, and the integral because of spatial average. For the methods with no spatial average, in Jha *et*

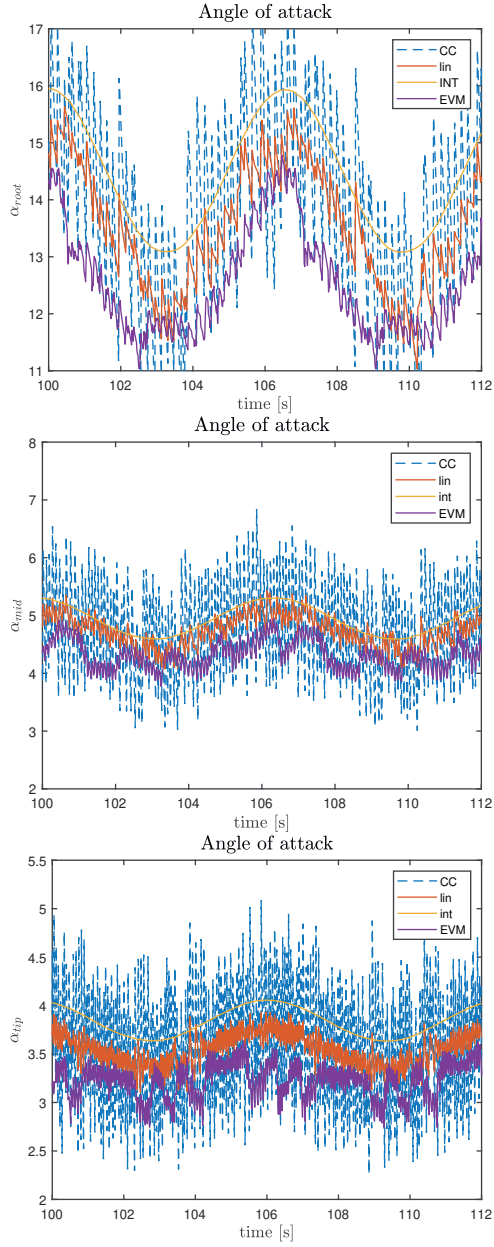


Figure 25: Time evolution of the angle of attack evaluated with the cell-centered (dashed blue), linear (orange), integral (yellow), and *EVM* (purple) approach on a point located at the root (left), mid (middle), and tip (right).

al. [85], the issue was observed and solved by just intervening on the numerics: they started by using different blends of second-order linear and first-order upwind interpolation upstream of the actuator

and elsewhere, which worked for a uniform grid (stretched grids require ulterior attention) and did not produce excessive artificial diffusion. Xie [72] also recently tackled the issue by integrating a Lagrangian averaging in time to the sampling.

These oscillations are, thus, only related to the line crossing different cells (the frequency increases towards the tip, where the blades travel faster). We chose not to try to eliminate them since they have no effect on the global quantities that we are interested in.

The subsequent step was to look at the spanwise evolution of the local quantities. The values at each blade station were evaluated by averaging over the last third of the simulation time. Figure 26 shows the evolution of the angle of attack and the axial velocity. The axial velocity is significantly higher. Again (as in 3.4.1), it is the one sampled upstream, not yet corrected and it is not the one used to compute the forces.

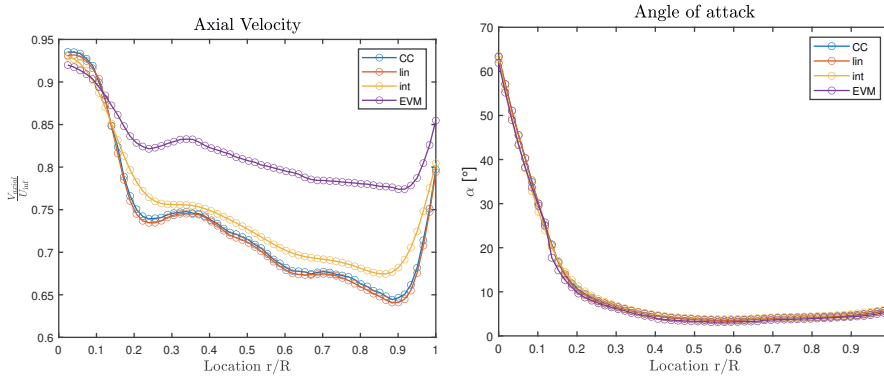


Figure 26: Spanwise evolution of the axial velocity (normalized with the inflow velocity) and angle of attack evaluated with the cell-centered (blue), linear (orange), integral (yellow), and EVM (purple) approach. The EVM axial velocity is the one sampled upstream and not yet projected with the new angle of attack.

Differences amongst the methods in evaluating the angle of attack can be appreciated when considering fewer actuator line points (it must be noted, though, that these differences become negligible for integral quantities). This is shown in figure 27. Figure 28 shows the adimensional lift and drag forces along the span. As in section 3.4.1, the lift predicted by the EVM is significantly lower. The drag is very close, but, with the EVM, the peak at around 15% span is not as pronounced. These differences will ultimately translate to differences in the global quantities and in the wake.

While looking at local quantities allows us to understand where the methods differ, ultimately, we are interested in global quantities such as power and thrust. The actuator line quite famously fails at accurately predicting both of them at the same time. The closest it gets to one, the farthest from the other [86].

Martinez-Tossas *et al.* [86] featured an experimental validation of the ALM against experiments performed at the low-speed wind tunnel of The Norwegian University of Science and Technology [87]. Across the tested TSR range $TSR \in [3, 4, 6, 9, 12]$, the thrust coefficient was under-predicted by 20 – 25%. This is consistent with the curves represented in figure 29, with the difference that the EVM seems to match the power perfectly. Since thrust is the quantity that most affects the wake, it is a priority to have a reliable prediction, especially when working in a wind farm environment. The EVM definitely fails at that, but so does the ALM in general. One possible explanation for the thrust under prediction is that we do not model the nacelle to remain consistent with the reference study [80]. If we did, we would see a change in both aerodynamic coefficients. In particular, drag would always increase, and lift would decrease normally and increase if stall conditions occur. When drag increases, thrust does too.

The effect of the thrust under-prediction can be quantified by looking at wind profiles in the near wake. Figure 30 shows the profiles at 1, 2, and 3 diameters downstream of the rotor plane. The

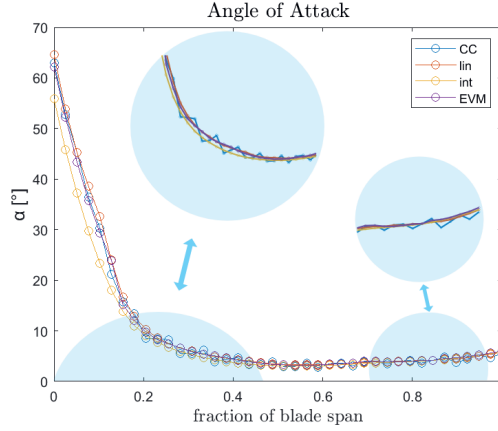


Figure 27: Spanwise evolution of the angle of attack, evaluated with the cell-centered, linear, integral, and [EVM](#) approach, when considering 40 points along the blade. The blue circles represent zoomed-in areas.

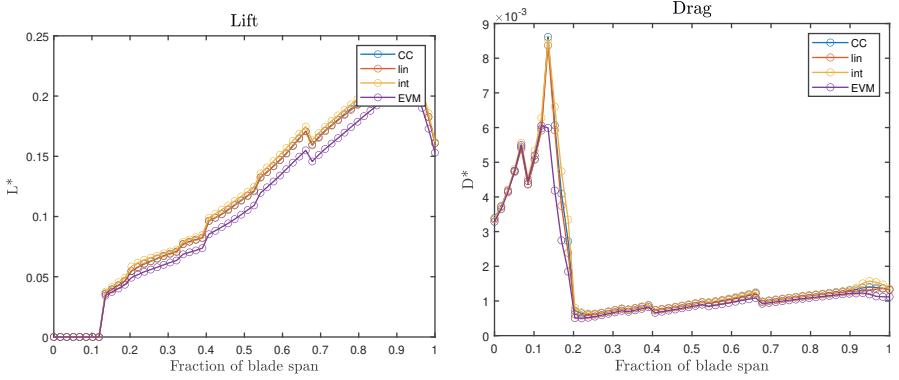


Figure 28: Spanwise evolution of the adimensional lift and drag forces evaluated with the cell-centered (blue), linear (orange), integral (yellow), and [EVM](#) approach (purple).

axial component of the velocity was averaged over the last 50 s of the simulation and divided by the reference wind speed of 8 m/s. We can see that the resulting shape for the cell-centered and linear methods are almost indistinguishable.

At all distances, the lower thrust predicted by the [EVM](#) results in a smaller deficit, with the wind speed never going below half the reference one.

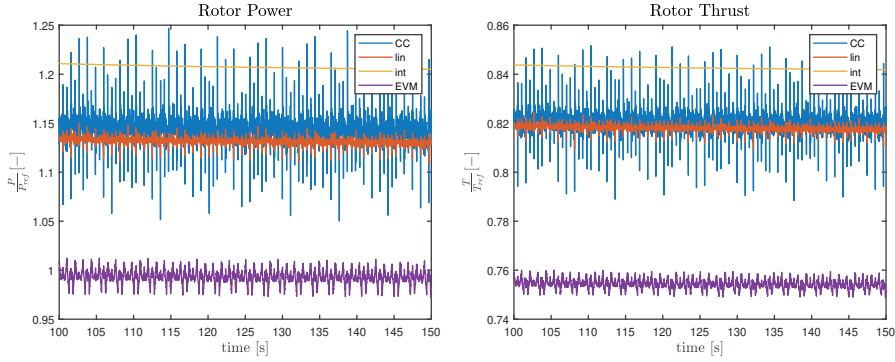


Figure 29: Time evolution of the rotor power and rotor axial force evaluated with the cell-centered, linear, integral, and **EVM** approach. Reference values from the [NREL 5-MW github \[88\]](#).

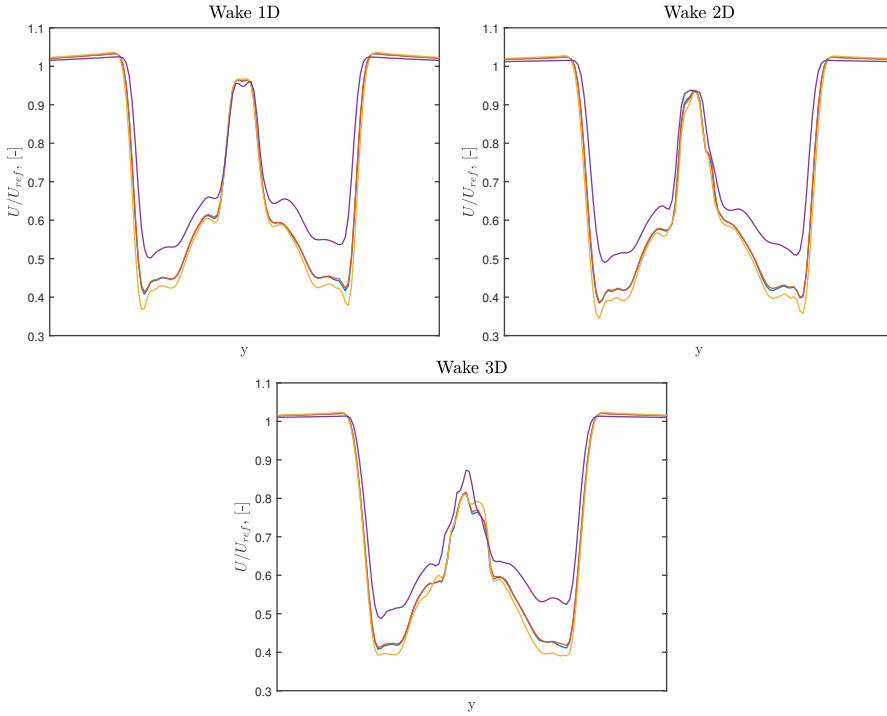


Figure 30: Non-dimensionalized wind profiles on planes parallel to the rotor plane. The planes are positioned at 1, 2, and 3 diameters downstream of the rotor, respectively.

3.4.3 Method sensitivity to force projection

We discussed in section 3.1 how, together with the velocity sampling, the main issue when using hybrid **CFD** methods for wind turbine simulation, such as the actuator line and the actuator disk, is the choice of the regularization kernel width ϵ . The two issues are not entirely decoupled: the velocity sampled in a certain point will be influenced by a force that has been smeared with a certain regularization kernel. Previous attempts at addressing the tunability of ϵ have gone in the direction

of either finding an optimal value, using it when possible [86] and correcting for it when not [61], or projecting in a way that is more physics-informed. For example, the latter can be done by considering a kernel that is non-isotropic and has coordinates in the chord-wise, thickness-wise, and radial directions that depend on the blade chord length, the maximum thickness length, and the actuator element width and vary along the span [57].

Another option would be to sample in a way that makes the results more robust to the ϵ choice. In this part of the study, we decided to compare the integral and EVM sampling methods based on this characteristic.

Since the integral method finds the free-stream velocity by integrating the velocity field weighted by the force projection function, we certainly do not expect its dependence on the projection function width to be negligible. Figure 31 shows how the power and thrust vary with the choice of the ϵ/Δ_x ratio. Tables 19 and 20 add quantitative information to the qualitative one given by the figure.

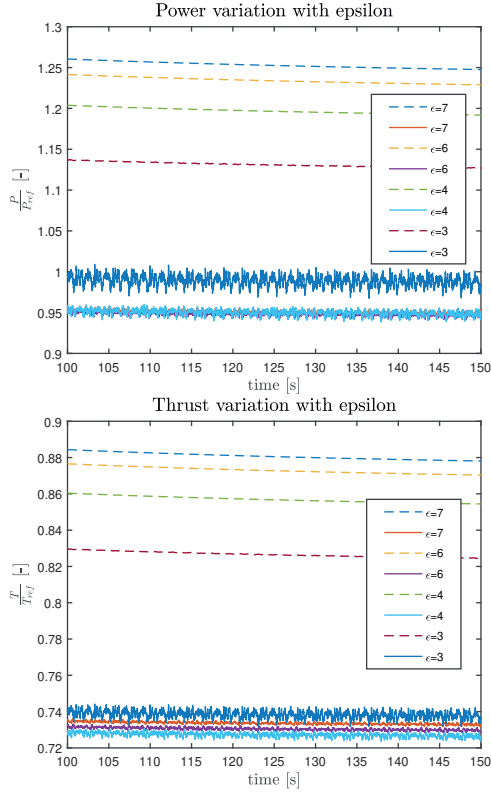


Figure 31: Time evolution of the rotor power and rotor axial force evaluated with the integral (dashed line) and EVM (solid line) approach with varying ϵ values. Reference values from the NREL 5-MW github.

Given a constant $\Delta x = 2$, the considered ϵ values are 3,4,6,7 with a value of 4 being considered as base case. Percentage errors are computed with respect to the base case results. We can see that the EVM predicts the same power regardless of the epsilon. The only exception is the simulation with $\epsilon = 3$. This is because the $\frac{\epsilon}{\Delta x}$ ratio is lower than the minimum suggested in Mikkelsen [82] to avoid numerical issues.

Thrust predictions are less consistent (and still very inaccurate), but the advantage of using the EVM is still very clear. When plotting the power signals in time for these simulations (like in Figure 31, we also see that the EVM curves converge faster.

Table 19: Mean power values normalized with respect to the reference in Jonkman [79] for the integral and EVM sampling with different values of ϵ . The percentage errors are computed by taking, for each method, the ratio evaluated with $\epsilon = 4\text{m}$, corresponding to a $\frac{\epsilon}{\Delta x} = 2$, as the correct one.

	$\epsilon = 3 \text{ m}$		$\epsilon = 4 \text{ m}$		$\epsilon = 6 \text{ m}$		$\epsilon = 7 \text{ m}$	
	$\frac{P}{P_{ref}}$	$\Delta\% \text{ error}$	$\frac{P}{P_{ref}}$	$\Delta\% \text{ error}$	$\frac{P}{P_{ref}}$	$\Delta\% \text{ error}$	$\frac{P}{P_{ref}}$	$\Delta\% \text{ error}$
integral	1.131	-5.51%	1.197	-	1.233	3.01%	0	4.85%
EVM	1	5.05%	0.952	-	0.949	-0.32%	0.953	0.11%

Table 20: Mean thrust values normalized with respect to the reference in Jonkman [79] for the integral and EVM sampling with different values of ϵ . The percentage errors are computed by taking, for each method, the ratio evaluated with $\epsilon = 4\text{m}$, corresponding to a $\frac{\epsilon}{\Delta x} = 2$, as the correct one.

	$\epsilon = 3 \text{ m}$		$\epsilon = 4 \text{ m}$		$\epsilon = 6 \text{ m}$		$\epsilon = 7 \text{ m}$	
	$\frac{T}{T_{ref}}$	$\Delta\% \text{ error}$	$\frac{T}{T_{ref}}$	$\Delta\% \text{ error}$	$\frac{T}{T_{ref}}$	$\Delta\% \text{ error}$	$\frac{T}{T_{ref}}$	$\Delta\% \text{ error}$
integral	0.826	-3.5%	0.856	-	0.873	1.99%	0.879	2.69%
EVM	0.740	1.78%	0.727	-	0.730	0.41%	0.734	0.96%

3.4.4 Power curve

All results presented refer to the same flow and operating conditions. If we want to prove the method's robustness, a further step would be to try and match the power and thrust curves reported in Jonkman [79]. Apart from the operating conditions already tested, we ran simulations across the entire operational range. It must be noted that in these simulations, we did not activate the turbine controllers and limiters present in SOWFA but rather imposed the theoretical conditions as per reference. Once the wind speed was chosen, the rotational speed was fixed based on the corresponding TSR, and the collective pitch of the blades was also modified accordingly, as detailed in table 21.

Table 21: Tested operating conditions.

	$U_\infty \text{ [m/s]}$	$\omega \text{ [rpm]}$	$\beta [^\circ]$
below rated 1	6	6.88	0
below rated 2	9	10.32	0
rated	11.4	12.1	0
above rated 1	15	12.1	10
above rated 2	18	12.1	15
above rated 3	22	12.1	20

Figure 32 shows the theoretical power and thrust curves and the predictions obtained with the EVM and the integral sampling. In the below-rated range (including the conditions considered in the rest of the study), the EVM matches the power closely and underestimates the thrust. By contrast, the integral overestimates the power (slightly) and also underestimates the thrust.

Starting from the rated condition, both methods show significantly lower accuracy in the power prediction while maintaining a similar behavior for the thrust. The decreasing trend for the power suggests that the given pitch angle fails in avoiding stall. Its overestimation with the integral approach is consistent with the results in Martinez-Tossaz *et al.* [86]. We believe this happens because the velocity gradients introduced by the smearing are stronger in highly loaded conditions so the integral method will overestimate the free-stream velocity. Its dependency on the smearing function is even stronger. On the contrary, by construction, the EVM samples the velocity upstream and accounts for

it with an angle of attack correction calibrated for attached flow, at stall amplifies the underprediction of the angle of attack, of the lift, and ultimately of the power.

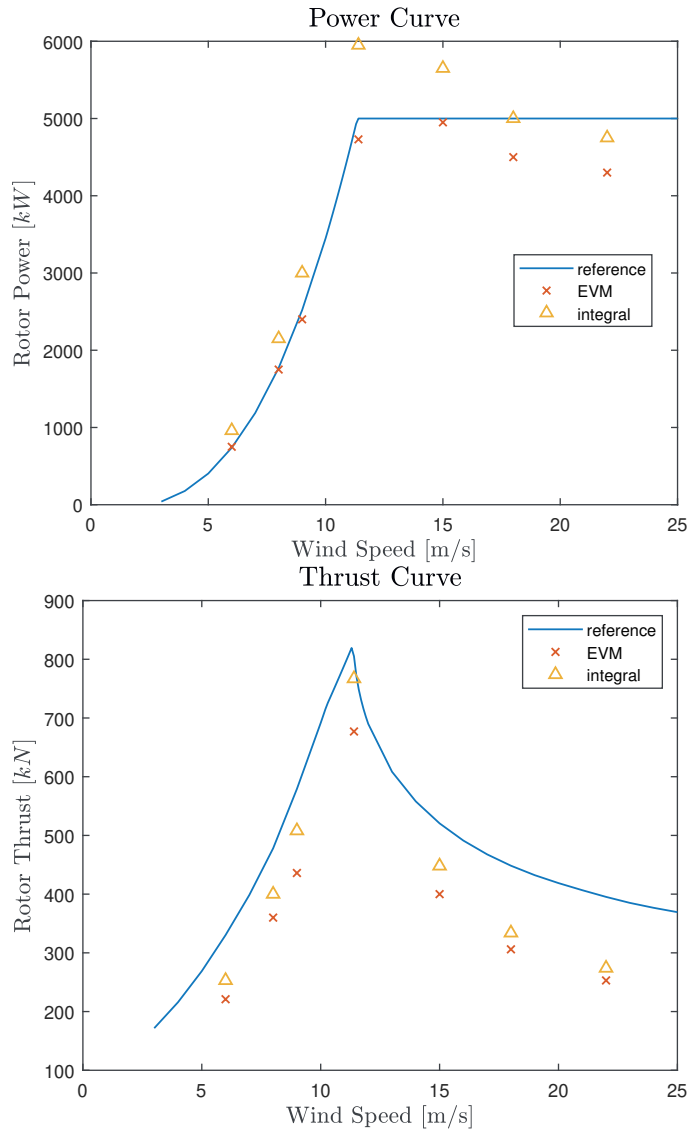


Figure 32: Rotor power (top) and rotor thrust (bottom) values shown for different wind speeds. The blue curves are the reference ones obtained with BEM.

3.5 CONCLUSIONS

Wind farm design and control require very accurate prediction of turbine performance and wake development, and hybrid CFD-analytical models such as the actuator disk and the actuator line remain the go-to approaches to physical characterization and data retrieval for reduced-order models. However, actuator line models remain accessible only to a knowledgeable set of users because of how strongly their results depend on parameters such as the projection function width ϵ .

In this work, we have shown how a different approach to the free-stream velocity sampling can reduce this effect. The approach was validated on a well-known case and compared to the standard local sampling approach (in the cell-centered and linear variants) and the state-of-the-art integral approach (based on spatial averaging).

A study on the sensitivity of the results to the projection function width clearly shows a reduced dependency on the projection function width when using the EVM sampling. For completeness, we simulated operating conditions across the entire operational range.

The EVM consistently matches the theoretical power reference in the below-rated conditions and underestimates it for the above-rated ones. The thrust is consistently underestimated by both the EVM and the integral approach.

In 3.1.3, we introduced the notion that smearing the forces generates a viscous core in the bound vorticity. The EVM implementation could benefit from accounting for the viscous core induction. This could be done by modifying the correction for the angle of attack.

We did not perform a mesh sensitivity analysis, and this limits the validity of our claims to the considered level of discretization. It is imperative for future studies to address possible mesh dependencies.

Finally, reducing the thrust mismatch should be a priority because it directly influences the wake deficit, and an accurate description of the wake is fundamental if we want to be able to use the actuator line for control purposes.

4

A DATA-DRIVEN COMPARISON OF THE PULSE AND THE HELIX

Research is formalized curiosity. It is poking and prying with a purpose.

Zora Neale Hurston

Dynamic induction control (DIC) is a novel, exciting branch of wind farm control. It makes use of time-varying control inputs to increase wake mixing, and consequently improve the velocity recovery rate of the flow and the power production of downstream turbines. The pulse and the helix are two promising DIC strategies that rely on sinusoidal excitations of the collective pitch and individual pitch of the blades, respectively. While their beneficial effects are evident in simulations and wind tunnel tests, we do not yet fully understand the physics behind them. We perform a systematic analysis of the dynamics of pulsed and helicoidal wakes by applying a data-driven approach to the analysis of data coming from LES. Specifically, dynamic mode decomposition (DMD) is used to extract coherent patterns from high-dimensional flow data. The periodicity of the excitation is exploited by adding a novel physics informed step to the algorithm. We then analyze the power spectral density of the resulting DMD modes as a function of the Strouhal number for different pitch excitation frequencies and amplitudes. Finally, we show the evolution in time and space of the dominant modes and comment on the recognizable patterns. By focusing on the modes that contribute the most to the flow dynamics, we gather insight on what causes the increased wake recovery rate in DIC techniques. This knowledge can then be used for the optimization of the signal parameters in complex layouts and conditions.

4.1 INTRODUCTION

Wind is leading the energy transition in Europe by meeting 16% of the power demand, but the EU Commission's ambition is to get it up to 50% by 2050 [89]. As the clustering of wind turbines closer and closer together in large farms is a standard by now, wind farm control emerges as a viable option for both enhancing power production and reducing maintenance costs [6].

In recent years, strategies involving time-varying control inputs have started gaining interest from the wind energy community. The main goal of these strategies is to promote the mixing of the wake with the surrounding airflow so that the inflow to the downstream turbines has a higher energy content. An early big step in this direction was done by Goit and Meyers [19], who described a procedure for finding the optimal dynamic induction of turbines in a wind farm. However, this was done at a high computational cost and resulted in a non-smooth signal. Munters and Meyers [20] observed that the optimal thrust coefficient signal in Goit and Meyers [19] resembled a sinusoid, which simplified the optimization problem significantly while reducing the detrimental effect on loads. The same results were reproduced experimentally by Frederik *et al.* [22]. The thrust coefficient was manipulated by exciting the collective pitch of the blades with a periodic signal. This Dynamic Induction Control (DIC) technique was called the pulse because of the magnitude variation's effect on the wake shape.

In 2020, Frederik *et al.* [21, 90] presented the helix, a new concept that takes advantage of individual pitch control (IPC), historically used for load mitigation, to dynamically vary the fixed-frame tilt and yaw moment to manipulate the wake. We refer to the helix as a dynamic individual pitch control (DIPC) strategy. Preliminary tests lead to encouraging results: the helix appears to increase power production without significantly increasing the loads on the blades when compared not only to the baseline greedy case but also to dynamic induction control (DIC) as previously implemented in Munters and Meyers [20].

The pulse and the helix have been experimentally investigated in Frederik *et al.* [24] with dedicated tests performed in the boundary layer test section of the Polimi wind tunnel. Three G1 wind turbine models [17] were placed in the test section, aligned, and at a five-diameter distance from each other. In the experiments, two different inflow conditions and different DIC amplitudes and frequencies were tested. The inflow turbulence was generated via roughness elements, recreating typical onshore (low-turbulence) and offshore (high-turbulence) conditions. The downstream turbines were used as sensors to measure thrust and power. A total power increase of up to 4% was reported for the high-turbulence case. In van der Hoek *et al.* [25], pulse was applied to a single MoWiTO-0.6 model turbine [26]. In this case, the focus is on the wake, which is captured with three-dimensional particle image velocimetry (3D-particle image velocimetry (PIV)). A decrease in wake velocity deficit and increased turbulence levels were shown. It was also possible to visualize and comment on the effect of DIC on the breakdown of the tip vortices, which is strictly related to the wake re-energizing process [27]. Experimental studies of the helix were performed by Heckmeier and expanded on by van der Hoek *et al.* [28]. In this study, the considered model turbine was again the MoWiTO-0.6. The layout consisted of two aligned models at a five-diameter distance from each other. As in the previous study, 3D-PIV was used to look at the wake, and additional information was gained through the downstream turbine. In the tested conditions, the individual pitch signal affects the stability of the tip vortices system, accelerating its breakdown and increasing the entrainment of kinetic energy in the wake. On a global scale, gains reached up to 15% of the total power output. So far, not much effort has gone into understanding why these new strategies work so well. Filling this research gap requires a focus on wake dynamics.

Wakes can be described as high-dimensional, nonlinear dynamical systems characterized by multi-scale phenomena in both space and time. However complex, they often exhibit low-dimensional behavior. Wakes are the perfect example of a problem for which extensive data sequences can be readily available through computational fluid dynamics (CFD) while governing equations are complicated to grasp or formulate correctly. In these cases, a data-driven perspective can be adopted to complement more traditional model-based approaches. By applying modal decomposition techniques, we can represent the system with a number of modes that is orders of magnitude smaller than

the state dimension of the system. The most common technique used for identifying coherent structures is proper orthogonal decomposition (POD). POD determines spatial modes, which are ordered according to their energy content. It was first applied to fluid dynamics by Lumley [91]. In Rowley *et al.* [92], dynamic mode decomposition (DMD) was introduced. It is also a data-driven approach; however, unlike POD, it produces modes based on their dynamics rather than the energy content and is characterized by a single frequency. The signal is split into a triplet of purely spatial modes, scalar amplitudes, and purely temporal signals. This makes it more suitable for the identification of dominant frequencies. Its applications to fluid dynamics in general and wind energy, in particular, include diagnostic and future state prediction. Various DMD algorithms have been developed and used for pattern detection, extraction of reduced-order models (ROM), and control. For example, Sun *et al.* [93] used DMD to investigate the near wake of a two-bladed horizontal axis wind turbine, gaining insight into the evolution of the tip vortices. In Cassamo and van Wingerden (2020) [94], input-output dynamic mode decomposition (IODMD) was used to derive a ROM for yaw control, and this was extended in Cassamo and van Wingerden (2021) [95] with Koopman modes for wind farm control.

This work aims to provide insight into wakes manipulated with DIC and, in particular, into the phenomena that promote mixing. The analysis focuses on the most relevant coherent structures and their dependency on the DIC technique and excitation frequency. The exact DMD algorithm is employed for the coherent structures extraction and a novel physics informed (pi) step exploiting the periodicity of the DIC-related phenomena. The study is organized as follows: Section 4.2.1 is devoted to explaining DIC, describing the pulse and the helix. Section 4.2.2 presents the exact DMD algorithm with the extension of the pi step. Next, Section 4.3 introduces the setup of the large eddy simulations (LES). Section 4.4 provides a comparison between the baseline case (Greedy control), pulse, and helix (both clock-wise and counter-clockwise). We then study the dependency of wake dynamics on excitation frequency. Finally, we summarize our main conclusions and elaborate on possible further steps in Section 5.5.

4.2 METHODS

4.2.1 Dynamic Induction Control

Control strategies based on a dynamically varying induction factor proved to increase the power production of small to medium-sized wind farms by enhancing wake mixing. With the unbounded optimal signal found in Goit and Meyers [19], DIC was able, in numerical simulations, to increase power gains up to 21% with respect to greedy control.

The pulse

With the pulse [22], wake mixing is induced by superimposing a sinusoidal signal on a wind turbine's collective blade pitch angles. The characterization of the excitation signal is usually done in terms of Strouhal number:

$$St = \frac{f_e D}{U_\infty} \quad (24)$$

where f_e is its frequency, D is the rotor diameter and U_∞ is the free-stream velocity. In [20], Munters and Meyers found an optimal sinusoidal excitation for the thrust coefficient with an amplitude $A = 1.5$ and a Strouhal number $St = 0.25$. They also claim that, since these parameters are non-dimensional, this optimum should be robust to spacing and turbulence intensity.

The helix

The helix [21] uses IPC to dynamically manipulate the wind turbine wake with lower power production and wake velocity fluctuations compared to other DIC strategies. The pitch angles of the blades

vary with sinusoidal signals that have the same (low) frequency and amplitude with a phase offset. This results in yaw and tilt moments on the rotor that force wake meandering. The resulting velocity field is helicoidal, hence the name of the strategy. If the phase offset between tilt and yaw angles is equal to $\pi/2$, the The helix rotates in a counterclockwise (CCW) direction; if it is equal to $3/2\pi$, the helix rotates in a clockwise (CW) direction. In practice, the desired pitch signals in a rotating reference frame θ_b (one for each blade b), can be obtained with an inverse multi-blade coordinate (MBC) transformation T^{-1} , as follows:

$$\begin{bmatrix} \theta_1(t) \\ \theta_2(t) \\ \theta_3(t) \end{bmatrix} = T^{-1}(\Psi) \begin{bmatrix} \theta_0(t) \\ \theta_{tilt}(t) \\ \theta_{yaw}(t) \end{bmatrix}, \quad (25)$$

with

$$T^{-1}(\psi) = \begin{bmatrix} 1 & \cos(\psi_1) & \sin(\psi_1) \\ 1 & \cos(\psi_2) & \sin(\psi_2) \\ 1 & \cos(\psi_3) & \sin(\psi_3) \end{bmatrix}, \quad (26)$$

where the angle ψ_b is the azimuth angle for blade b, and θ_0 is the fixed-frame collective pitch. Finally:

$$\theta_b(t) = [1 \quad \cos(\psi_b) \quad \sin(\psi_b)] \begin{bmatrix} \theta_0(t) \\ \theta_{tilt}(t) \\ \theta_{yaw}(t) \end{bmatrix}, = \sin[(\omega_r + \omega_e)t + \psi_{0,b}] \quad (27)$$

where ω_r is the rotational velocity and ω_e is the one relative to the pitch excitation. For this study,

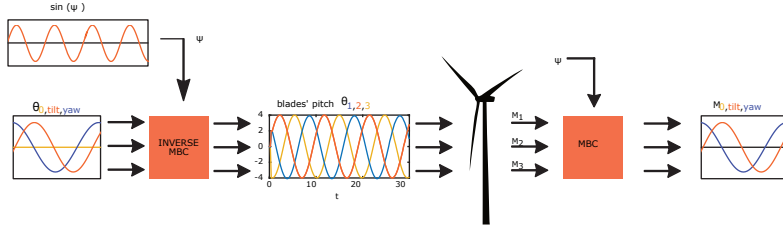


Figure 33: Schematic representation of how the multi-blade coordinate transformation is used to obtain a directional thrust force

these equations were embedded in the Simulator for Offshore Wind Farm Applications (SOWFA) supercontroller [96].

4.2.2 Physics Informed Dynamic Mode Decomposition

With DMD, we can extract key spatial invariant modes and their corresponding temporal response. This section briefly summarizes the main steps taken in the regular DMD algorithm and how knowledge related to the excitation can be incorporated into the algorithm.

The first step is to collect m snapshots of the flow field. These snapshots are representative of the state of the system at each time step, reshaped into a very tall column vector. In this paper we define this state vector as:

$$x_k = [u(t_k)^T \quad v(t_k)^T \quad w(t_k)^T \quad p(t_k)^T]^T \in \mathbb{R}^{n \times 1}, \quad (28)$$

where $u(t_k), v(t_k), w(t_k)$ represent the vectorized velocity fields in the 3 dimensions at time instance t_k , and $p(t_k)$ contains the pressure field in the whole computational domain. We can organize the snapshots into the matrices X and X' :

$$X = \begin{bmatrix} \vdots & \vdots & \vdots & \dots & \vdots \\ x_1 & x_2 & x_3 & \dots & x_{m-1} \\ \vdots & \vdots & \vdots & \dots & \vdots \end{bmatrix} \in \mathbb{R}^{n \times m-1}, \quad X' = \begin{bmatrix} \vdots & \vdots & \vdots & \dots & \vdots \\ x_2 & x_3 & x_4 & \dots & x_m \\ \vdots & \vdots & \vdots & \dots & \vdots \end{bmatrix} \in \mathbb{R}^{n \times m-1}, \quad (29)$$

with $n \in \mathbb{Z}^+$ the state dimension and $m \in \mathbb{Z}^+$ the number of snapshots. Linear DMD then finds the best linear operator that advances X into X' :

$$X' \approx AX \quad (x_{k+1} = Ax_k). \quad (30)$$

When the state dimension n is very large, it is unfeasible to deal with the full $A \in \mathbb{R}^{n \times n}$ matrix directly. The DMD algorithm substitutes it with a POD-projected matrix $\tilde{A} \in \mathbb{R}^{r \times r}$ with r the reduced state dimension. This matrix is obtained using the singular value decomposition (SVD) of X

$$X \approx U\Sigma V^*, \quad (31)$$

where $*$ denotes the complex conjugate transpose, $U \in \mathbb{C}^{n \times r}$, $\Sigma \in \mathbb{C}^{r \times r}$ and $V \in \mathbb{C}^{m \times r}$. The left singular vectors U are POD modes. The columns of U are orthogonal, so $U^*U = I$; similarly $V^*V = I$. The matrix \tilde{A} can thus be written as

$$\tilde{A} = U^*AU = U^*X'V\Sigma^{-1}. \quad (32)$$

The following step is the eigen-decomposition of \tilde{A} :

$$\tilde{A}W = W\Lambda, \quad (33)$$

where the columns of $W \in \mathbb{C}^{r \times r}$ are eigen-vectors and $\Lambda \in \mathbb{C}^{r \times r}$ is a diagonal matrix containing the corresponding eigenvalues $\lambda_k \in \mathbb{C}$. At this point we exploit the fact that we work with a periodic excitation signal to develop a physics informed DMD scheme. For presentation reasons, we will first convert the autonomous dynamic equation (43) into its continuous time equivalent:

$$\frac{dx}{dt} = \tilde{A}_c x \quad (34)$$

Next, we exploit the fact that the response contains a first-order rigid body mode (mean of the flow field) and a number of undamped second-order oscillatory modes (excitation frequency and higher harmonics). With this information, there exists a similarity matrix $T \in \mathbb{C}^{r \times r}$ such that TAT^{-1} is a structured real block diagonal matrix. The new linear operator $\hat{A}_c = T\tilde{A}_cT^{-1}$ has the same eigenvalues as \tilde{A}_c and has the following block diagonal structure:

$$\hat{A}_c = \begin{bmatrix} 0 & & & & & \\ & 0 & \omega_1 & & & \\ & -\omega_1 & 0 & & & \\ & & & 0 & \omega_2 & \\ & & & -\omega_2 & 0 & \\ & & & & \ddots & \\ & & & & & 0 & \omega_q \\ & & & & & & -\omega_q & 0 \end{bmatrix}, \quad (35)$$

where q represents the number of harmonic modes we take into account. The time-invariant modal shapes are subsequently given by:

$$[\Phi^{(0)} \quad \Phi_1^{(1)} \quad \Phi_2^{(1)} \quad \dots \quad \Phi_1^{(q)} \quad \Phi_2^{(q)}] = X'V\Sigma^{-1}WT^{-1} \in \mathbb{R}^{n \times 2q+1}, \quad (36)$$

with $\Phi_*^{(*)} \in \mathbb{R}^{n \times 1}$. This makes it possible to describe the flow from a given set of initial conditions $\alpha(t_1)$ at time instance t_1 into a response at time instance t_2 as a summation of modes:

$$\begin{bmatrix} u(t_2) \\ v(t_2) \\ w(t_2) \\ p(t_2) \end{bmatrix} = \Phi^{(0)} \alpha^{(0)}(t_1) + \sum_{i=1}^q \begin{bmatrix} \Phi_1^{(i)} & \Phi_2^{(i)} \end{bmatrix} \begin{bmatrix} \cos(\omega_i \Delta t) & \sin(\omega_i \Delta t) \\ -\sin(\omega_i \Delta t) & \cos(\omega_i \Delta t) \end{bmatrix} \begin{bmatrix} \alpha_1^{(i)}(t_1) \\ \alpha_2^{(i)}(t_1) \end{bmatrix}, \quad (37)$$

with $\Delta t = t_2 - t_1$ and $\alpha_*^{(*)}(t_1)$ the initial condition of a corresponding mode at time instance t_1 . With the normalization of the mode shapes we can now track the modal amplitudes over time: for mode 0 (the mean mode) it will be $\|\Phi^{(0)} \alpha^{(0)}\|_F$, for the second order ones it can be computed as $\sqrt{(\|\Phi_1^{(i)} \alpha_1^{(i)}(t_1)\|_F^2 + \|\Phi_2^{(i)} \alpha_2^{(i)}(t_1)\|_F^2)}$, with $\|\cdot\|_F$ the Frobenius norm.

4.3 SIMULATION

The snapshots given as input for the DMD were obtained from a LES performed in SOWFA [46] coupled to the super controller described in Fleming *et al.* [96]. The rotor is modeled with the actuator line model (ALM), an extension of the blade element momentum (BEM) method for hybrid CFD/analytical computations. The atmospheric boundary layer (ABL) flow is governed by an incompressible formulation of the Navier-Stokes (NS) equations, while the model substitutes the physical blades with body forces distributed along lines that represent them. The forces are obtained through tabulated airfoil data and projected back into the domain employing a three-dimensional smearing Gaussian function to prevent numerical issues. Its main advantage is that it drastically reduces the computational cost while maintaining high fidelity results.

For our study, we used a uniform inflow profile to isolate the effect of the pitch actuation. The wind speed at hub height was set to 9 m/s. These conditions are not representative of realistic working conditions in an actual wind farm, but they are perfectly suited to visualize the effects of DIC on the wake. The considered rotor is the DTU 10 MW reference turbine [43], which has a diameter of 178.3 m. The simulated time is 2000 s but, for our snapshots, we discard the transient part, corresponding to the initial 400 s. The simulation time step is 0.2 s. The base mesh has the characteristics described in Table 22 and was locally refined to reach a characteristic cell dimension in the rotor area of 3.125 m. The positions of the refinements and the names of the boundaries are illustrated in figure 40. For the

Table 22: Base mesh characteristics. Direction x is stream-wise, y is vertical, z is perpendicular to x and y.

	x	y	z
domain extension	2500 m	1000 m	600 m
number of cells	50	20	12

snapshots, we further decimated the data in space by considering one out of four elements in x , y , and z .

4.3.1 ALM optimal parameters

The requirements on the parameters imposed by the use of the ALM were respected: the projection function width was set to circa twice the characteristic cell dimension, i.e. 6 m. The choice of the correct value for this parameter is of the utmost importance. The reason is quite intuitive: if a very large value is chosen, the actuator line model will appear to recover an aerodynamic power exceeding the Betz limit, and if too small a value is chosen, the predicted power will be well below measurements or BEM calculations. The number of cells along a blade was higher than 50, which guaranteed an accurate description of the tip vortices.

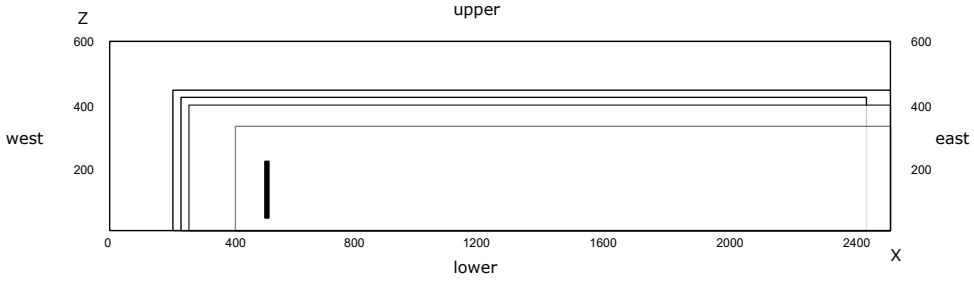


Figure 34: Vertical Slice of the domain in the uniform case, showing where the refinement zones are positioned and how the boundaries are indicated. The rotor is represented by the thick black line.

4.4 ANALYSIS

The data structure obtained from the simulation has dimensions of $96000 \times 800 \times 4$. The first dimension is space, the second time, then, for each spatio-temporal coordinate, we have collected all three velocity components and pressure. We reorganized it in column vectors that we feed to the DMD algorithm described in Section 4.2.2. The selected rank for our decomposition is 9, which means that we will obtain nine complex-conjugate eigenvalues and four modes in addition to mode 0. The choice of the rank is justified by the results in Table 23.

Table 23: Goodness of fit (FIT_{total}) of the decomposition measured through Variance Accounted For (VAF) between original and reconstructed data structure for the cases with St equal to 0.25. FIT_{out} is computed leaving that particular mode out of the reconstruction.

	FIT_{total}	$FIT_{out\ 0}$	$FIT_{out\ 1}$	$FIT_{out\ 2}$	$FIT_{out\ 3}$	$FIT_{out\ 4}$
pulse	98.08	21.55	81.52	94.26	97.79	98.08
CW-helix	98.38	25.17	77.52	95.05	97.37	98.36
CCW-helix	97.77	28.08	75.44	93.95	95.84	97.75

The sampling interval and the number of snapshots did not undergo a sensitivity analysis because, in other studies, the variation of the residual resulted to be insensitive to the former [97, 98], and to reach a plateau for the latter exactly around $m = 800$ [97].

4.4.1 Pulse and helix comparison to baseline case

In the first part of the analysis, we compare the wakes resulting from pulse, clock-wise (CW)-helix, and counter clock-wise (CCW)-helix. We consider data coming from three simulations with the setup described in Section 5.3.3. We consider a signal with 4° amplitude and St equal to 0.25 in all three cases. In Table 24, we summarize the characteristics of the found DMD modes.

First, we notice that, for the DIC cases, the frequencies associated with these modes are recognizable and definitely not surprising: modes 1, 2, and 3 are excited by the DIC signal frequency and its first and second harmonics. The frequency associated with mode 4 is the rotor frequency 1P. The modal amplitudes show that Mode 0 is always dominant. It is interesting to observe how Mode 4 seems to be insignificant for the pulse data, while for both the helix cases, its modal amplitude is higher than the one associated with Mode 3. Mode 0, being associated with zero frequency, is representative of the mean flow. We chose to represent this mode separately because it gives a more immediate visualization of the DIC techniques' effect on the recovery rate. We also plot it for the baseline case (same setup but static greedy control) in Fig. 35.

Table 24: Frequencies and individual contribution to the reconstruction given by each one of the five most relevant DMD modes.

	pulse		CW-helix		CCW-helix	
	St	Modal Amplitude	St	Modal Amplitude	St	Modal Amplitude
mode 0	0	1	0	1	0	1
mode 1	0.25	0.240	0.25	0.160	0.25	0.151
mode 2	0.5	0.130	0.5	0.092	0.5	0.083
mode 3	0.75	0.069	0.75	0.057	0.75	0.059
mode 4	2.7	0.0003	2.7	0.064	2.7	0.064

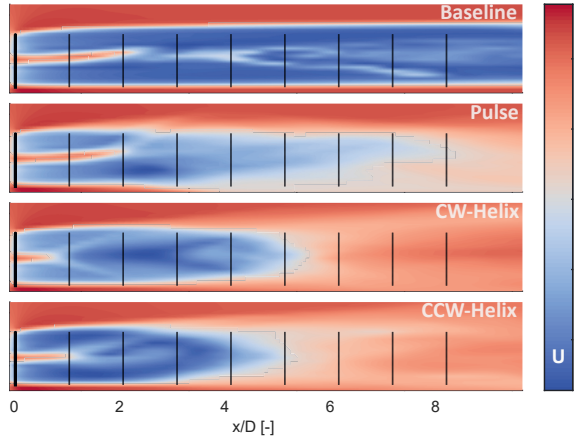


Figure 35: Vertical slices of the stream-wise velocity component, reconstructed from mode 0 as $\Phi^{(0)}\alpha^{(0)}$. From top to bottom, we have pulse, CW-helix, and CCW-helix. The free-stream velocity was 9 m/s.

The effectiveness of the three DIC techniques is immediately apparent: the wind speed in the wake for the baseline case is uniformly low (about half the free-stream velocity), and the wake itself is significantly longer than in the remaining cases. In the near wake, which is 1 to 4 diameters downstream of the turbine, we do not notice huge differences between the pulse and the CW-helix. The high-velocity zone in the hub region derives from the fact that we do not model the nacelle. Interestingly, for the CCW-helix, starting from 3D diameters downstream, an area of significantly (20%) lower wind speed appears. This area prolongs in the middle part between 4 and 6 diameters, where we start to spot bigger differences also between pulse and CW-helix. For CW-helix, the higher variability in wind speeds is representative of an enhanced mixing. At the same time, we notice that full recovery of the outer part starts earlier in the pulsed wake. The far wake is the most interesting for our purposes and in terms of differences between the DIC techniques considered. The CCW-helix is the only technique leading to recovering up to 80% of the free-stream velocity before the flow reaches a distance correspondent to five diameters downstream. Concerning the pulse, the big difference in velocity between the center of the wake and its borders suggests higher turbulence levels that would negatively affect a second turbine placed at that distance. Furthermore, the pulsed far wake is asymmetric, which could impact the loads distribution in a wind farm setting. This analysis confirms and extends what was observed in Frederik *et al.* [21].

Additional information can be given by the remaining four modes, which represent oscillations around the mean flow. We show them through iso-surfaces of velocity in Figure 36. Since we had uniform flow and no pitch actuation, the remaining modes for the baseline case are associated with

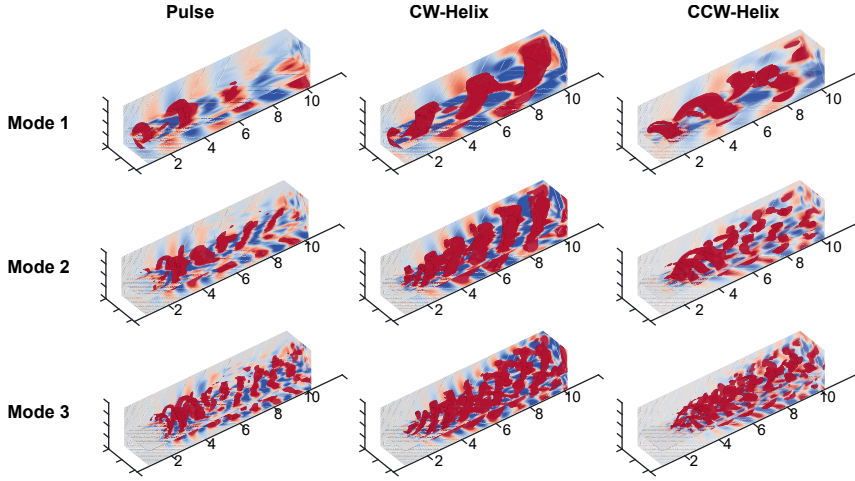


Figure 36: Iso-surfaces of the stream-wise velocity component reconstructed from modes 1, 2, and 3 (from top to bottom) as $\Phi_1^{(i)} \alpha_1^{(i)}(t_1)$ with i equal to 1,2,3 respectively. From left to right, we have pulse, CW-helix, and CCW-helix. The free-stream velocity was 9 m/s. Three slices, positioned at the left, bottom, and downstream boundaries of the domain, are added to improve visualization.

higher frequencies and have no significance for our analysis. Iso-values for Figure 36 are chosen so that they give a good visual representation of the mode, and they are different for the different modes.

The obtained tridimensional visualization of the modes gives us valuable information. First of all, we can really see how the mode shapes respectively pulsate and rotate helicoidally in alternate directions. We can also evidence how, together with harmonic growing of the frequency, the structures become closer together. An interesting feature of the helix shapes is that they seem to enlarge as they move downstream before breaking down, while for the pulse, the main structure repeats itself a few times before disassembling.

4.4.2 Pulse and CCW-helix modes dependence on Strouhal number

With the same setup described in Section 4.3 ($St = 0.25$), the pulse and CCW-helix simulations were repeated for Strouhal numbers equal to 0.2, 0.3, and 0.4. The amplitude remained unchanged and equal to 4° . This was done to assess the influence of this parameter on the mixing dynamics. The DMD analysis was performed as described in Section 4.4, and Table 25 summarizes the main findings.

Table 25: Frequencies and energy associated with the four most relevant DMD modes (after mode 0) for pulse and CCW-helix simulations at different excitation St numbers.

	Mode 1				Mode 2				Mode 3				Mode 4			
	St	Modal Amplitude			St	Modal Amplitude			St	Modal Amplitude			St	Modal Amplitude		
		pulse	CCW-helix			pulse	CCW-helix			pulse	CCW-helix			pulse	CCW-helix	
St 0.20	0.20	0.226	0.143		0.4	0.139	0.078		0.6	0.075	0.055		2.7	0.004	0.063	
St 0.25	0.25	0.240	0.151		0.5	0.130	0.083		0.75	0.069	0.059		2.7	0.0003	0.065	
St 0.30	0.30	0.243	0.158		0.6	0.119	0.082		0.9	0.059	0.055		2.7	0.001	0.065	
St 0.40	0.40	0.234	0.192		0.8	0.101	0.100		1.2	0.029	0.050		2.7	0.0009	0.065	

Again, as expected, the frequencies associated with the modes follow a very clear pattern: a mode with 0 frequency associated with the mean flow, a mode with the same frequency as the one asso-

ciated with the **DIC** signal frequency, two with higher harmonics of this same frequency and finally one related to the rotation frequency of the rotor. Plotting vertical slices of the stream-wise velocity component for mode 0 allows us to visualize the mean flow evolution in the stream-wise direction in Figure 37. Also for the other tested frequencies, the **CCW-helix** appears to be more effective in

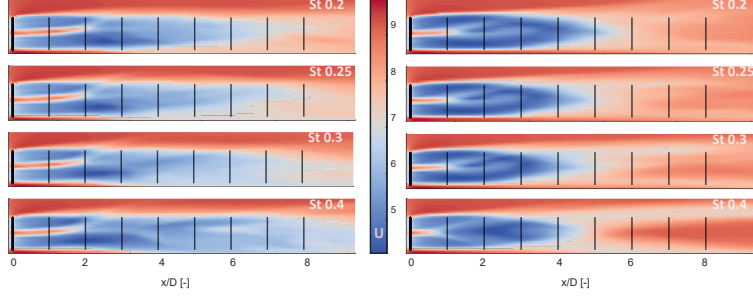


Figure 37: Vertical slices of the stream-wise velocity component reconstructed from mode 0 as $\Phi^{(0)}\alpha^{(0)}$. Slices on the left are relative to pulse simulations. Slices on the right to **CCW-helix** simulations. Each slice from top to bottom corresponds to a different St number for the excitation signal.

enhancing the mixing: immediately downstream of the rotor we have a stronger deficit but the wake is shorter. The pulse slices confirm the results of Munters and Meyers [20]: the fastest recovery is observed for $St = 0.25$. The difference with $St = 0.2$ is minimal. Interestingly, the latter has a more symmetrical wake, which could be relevant when optimizing the signal taking downstream turbines loading into account. Much more interesting is the representation of mode 0 for the **CCW-helix**, which suggests that the optimal excitation frequency for this technique is higher than for the pulse. The remaining modes are represented in Fig. 38. The frequencies follow the same pattern evidenced

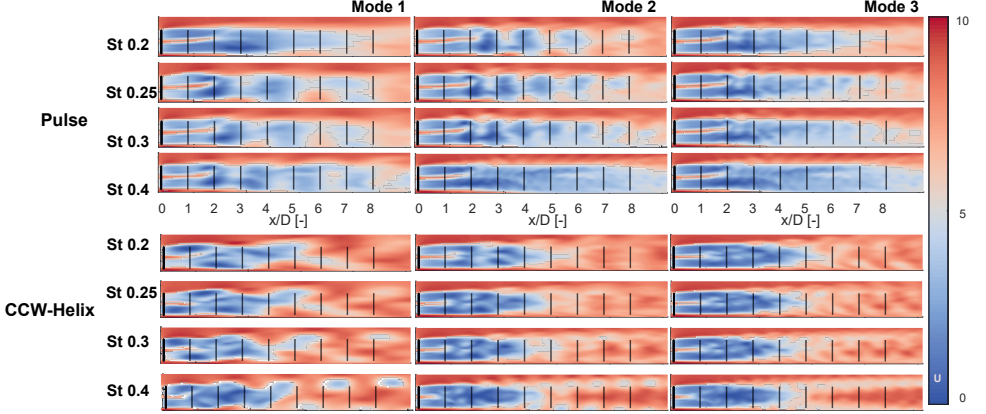


Figure 38: Vertical slices of stream-wise velocity at $y=0$, reconstructed from modes 1, 2, and 3 (from left to right) as $\Phi_1^{(i)}\alpha_1^{(i)}(t_1)$ with i equal to 1,2,3 respectively, for pulse and **CCW-helix** simulations for all of the considered St numbers.

in Section 4.4.1. When the wake breaks down we can even see how the number of distinct structures doubles from one mode to the next.

4.5 CONCLUSIONS

In this chapter, we reported the results of a numerical study aimed at characterizing the dynamic response of wakes manipulated with DIC techniques. The considered turbine was the DTU 10 MW. Its operation under a uniform inflow was simulated using the CFD framework SOWFA with the blades modeled as actuator lines. The obtained data structure was analyzed via a novel physics informed dynamic mode decomposition (pi-DMD) algorithm retrieving the five most relevant dynamic modes associated with the wake. Appropriate representations of these modal shapes were used to compare two promising DIC techniques, namely the pulse and the helix, and assess the dependence of their effectiveness in increasing the mixing on the pitch excitation frequency. As a consequence of the periodicity of the excitation signal, the frequencies associated with the three most relevant modes are the excitation frequency and its first and second harmonics. The modes associated with the helix have helicoidal shapes that enlarge as they travel downstream and have pitches proportional to the mode frequency. The CCW-helix is the technique leading to the quickest recovery to the free-stream velocity. This is consistent with the findings of Frederik *et al.* [21]. The fastest recovery for the pulse is observed for St equal to 0.25, while the helix is more effective for the highest St tested ($St = 0.4$). The higher modes give us an idea of the regions where dynamically interesting phenomena can be observed and the associated frequencies. They could guide a selection of appropriate subdomains we could limit further analysis to. Future works will extend the analysis for the helix to higher St numbers and assess the dependence on the excitation amplitude, also for simple wind farm cases.

5

AN ANALYSIS OF THE HELIX WAKE AND ITS PROPERTIES VIA DYNAMIC MODE DECOMPOSITION

It is not by prayer and humility that you cause things to go as you wish, but by acquiring a knowledge of natural laws.

Bertrand Russell

The physics behind the dynamic induction control technique known as the helix is still unclear. Its potential in a wind farm context has been proved both numerically and experimentally, but a simple helix wake model does not exist yet. We tackle this problem with a data-driven approach. Dynamic mode decomposition of data generated with large eddy simulations is performed. We simulate a 10 MW model turbine under a range of helix excitation frequencies and different inflows. We identify inflow modes related to the turbulence length scales of the inflow and helix modes related to the excitation frequency. We show that a modest number of modes allows us to reconstruct the initial flow field accurately and that the optimum excitation frequency depends on the turbulence intensity and the position of the downstream turbines.

5.1 INTRODUCTION

In the last few decades, the transition to renewable sources of energy has emerged as critical to the survival of our species on this planet. Climate change is currently the biggest threat to our societies and has already caused irreparable damage to the biosphere. Wind is a clean and abundant resource, and the technology to harness it is mature and competitive. The wind energy industry is the fastest-growing one in the renewables landscape, with big, ambitious projects being developed all over the globe [99]. Although wind is abundant, favorable locations for wind turbines are not. A proper location should not only have strong, uniform wind but also be far enough from inhabited centers and respond to logistic necessities related to transport, installation, maintenance, and connection to the grid. In this context, the strategic arrangement and clustering of wind turbines into farms play a pivotal role in maximizing efficiency [100]. When a farm perspective is adopted, wake aerodynamics becomes extremely relevant to the turbine's operation and control. The wake of a wind turbine is an area of flow characterized by lower velocity and higher turbulence intensity that extends for several diameters downstream of the turbine itself. When wind turbines are placed in clusters, the downstream turbines will easily operate in the wake of the upstream ones, with lower energy available for extraction and increased fatigue loads. This ultimately impacts the turbines' power production and their life span [101].

Wind farm control (WFC) is the branch of wind energy that studies how a certain behavior of the wind farm can be achieved from a global perspective. This means that certain turbines will perform sub-optimally but that the gain for the whole farm exceeds the individual loss. The objectives of WFC are load mitigation and power maximization. Most research focuses on the latter [102]. The two concepts currently dominating the field are based on wake redirection (WR) [103] and dynamic induction [20]. The first mainly relies on misaligning the rotor with the incoming wind direction by static yaw control. It made a first appearance in Clayton and Filby [7], was then extensively tested numerically [8, 9], on model turbines [10] and on the field [11] and is now officially on the market [12]. Dynamic induction control (DIC) is more recent and is at a different development stage. The main difference with WR (at least in its most common variant) is that dynamic control techniques have the ambition of not only adapting the turbine set-points to changes in wind direction and/or speed but rather actively affecting wake mixing and turbulence. The DIC techniques dominating the field are the pulse [20] and the helix [21]. In both cases, induction control is achieved by means of pitch actuation: collective for the pulse and individual for the helix. Recently, a lot of effort has gone into explaining how DIC affects the onset of instability and the transition from near to far wake. Croce *et al.* [104] suggested that the quicker wake re-energization through DIC techniques should be attributed to the anticipation of vortex roll-up, which occurs when the boundary layer rolls around higher vorticity cores.

In In Hodgkin, Deskos, and Laizet [105], the authors concluded that, in a fully turbulent atmospheric boundary layer (ABL) inflow, this might not be the case as the breakdown of tip vortices comes from a complex interaction across a range of excitation frequencies. Korb, Asmuth, and Ivanell [106] performed a thorough characterization and observed that the pairing and leapfrogging of vortices are not visible when a varying blade pitch is applied since the thickening and shrinking of the tip vortices rather lead to their merging. They also questioned the attribution of the power gains obtainable with the helix to the sole early wake mixing and separated the contribution of meandering, deflection, and deformation. In the aforementioned studies, wake instabilities were predicted through linear stability analysis: the Navier-Stokes equations were linearized around the base flow, and small perturbations were introduced to analyze their spatial and temporal evolution. An alternative approach consists of taking time-resolved data from experiments or numerical simulations and applying modal decomposition techniques. Some of these techniques were first developed for applications to fluid dynamics [98] and have been recently applied to wind turbines' and propellers' wakes [97]. Sarmast *et al.* [97] focused on the mutual inductance instability of the wake, using both proper orthogonal decomposition (POD) and dynamic mode decomposition (DMD) and deriving a model for determining the stable wake length. Magionesi *et al.* [107] applied POD and DMD to the wake past a marine propeller and found modes related to the coupling of tip vortices, hub-tip vortex

interaction, and wake meandering. Despite their popularity, data-driven approaches such as POD and DMD have not yet been widely applied to dynamically manipulated wakes. Understanding the mechanisms that make dynamic induction control effective in anticipating wake breakdown would benefit enormously from both the identification of dominant coherent structures and the availability of reduced order models (ROMs). The study presented in Chapter 4 [108, 109] is the first example of a data-driven approach to the modeling of helicoidal wakes: large eddy simulations (LES) data of standard, pulsed, and helicoidal wakes was fed to a physics informed dynamic mode decomposition (pi-DMD) algorithm to obtain the dominant dynamic modes in these configurations. Since the inflow was uniform, the resulting dominant modes were very clearly related to the DIC strategy adopted. In particular, the dominant modes were associated to the same Strouhal number of the helix excitation signal and its harmonics. The Strouhal number, $St = fD/u_\infty$, where f is the dominant frequency, D is a length scale (the turbine rotor diameter in our case), and u_∞ is the freestream velocity, is a dimensionless quantity often used to represent periodic flow mechanisms. We know that higher turbulence intensity of the inflow leads to faster wake recovery. In fact, inflow turbulence intensity influences the length of the near-wake and the persistence of tip vortices. With more realistic inflows, we expect the role of DIC to be smaller in the wake recovery compared to the inflow turbulence. However, how the DMD modes will change and whether they are still relevant in the wake dynamics remains an open question. The first contribution of this work is to derive a simple model for helicoidal wakes under turbulent inflow and use it to give an answer to this question.

While DMD is guaranteed to give us valuable information on the physics of the helix, some fundamental questions on wake dynamics remain open. One example is the nature of wake meandering, a low-frequency, large-scale lateral motion of the wake. Recent studies have shown that inflow turbulence and periodic perturbations (such as those introduced with DIC) interact in a complex way. Mao and Sørensen [110] performed a non-linear optimal perturbation analysis of the wake downstream of an actuator disk. They found that the optimal perturbation had the shape of an azimuthal wave in the stream-wise direction with a frequency corresponding to a $St = 0.25$. The value found in Mao and Sørensen [110] is in the range of frequencies considered optimal for DIC [20]. Forcing at this frequency led to substantial amplification of the inflow perturbation in the wake flow. Some of these studies reinforce the view of meandering as an intrinsic property of the wake flow triggered by the selective amplification of upstream disturbance. The presented view of the phenomenon contradicts the assumption at the basis of the dynamic wake meandering (DWM) model [35], which assumes that the wake acts as a passive tracer advected downstream by the mean wind. Lin and Porté-Agel [111] simulated an array of eight NREL 5MW [79] wind turbines where the first turbine was undergoing sinusoidal yaw control. The inflow had a 8% stream-wise turbulence intensity. The main finding was that the optimal power gain was obtained when the dynamic yawing triggered meandering resonance. Interestingly, similar results are shown in Li, Dong and Yang [112] for a floating offshore wind turbines (FOWT), where side-by-side motions triggered the meandering resonance. Hodgson *et al.* [113] studied the inflow turbulent time scales' effect on wake recovery, isolating their influence from the other properties such as turbulence kinetic energy, buoyancy, and shear. They found that a certain range of inflow Strouhal numbers (0.33 – 0.66) consistently results in the greatest amplification of stream-wise velocity fluctuations, regardless of whether this was the dominant component of the inflow. In light of these results, the second contribution of this work is to explore if and how the helix interacts with inflow perturbations.

In this paper, we present a data-driven analysis of helicoidal wakes under uniform and turbulent inflow conditions and provide insight into the contribution of DIC to the wake dynamics. The data is gathered through LES and a wake model is derived with DMD. We verify that DMD modes related to pitch excitation remain dominant when turbulence is introduced and show that a ROM of a helicoidal wake could be built out of as few as two modes. We demonstrate that the optimal excitation frequency is a function of the inflow and the position downstream, contrary to what was initially thought for DIC [20]. The paper structure is the following: Section 5.2 briefly presents the theory behind the helix and DMD, Section 5.3 details the flow and wind turbine models adopted and describes the setup. In Section 5.4, we show the obtained dynamic modes and elaborate on how turbulence affects the

wake physics and the efficacy of [DIC](#). Finally, we summarize our main conclusions and elaborate on possible further steps in [Section 5.5](#).

5.2 METHODOLOGY

This section describes the helix, gives a general theoretical overview of modal decomposition techniques, and presents the [DMD](#) algorithm used for this work.

5.2.1 The helix

The helix [\[21\]](#) uses individual pitch control ([IPC](#)) to dynamically manipulate the wind turbine wake with lower power production and wake velocity fluctuations compared to other [DIC](#) strategies. The pitch angles of the blades vary with sinusoidal signals that have the same (low) frequency and amplitude with a phase offset. This results in yaw and tilt moments on the rotor that force wake meandering. The resulting velocity field is helicoidal, hence the name of the strategy. If the phase offset between tilt and yaw angles is equal to $\pi/2$, the helix rotates in a counter clock-wise ([CCW](#)) direction; if it is equal to $3\pi/2$, the helix rotates in a clock-wise ([CW](#)) direction. In practice, the desired pitch signals in a rotating reference frame θ_b (one for each blade b), can be obtained with an inverse multi-blade coordinate ([MBC](#)) transformation T^{-1} , as follows:

$$\begin{bmatrix} \theta_1(t) \\ \theta_2(t) \\ \theta_3(t) \end{bmatrix} = T^{-1}(\Psi) \begin{bmatrix} \theta_0(t) \\ \theta_{tilt}(t) \\ \theta_{yaw}(t) \end{bmatrix}, \quad (38)$$

with

$$T^{-1}(\psi) = \begin{bmatrix} 1 & \cos(\psi_1) & \sin(\psi_1) \\ 1 & \cos(\psi_2) & \sin(\psi_2) \\ 1 & \cos(\psi_3) & \sin(\psi_3) \end{bmatrix}, \quad (39)$$

where the angle ψ_b is the azimuth angle for blade b , and θ_0 is the fixed-frame collective pitch. Finally:

$$\theta_b(t) = \begin{bmatrix} 1 & \cos(\psi_b) & \sin(\psi_b) \end{bmatrix} \begin{bmatrix} \theta_0(t) \\ \theta_{tilt}(t) \\ \theta_{yaw}(t) \end{bmatrix} = \sin[(\omega_r + \omega_e)t + \psi_{0,b}], \quad (40)$$

where ω_r is the rotational velocity and ω_e is the one relative to the pitch excitation. For this study,

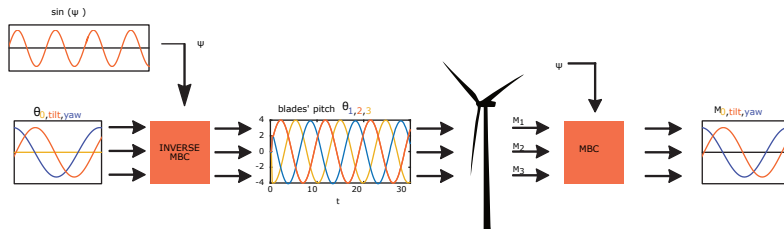


Figure 39: Schematic representation of how the multi-blade coordinate transformation is used to obtain a directional thrust force.

these equations were embedded in the SOWFA supercontroller [\[96\]](#).

5.2.2 Modal decomposition

Wind turbine wakes can be described as high-dimensional, nonlinear dynamical systems characterized by multi-scale phenomena in both space and time. However complex, they often exhibit low-dimensional behavior. This makes modal analysis techniques a very attractive option to address the complex dynamics of wakes. These techniques are data-driven, and the philosophy behind them, in general, is to reduce the order of the problem by projecting high-dimensional data onto a lower-dimensional space. This allows the extraction of coherent spatio-temporal structures that represent the system with a number of modes that is orders of magnitude smaller than its state dimension.

Among the various techniques, one that first emerged in the field of fluid mechanics is proper orthogonal decomposition (POD). POD determines spatial modes, which are ordered according to their energy content. It was first applied to fluid dynamics by Lumley [91]. Starting from the data, we can build a matrix of snapshots, each representing the system's state of interest at a given time. We normally assume that the snapshots are spaced equally in the evolution direction and that the total spatial dimension is higher than the number of snapshots (the matrix is tall and skinny). We can take the snapshot matrix and break it down into three matrices. The first contains the modes and gives us spatial information; the second gives us the mode amplitude; the third contains time information and allows us to reconstruct the dynamics. If we enforce the first matrix's orthogonality and the second's diagonality, the transformation applied is a singular value decomposition (SVD), and the modes obtained are the POD modes. Disadvantages of POD are that:

- it is sensitive to outliers;
- spacial orthogonality is not always physically significant;
- ordering by energy is not always appropriate;
- temporal dynamics is multi-frequential.

In Rowley *et al.* [92], DMD was introduced. It is also a data-driven approach; however, unlike POD, it produces modes based on their dynamics rather than the energy content and is characterized by a single frequency. The signal is split into a triplet of purely spatial modes, scalar amplitudes, and purely temporal signals. This makes it more suitable for the identification of dominant frequencies. Its applications to fluid dynamics in general and wind energy, in particular, include diagnostic and future state prediction. Various DMD algorithms have been developed and used for pattern detection [114], reduced order models (ROMs) extraction [115], and control [94].

Exact DMD algorithm

DMD is a powerful tool for tackling complex dynamical systems, particularly in domains like fluid dynamics. However, the standard algorithm has certain significant drawbacks, like susceptibility to noise and a tendency to over-fit. For this reason, many variants of the algorithm have been proposed in the literature [114]. The variant we used in this paper is exact DMD [116], which solves the issues of the standard algorithm without adding complications.

The DMD algorithm takes as input a number m of snapshots of the flow field. These snapshots can be obtained both experimentally and numerically, and they represent the state of the considered system at a certain time step. As a first step, the snapshots should be shaped into very tall columns. In our case, they will be organized as follows:

$$x_k = [u(t_k)^T \quad v(t_k)^T \quad w(t_k)^T]^T \in \mathbb{R}^{n \times 1}, \quad (41)$$

where $u(t_k)$, $v(t_k)$, $w(t_k)$ represent the vectorized velocity fields in the 3 dimensions at time instant t_k .

The series of snapshots is assembled into two matrices X and X' :

$$X = [x_1 \quad x_2 \quad x_3 \quad \dots \quad x_{m-1}] \in \mathbb{R}^{n \times m-1}, \quad X' = [x_2 \quad x_3 \quad x_4 \quad \dots \quad x_m] \in \mathbb{R}^{n \times m-1}, \quad (42)$$

with $n \in \mathbb{Z}^+$ being the state dimension and $m \in \mathbb{Z}^+$ being the number of snapshots.

DMD aims to find the best linear operator A that advances X into X' :

$$X' \approx AX \quad (x_{k+1} = Ax_k). \quad (43)$$

The DMD problem can then be formulated as:

$$\underset{\text{rank}(A)=r}{\operatorname{argmin}} \|X' - AX\|_F, \quad (44)$$

where $\|\cdot\|_F$ is the Frobenius norm.

When the state dimension n is very large, it is unfeasible to deal with the full $A \in \mathbb{R}^{n \times n}$ matrix directly. The DMD algorithm substitutes it with a POD-projected matrix $\tilde{A} \in \mathbb{R}^{r \times r}$ with r the reduced state dimension. This matrix is obtained using the Singular Value Decomposition (SVD) of X

$$X \approx U \Sigma V^*, \quad (45)$$

where $*$ denotes the complex conjugate transpose, $U \in \mathbb{C}^{n \times r}$, $\Sigma \in \mathbb{C}^{r \times r}$ and $V \in \mathbb{C}^{m \times r}$. The left singular vectors U are POD modes. The columns of U are orthogonal, so $U^*U = I$; similarly $V^*V = I$. The matrix \tilde{A} can thus be written as

$$\tilde{A} = U^*AU = U^*X'V\Sigma^{-1}. \quad (46)$$

The following step is the eigen-decomposition of \tilde{A} :

$$\tilde{A}W = W\Lambda, \quad (47)$$

where the columns of $W \in \mathbb{C}^{r \times r}$ are eigen-vectors and $\Lambda \in \mathbb{C}^{r \times r}$ is a diagonal matrix containing the corresponding eigenvalues $\lambda_k \in \mathbb{C}$. As anticipated, we now have the spatial modes (eigenvectors) and their growth/decay rates and oscillation frequencies (from the eigenvalues).

5.3 NUMERICAL ENVIRONMENT

This section presents the numerical models adopted and the simulation setups.

5.3.1 Inflow model

The ABL is simulated with SOWFA [46]. SOWFA is based on OpenFOAM [117], an open-source computational fluid dynamics (CFD) code that discretizes the Navier-Stokes (NS) equations. The representation of the rotor, described in Section 5.3.2, is non-geometric and does not require a very fine grid around the blades. This allows us to perform LES by avoiding their issues with the treatment of near-wall regions [118]. At the same time, the computational cost is maintained low. When using LES, the larger turbulent scales are simulated, while the effect of the smaller ones (the viscous subrange) is mimicked with a sub-filter-scale model. In particular, SOWFA uses a one Equation Eddy Viscosity Model for incompressible atmospheric flows. The model is based on the original *oneEqEddy* OpenFOAM model [119], but has some small modifications, such as buoyancy production, specific to atmospheric flow. Turbulent initial conditions are introduced by running precursor simulations with the atmospheric *ABL solver*. The solver allows the user to specify surface roughness, stability, wind speed, and direction. Precursor simulations are performed in a domain without the wind turbine over a time span that is sufficient for the turbulence to develop correctly. The volume field is then used to initialize the wind farm simulation (successor), and data planes are used as inflow boundary conditions.

5.3.2 Turbine Model

The rotor is modeled with the actuator line model (ALM) [44]. When considering wind turbines, the large Reynolds numbers and the multiple length scales involved make LES on a fully resolved geometry too computationally demanding to be used extensively. For this reason, hybrid methods compute the effect of the turbine on the flow analytically. ALM is an improved version of the popular actuator disk model (ADM), which is a direct descendant of Glauert's blade element momentum (BEM) [29]. With the ALM, forces exchanged between the flow and the blades are computed along lines that correspond to the individual blades. Velocities are sampled from the computational domain, and the aerodynamic coefficients are obtained from polar data. Once obtained, the forces are smeared over several cells to prevent numerical issues. Additionally, with the ALM, blades can be modeled in a way that allows them to respond dynamically to changing conditions and can account for aeroelasticity when coupled to a structural code. This allows us to describe the wake's dynamics better (with respect to ADM) and capture the tip vortices (provided that the resolution is sufficient) and their influence on the induced velocities. However, smaller-scale phenomena, such as those involving the blade boundary layer, cannot be captured.

5.3.3 Setup

The following is a description of the setup of the LES cases used to build the data set. All of the simulations have one of the three setups described below.

SPACE DISCRETIZATION For all cases, the domain is a $2.5 \times 1 \times 0.6$ km box with the specific discretization reported in Table 26 and the refinement areas illustrated in Figures 40 and 41. The uniform case discretization is the same as in Chapter 4 [108], as the same data set was used. The precursor mesh does not need a fine resolution: the turbine is not in the domain, and we just want the selected turbulent conditions to develop. Based on the literature [120], the resolution required for that to happen is in the order of 10 m. The selected dimension of a precursor cell is 12.5 m. This base mesh required only two refinements for the successor cases to reach the same resolution of the uniform ones away from the walls. Each refinement halves the characteristic dimension of the cell so that we get to $\Delta x = 3.125$ m in the rotor area. The considered rotor is the DTU 10 MW reference turbine [43], which has a diameter of $D = 178.3$ m. For all turbine simulations, $D/\Delta x = 58$. While, according to [46], $D/\Delta x = 50$ should be sufficient, in our case we do not properly capture the smaller structures in the wake (see 43). This limit was dictated by our computational resources and should be addressed in future works.

Table 26: Mesh characteristics for the three types of simulations.

	domain extension			number of cells			number of refinements	smallest cell dimension
	x	y	z	x	y	z		
uniform case	2500 m	1000 m	600 m	50	20	12	4	3.125 m
precursor	2500 m	1000 m	600 m	200	80	48	0	12.5 m
successor	2500 m	1000 m	600 m	200	80	48	2	3.125 m

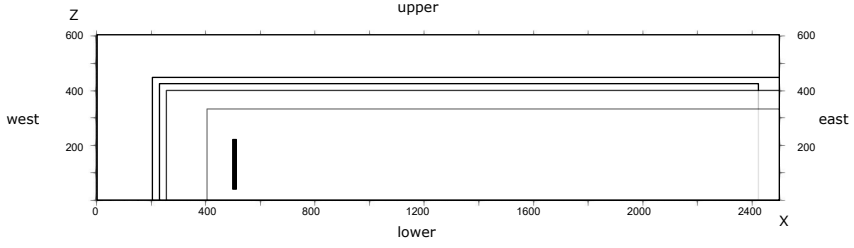


Figure 40: Vertical slice of the domain in the uniform case, showing where the refinement zones are positioned and how the boundaries are indicated. The rotor is represented by the thick black line.

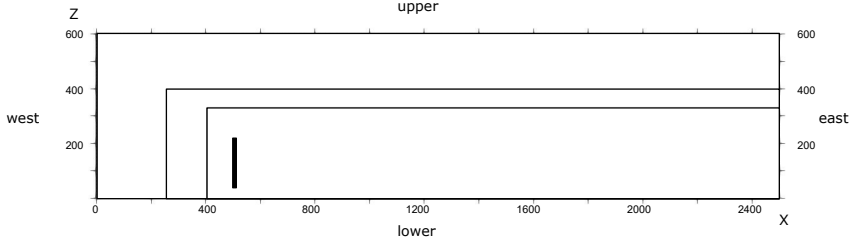


Figure 41: Vertical slice of the domain in the successor case, showing where the refinement zones are positioned and how the boundaries are indicated. The rotor is represented by the thick black line.

TIME DISCRETIZATION For the uniform case, the total simulated time is 3000 s, but for the DMD snapshots, we discarded the transient part, corresponding to the initial 1400 s. The simulation time step is 0.2 s, and a snapshot is taken once every 2 s. Our computational resources downwardly limited the time step. It respects the standard Courant–Friedrichs–Lewy number (CFL) condition but not the more stringent one normally required for actuator line simulations. The condition is formulated in Equation 48 and it indicates that the tip of the blade should not cross more than a cell over a time step.

$$CFL_{tip} = \frac{\omega R \Delta t}{\Delta_g} < 1 \quad (48)$$

where ω is the wind turbine rotational speed, R is the blade radius and $\Delta_g = \sqrt[3]{\Delta_x \Delta_y \Delta_z}$ is the equivalent cell dimension. In our case $CFL_{mean} = 0.25$ and $CFL_{tip} = 10$. We deem this to be acceptable since we are not properly modeling the tip-vortices anyway. The precursor needs to run for a long time before the data planes for the successor can be sampled. The total duration of our precursor was 33000 s with a time step of 0.5 s.

INITIAL AND BOUNDARY CONDITIONS The domain boundaries are reported in Table 27 and Table 28, together with the assigned boundary conditions for the main quantities. The turbine is located 500 m downstream of the inlet and in the middle between the north and south walls. Some of the boundary conditions might require further explanation. With *fixed flux pressure*, the pressure gradient is set in a way such that the velocity boundary condition specifies the flux on the boundary. The *inletOutlet* condition is equivalent to the *zero gradient* one, but it switches to a *fixed value* in case of backward flow.

For this study, two precursors were considered. The simulated ABL is neutral in both cases, meaning that shear is the dominant phenomenon, and the parameter affecting the turbulence the most is the roughness length z_0 . The velocity is controlled through a uniform pressure gradient such that the wind speed at hub height is 9 m/s. The inflow wind profile is logarithmic, and the potential temperature is set using a capping inversion width of 100 m, a reference potential temperature of

Table 27: Boundary conditions for the precursor

patch	U	p	T	k	nu
lower	ABL wall function	fixed flux	zero gradient	zero gradient	fixed value
upper	slip	fixed flux	fixed gradient	zero gradient	fixed value
west	cyclic	cyclic	cyclic	cyclic	cyclic
east	cyclic	cyclic	cyclic	cyclic	cyclic
north	cyclic	cyclic	cyclic	cyclic	cyclic
south	cyclic	cyclic	cyclic	cyclic	cyclic

Table 28: Boundary conditions for the successor

patch	U	p_{rgh}	T, k	nu
lower	ABL wall function	fixed flux pressure	zero gradient	fixed value
upper	slip	fixed flux pressure	fixed gradient	fixed value
west	time varying mapped fixed value	fixed flux pressure	time var. mapped fixed value	zero gradient
east	inletOutlet	zero gradient	zero gradient	zero gradient
north	inletOutlet	fixed flux pressure	zero gradient	zero gradient
south	inletOutlet	fixed flux pressure	time var. mapped fixed value	zero gradient

300 K, an initial capping inversion height of 750 m, a potential temperature jump across the capping inversion of 5 K and a stable lapse rate of 3 K/km. Although the inversion height is nominally defined at 750 m, the vertical extent of the computational domain is limited to 600 m. This configuration is commonly adopted in LES of atmospheric flows to impose a stable stratification that limits the vertical development of turbulence without requiring the inversion layer to be fully resolved within the domain. The inversion influences the flow dynamics below it by damping turbulence near the top of the domain, contributing to a more realistic representation of a capped boundary layer. The same domain extent is used for both precursor and successor simulations. Turbulence is triggered using sinusoidal spanwise velocity perturbations in the first 100 m of the ABL. The Coriolis parameter is set to $4.813 \cdot 10^{-5}$ rad/s, corresponding to a latitude of 41.44. The main ABL parameters are summarized in Table 29. As turbulence is developed inside the ABL, the velocity controller slowly rotates the wind direction at geostrophic height, trying to maintain the desired magnitude and direction at the reference height. After 30000 s, the ABL height is kept constant, and turbulence statistics can be computed (see Figure 42).

Our choices resulted in a mean turbulence intensity (TI) at the hub height of 3.3% in one case and 6.5% in the other. These values are representative of the range of TI that a first-row wind turbine can experience when placed offshore. The tower is about 115 m, meaning the turbine will partially operate outside the Prandtl layer.

In the final hundred seconds of the precursors' simulations, we collected velocity data from a diameter-long vertical line of probes through the point where the hub should be and on a horizontal line from the same point in the stream-wise direction to the end of the domain. We used these data to estimate the turbulence integral length scales in these directions. The definition of the integral length scale, L , that we adopted is based on Taylor's hypothesis on frozen turbulence. With this assumption, the integral length scale at a certain position can be expressed as a function of an integral time scale at that position:

$$L(z) = U(z) \cdot T(z) \quad (49)$$

Table 29: Main ABL parameters for the precursor simulations

u_{ref} [m/s]	h_{ref} [m]	θ_0 [K]	Δ_h [m]	γ [K/km]	$H_{inversion}$ [m]	f_c [rad/s]	$z_{0,TI=3.3\%}$ [m]	$z_{0,TI=6.5\%}$ [m]
9	115	300	100	3	750	$4.813 \cdot 10^{-5}$	10^{-6}	10^{-2}

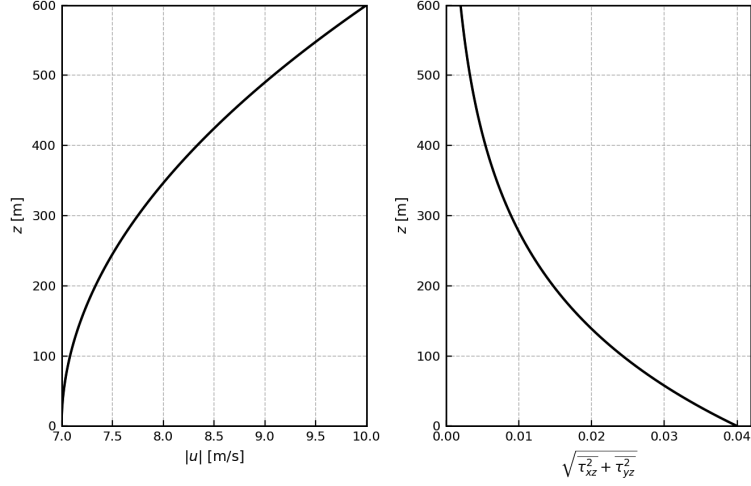


Figure 42: Precursor stream-wise velocity and shear stress profiles.

This integral time scale is calculated as follows:

$$T = \int_0^{1/e} \rho(\tau) \cdot d\tau \quad (50)$$

where $\rho(\tau)$ is the auto-correlation coefficient of the time signal of the velocity fluctuations, and e is Euler's number. Table 30 summarizes the results:

Table 30: Mean turbulence length scale in vertical and stream-wise direction in correspondence of where the hub of the turbine would be

TI	L_x [m]	L_z [m]
3.3%	345	268
6.5%	387	274

5.4 RESULTS

This study includes results from a total of 23 simulations, including 2 precursor simulations. The setup is as described in Section 5.3.3. In each of the simulations, we have a single DTU 10 MW turbine controlled with a CCW helix with amplitude 4 and frequency varying in the range $St \in [0.15, 0.2, 0.25, 0.3, 0.35, 0.4]$. This is done for three different inflow conditions: a uniform inflow and turbulent inflows with $TI = 3.3\%$ and $TI = 6.5\%$.

5.4.1 Wake Deficit Recovery

In this Section, before going into the DMD analysis, we look at instantaneous flow-field results and at the evolution of normalized global quantities in the wake. Figures 43 and 44 show a top view of the wake, for the low turbulence case, at the last step of the simulation with a comparison between baseline and helix control with $St_{exc} = 0.4$. We only show this case because it allows a clearer visualization of what happens in all cases, including the high turbulence ones. In particular, Figure 43

shows the stream-wise velocity, u , normalized by the value imposed at the rotor hub (9 m/s), and Figure 44 shows the vertical component of the velocity, v , on a same vertical plane passing through the hub.

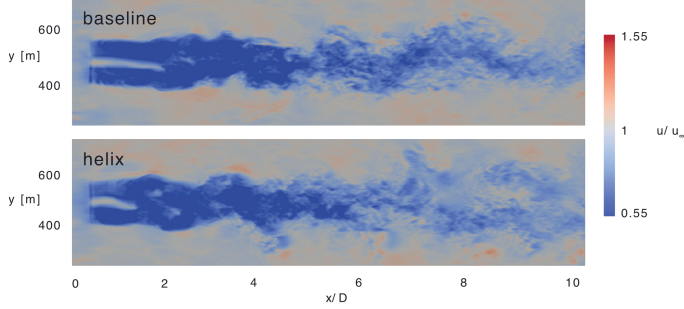


Figure 43: Horizontal snapshot of the stream-wise velocity component (u) at the final time step for baseline control (top) and for the helix with excitation St 0.4 (bottom). Turbulence intensity in both cases is 3.3%

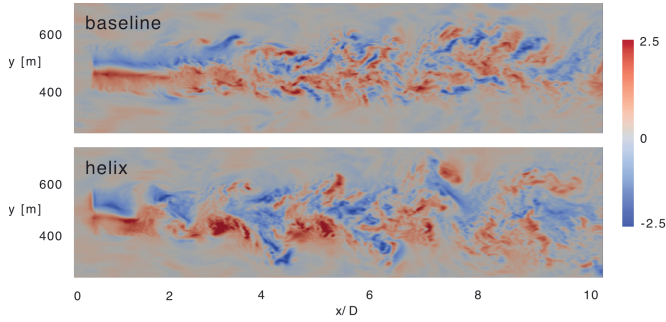


Figure 44: Horizontal snapshot of the vertical velocity component (v) at the final time step for baseline control (top) and for the helix with excitation St 0.4 (bottom). Turbulence intensity in both cases is 3.3%

We can clearly observe an earlier onset of instability in the cases where the helix control is used. We see it, in particular, from the anticipation of meandering. From Figure 44, it seems that the wake breakdown is triggered by destabilization of the hub vortex, which would be consistent with some of the literature [121]. To quantify the gains obtained by using the helix, we first looked at the global quantities for the rotor. The turbine's power output is reduced as expected since the pitch signal is suboptimal. The maximum power loss with respect to the baseline is 3.66%. This is reported in Table 31.

Table 31: Turbine power variations obtained with the helix with different inflow conditions with respect to the baseline case value corresponding with the same inflow.

	Rotor Power					
	$St = 0.15$	$St = 0.2$	$St = 0.25$	$St = 0.3$	$St = 0.35$	$St = 0.4$
Uniform Inflow	-3.66%	-3.16%	-2.71%	-2.32%	-2.04%	-1.67%
TI=3.3%	-3.24%	-3.22%	-2.95%	-2.7%	-2.34%	-2.16%
TI=6.5%	-3,58%	-3.21%	-2.94%	-2.79%	-2.58%	-2.38%

However, the helix should allow downstream turbines to compensate for the loss and increase the power at a farm level. Other studies on [DIC](#) were performed considering downstream turbines as sensors to assess the effect on the wake. Since we have only one turbine in our simulations, we introduced some "ghost" turbines. We selected planes at multiple distances downstream of the turbine and looked at what kind of inflow would be available to a turbine of the same diameter aligned with it. To do so, we considered the mean velocity on each point of the plane contained in a circle with the same diameter as the turbine, averaged it in space, and elevated it to the power of three. We will refer to this quantity as "power available" because, for the scope of our analysis, we are interested in trends and ratios and do not need an exact value.

Figure 45 shows the power available at the different considered locations for the baseline case compared to the helix cases at different Strohual numbers, normalized by the rotor power for the baseline case. For uniform inflow, the further downstream we move, the more effective the helix proves in

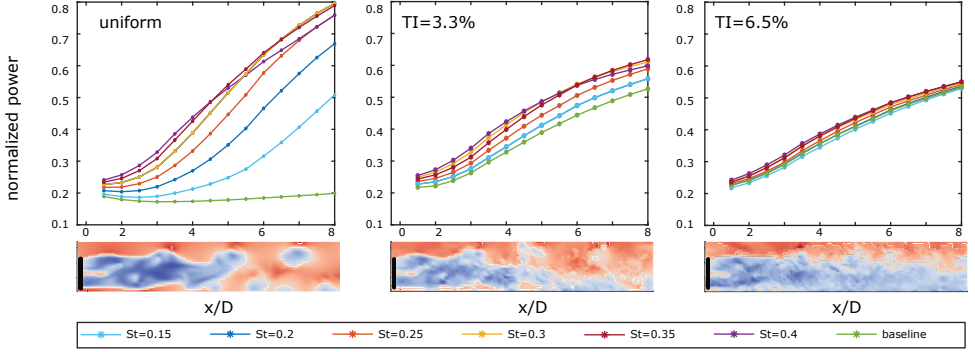


Figure 45: Available power estimate at different locations downstream of the rotor for all cases. From left to right, we show the uniform case, the low turbulence intensity case, and the high turbulence intensity case. Underneath the plots, we show vertical slices of stream-wise velocity from the case with $St = 0.4$ for illustrative purposes.

recovering energy. In the range $St \in [0.3 - 0.4]$ the lines come closer together with the optimum recovery depending strongly on the position after about four and a half diameters downstream. With turbulent inflow, the advantage obtained in the near-wake is more or less retained until the end of our sampling box. We believe that the saturation occurs when the forcing introduced by the helix is not contributing to the mixing and additional turbulent kinetic energy gets dissipated. The observation on the gain saturation in the range remains true for the low turbulence intensity case. We do not see the same behavior for the high turbulence intensity case because there is no clear phase where the forcing dominates so no transition to the near-equilibrium between mixing and dissipation. Interestingly, the trend we observe for the CCW-helix is the opposite of what is typically seen with the pulse strategy, where lower frequencies tend to be more effective. A possible explanation is that, while the pulse modulates induction in a more symmetric way and benefits from slower forcing, the CCW-helix introduces directional forcing (in yaw and tilt) that likely needs a higher frequency to effectively trigger lateral instabilities and wake meandering. At low St , that effect might simply be too weak to make a difference.

In the uniform inflow case, the gains are much higher, which was expected since, in the other cases, the most important factor in the recovery is the inflow turbulence. However, the gains obtained in the turbulent cases when using the helix would be very significant in a real wind farm scenario. One general conclusion can be drawn from this analysis: the optimal Strohual number for the helicoidal excitation depends on both the turbulence intensity and the position downstream.

The slices in Figure 46 are parallel to the rotor plane and show the mean stream-wise velocity at the "ghost" turbines positions at $St_{exc} = 0.4$. We can observe how the flow evolves depending on the inflow: the stream-wise velocity outside of the rotor area is higher than the free-stream for the

turbulent cases because the inflow profile is such that the free-stream value is imposed only at hub height. In the near-wake, the closer we are to the wake center, the higher the deficit. At a distance of 6 and 8 diameters downstream of the turbine, that area presents a higher stream-wise velocity for the uniform case.

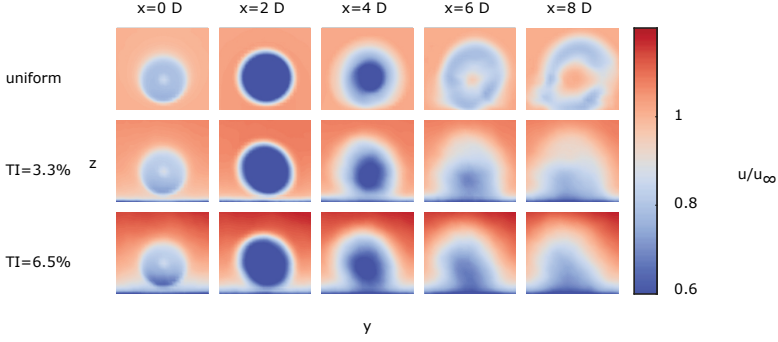


Figure 46: Mean stream-wise velocity immediately downstream of the rotor plane and at parallel planes at various distances downstream for all inflow conditions and $St_{exc} = 0.4$.

5.4.2 Dynamic mode decomposition analysis

The data structure obtained from the simulations has dimensions of $96000 \times 800 \times 3$. The first dimension is space, the second is time, and then, for each spatio-temporal coordinate, we have collected all three velocity components. This choice of observables is the same as in Chapter 4 [109]. What was found, in that case was that the results were the same with the three velocity components or with the stream-wise only (because of the uniform horizontal inflow), but spurious modes appeared when also considering the pressure. We reorganized the data in column vectors that we feed to the **DMD** algorithm.

Uniform case

The selected rank for our decomposition is $r = 15$. This results in seven modes. One mode always has zero frequency and is representative of the mean flow. In the following, we will call this mode M . We evaluated the model accuracy by computing the relative root mean square error (RRMSE) in the range $r \in [1, 181]$ as shown in Figure 47.

The RRMSE is a normalized measure of the differences between values predicted by a model and the measurements. In our case, it is calculated based on the element-wise residuals between the true snapshot matrix \mathbf{X}' and its reconstruction $\mathbf{X}'_{DMD,ij}$:

$$RRMSE = \sqrt{\frac{\frac{1}{nm} \sum_{i=1}^n \sum_{j=1}^m (\mathbf{X}'_{ij} - \mathbf{X}'_{DMD,ij})^2}{\sum_{i=1}^n \sum_{j=1}^m (\mathbf{X}'_{ij})^2}} \quad (51)$$

We see that the error strongly depends on the excitation. This is because, since the helix is more effective at higher frequencies, the helicoidal modes, whatever the rank, retain more energy content than would otherwise be more widely distributed.

Frequencies and amplitudes of the uniform inflow complex conjugate modes are represented in Figure 48. The first and most important mode always has the same frequency as the imposed helix signal. The other modes have frequencies that are harmonics of the first. In the following, we will be indicating these modes as H_1 for the first helix modes and H_n for the harmonics (where n is the relative integer multiple). The amplitude can be related to the total energy content in the considered

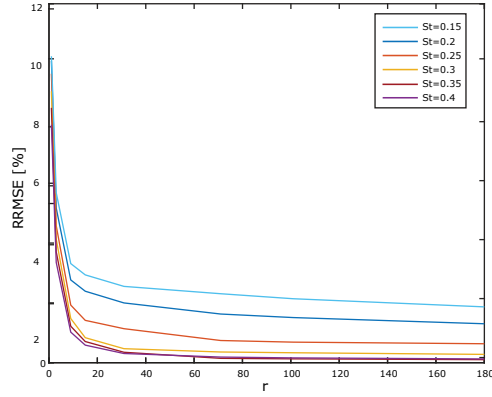


Figure 47: Relative root mean square error when modeling the flow with DMD as a function of the chosen rank. Different lines represent different Strouhal numbers of the excitation signal.

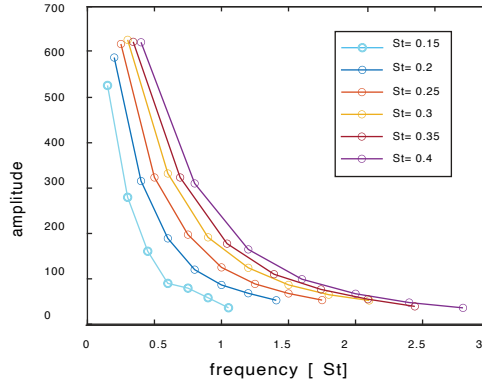


Figure 48: Spectral representation of the modes for all the uniform inflow helix cases

volume. As seen in Section 5.4.1, the optimum Strouhal also depends on the stream-wise position. Figure 49 shows iso-surfaces of the stream-wise velocity component reconstructed from the first three helix modes. The iso-values for Figure 49 are chosen so that they give a good visual representation

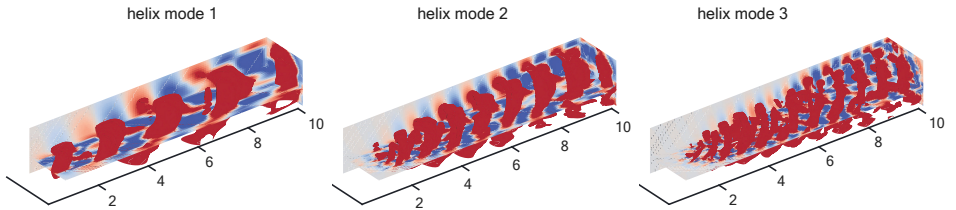


Figure 49: Iso-surfaces of the stream-wise velocity component reconstructed from modes H_1 , H_2 , and H_3 (from left to right). The free-stream velocity was 9 m/s. Three slices, positioned at the left, bottom, and downstream boundaries of the domain, are added to improve visualization.

of the mode, and they are different for the different modes. We of course recognize the helicoidal pattern and evidence how, together with harmonic growing of the frequency, the structures become

closer together. Figure 50 gives us an idea of the reconstruction quality obtainable with just the mean and the first helix mode in the uniform case.

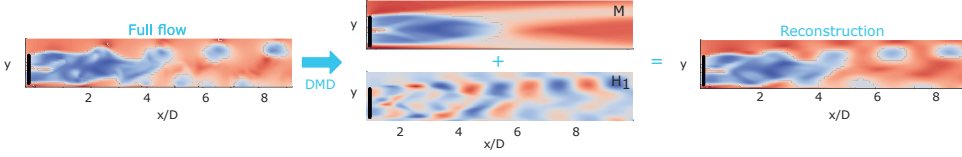


Figure 50: Representation of the reconstruction obtained with only mode 0 and more 1 for the uniform case with $St=0.4$

The information conveyed by Figure 50 can be quantified using the same criterion chosen to select the DMD rank. With the rank being fixed to 15, we evaluated the error using different modes for reconstruction. Figure 51 shows the results of this evaluation.

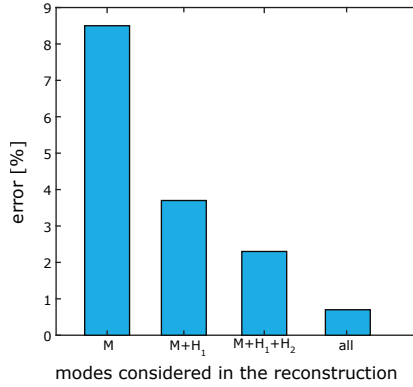


Figure 51: Relative root mean square error when modeling the flow with DMD with only selected modes. Mode 0 (M) is always present since it represents the mean.

Turbulent case

In this section, we finally address the two main research questions: do helix modes still show up in low-rank DMD of a turbulent inflow wake? Can we establish if the helix triggers wake meandering as inflow perturbations with similar frequencies to Mao and Sørensen [110] and Li, Dong and Yang [112]?

In turbulent cases, as expected, the quality of the reconstruction is lower. The energy associated with the complex modes is several orders of magnitude lower than the one associated with mode 0. This does not mean the helicoidal mode cannot contribute significantly to the dynamics. Given an excitation frequency, the error remains constant in the range of ranks tested for the uniform case $r \in [1, 181]$. The error varies from a minimum of 7.6% for $St=0.4$ to a maximum of 8.1% for $St=0.2$. For consistency with the uniform case, we picked $r=15$ again.

To isolate the effect of turbulence, we first performed DMD on the precursor simulations. Because of the coarser mesh, the data structure is considerably smaller, namely $96000 \times 300 \times 3$.

For both precursors, the dominant frequency ($St=0.072$) is related to the vertical integral length scale found for the precursors, as shown in Section 5.3.3. The other dominant frequencies are the first and second harmonic. In the following, as done for the helix modes, we will refer to these modes as I_1 for the first inflow mode and I_n for the harmonics (where n is the relative integer multiple). The frequency related to the stream-wise integral length scale is also present but is not dominant. These

modes are still relevant for the successors: we find them again in addition to the helix-related modes. Although we expected to find the precursor modes (we already know that turbulence dominates the flow field), whether the helix modes would still be relevant was an open question. From figure 52, we can observe how the turbulence intensity modifies the amplitude of the modes and their spacial decay but not their frequencies.

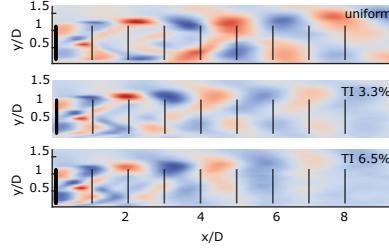


Figure 52: Vertical slices of the stream-wise velocity component, reconstructed from the first helix mode for the uniform case and the two turbulent cases with $St_{exc}=0.3$. The frequency of this mode is also $St=0.3$.

In general, the exact **DMD** modes follow a predictable pattern for turbulent cases, given an excitation frequency and the precursor characteristics. One or more zero frequency modes over which the mean flow is distributed, one mode at the dominant precursor frequency with some of its harmonics (inflow modes), and one mode at the excitation frequency with some of its harmonics (helix modes).

Figures 53 and 54 show the flow reconstruction obtainable with only the mean flow and the helix mode for the case with $St=0.4$ at both turbulence intensities. As already mentioned, the quality is significantly lower with respect to the uniform case (See Figure 50), but the first helix mode is still dominating the dynamics. Any attempt at reconstructing the full flow that does not include it is indistinguishable from the mean.

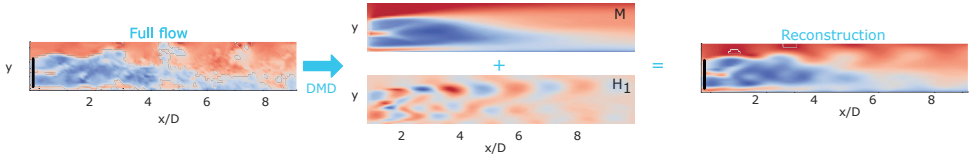


Figure 53: Representation of the reconstruction obtained with only mode 0 and the first helix mode for the case with $St = 0.4$ and $TI=3.3\%$

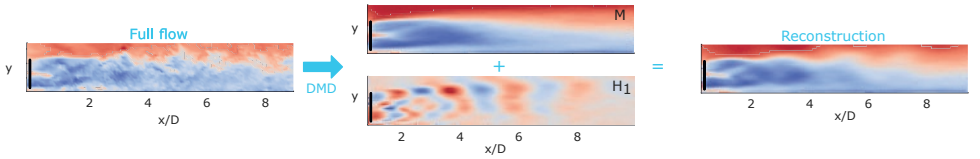


Figure 54: Representation of the reconstruction obtained with only mode 0 and the first helix mode for the case with $St = 0.4$ and $TI=6.5\%$

The information conveyed by Figure 53 and Figure 54 can be quantified using the same criterion chosen to select the **DMD** rank. With the rank being fixed to 15, we evaluated the error using different modes for reconstruction. Figure 55 shows the results of this evaluation.

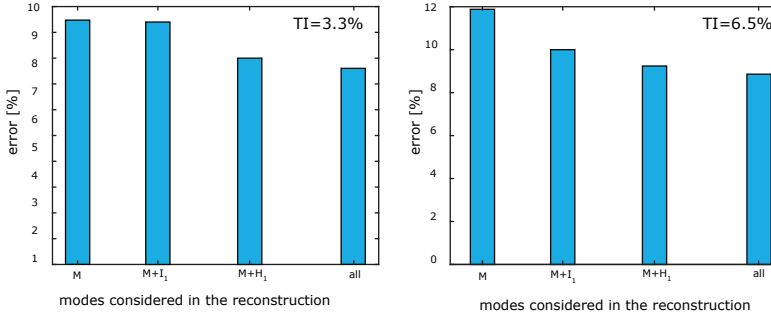


Figure 55: Relative root mean square error for the turbulent cases with $St=0.4$ when modeling the flow with **DMD** with only selected modes. Mode 0 (M) is always present since it represents the mean.

5.5 CONCLUSIONS

In this paper, we reported the results of a numerical study that characterized the dynamic response of wakes manipulated with **DIC** techniques. The considered turbine was the DTU 10 MW. Its operation under three different inflow conditions was simulated using the **CFD** framework SOWFA with the blades modeled as actuator lines.

The main finding of this study is that the helix retains its dynamic importance when a realistic value of turbulence intensity is considered. Analysing the data via an exact **DMD** algorithm, we retrieved the eight most relevant dynamic modes associated with the wake. The helix modes are still dominant. We found that the frequencies of dominant modes are associated with the turbulent length scales of the inflow and with the pitch excitation. The turbulence intensity affects their amplitudes and spatial decay. Wake energy content analysis at various downstream locations also lead to an important finding: the optimal St_{exc} for the helix varies with the turbulence intensity and the downstream position.

The found optimal St values are consistent with the observation in Hodgson *et al.* [113] that inflow Strouhal numbers in the range of $St=0.33$ to $St=0.66$ results in optimal amplification of stream-wise velocity fluctuations, but, with the current simulation setup, there is no clear relationship between the excitation frequency and the triggering of meandering as in Mao and Sorensen [110] and Li, Dong and Yang [112]. The modes obtained from **DMD** also give us a simple, linear, model the helicoidal wake. We show that a fair reproduction of the full-flow dynamics is not attainable without the first helix mode and that, in a turbulent case, a simple wake model that only takes into account the rigid mode (mean flow) and the first helix mode, which is an order reduction from infinite to two, leads to a maximum error of 3% on the reconstruction of the full flow field for uniform inflow case, and a maximum of 9% for the turbulent ones. The percentages given for the turbulent cases refer to the case with $St_{exc}=0.4$, but we do not expect big variations with St_{exc} . In the uniform case, the reconstruction error is generally much lower and more dependent on the rank of the initial decomposition and on St_{exc} .

Our recommendation for future work is to augment the space and time resolution to the point where the influence of tip vortices and their interaction with the hub vortex can be assessed. Moreover, the modes' dependency on other inflow parameters (such as turbulence length scales) needs to be assessed.

6 | CONCLUSIONS AND RECOMMENDATIONS

'T-shirt idea: "Goodbyes Stink"'

Michael Scott

The objective of this thesis was to best leverage high-fidelity modeling and data-driven techniques for the characterization of wakes manipulated with dynamic induction control. This chapter is a summary of the answers we were able to give to the three main research questions we had set up to answer.

6.1 CONCLUSIONS

The wind energy community is looking with growing interest at wind farm control strategies based on dynamic induction. When wind turbines are placed in clusters, the downstream turbines will easily operate in the wake of the upstream ones, with lower energy available for extraction and increased fatigue loads, which ultimately impacts the turbines' power production and their life span. Dynamic induction control (DIC) techniques aim not only to adapt the turbine set-points to changes in wind direction and/or speed but also to actively affect wake mixing and turbulence. Optimizing these techniques experimentally or with high-fidelity modeling is unfeasible as it would require unreasonable economic and time resources. Despite a large number of numerical and experimental tests and, as of late, linear stability analyses, incomplete knowledge of the physics of manipulated wakes prevents the community from embedding dynamic induction control into analytical control-oriented models. These models are also fundamental if a closed-loop paradigm for wind farm control is to ever be adopted. This dissertation addressed this gap with a data-driven approach to wake characterization. The main goal was formulated as follows:

Thesis goal: Development of numerical methods reliably modeling wind turbine wakes as a tool for optimized solutions of dynamic wind farm control.

Overall, our effort resulted in a better understanding of wake dynamics and the limit to which it can be linearized. We first focused on assessing the reliability of the high-fidelity tools we would use for the analysis, addressing the possibility of accounting for blade structural properties and the limitations of the actuator line model (ALM). Once a proper framework for the analysis was individuated and tested, a reduced-order model of helicoidal wakes was obtained and used for their characterization.

The first step of the dissertation was to carefully consider the necessity of accounting for the coupling of computational fluid dynamics models to computational structural dynamic ones in the framework. With turbine rotors becoming bigger and bigger, the increasing blades' flexibility will not only affect the loads but could influence the wakes as well. Fluid-structure interaction (FSI) models add to the complexity of already resource-intensive large eddy simulations (LES). In Chapter 2 we addressed the following question.

Research Question 1: When does the accuracy obtainable with a computational fluid and structural dynamics (CFD-CSD) coupling justify the increased computational cost?

We tested a FSI method based on the coupled Simulator for Offshore Wind Farm Applications (SOWFA)+ OpenFAST framework. The linear structural module of FAST (Elastodyn) was coupled to SOWFA's ALM simulations to perform the aeroelastic analysis of a wind tunnel scaled model (1 : 75) of the DTU 10 MW turbine. To obtain results representative of real-scale turbines, the structural properties were also scaled. The influence of turbine stiffness on wake flow was assessed considering a wide range of structural properties. The conclusion was , for the considered model rotor, aeroelastic effects on global performance were negligible up to about 4% tip deflection, while wake differences became more evident at larger deflections. While these results should be regarded as case-specific trends rather than general recommendations, we chose, in subsequent chapters, to omit blade flexibility, enabling a balance between accuracy and computational feasibility.

In Chapter 3, we focused on the ALM, which is a hybrid approach for high-fidelity wind turbine simulations. It is preferable to traditional fully resolved geometry simulations as it reduces the cost of computational fluid dynamics (CFD) by modeling the rotor blades (and the tower and the nacelle, if necessary) as lines for which each point represents a section of the blade that exchanges with the fluid a body force computed analytically and projected onto the domain with a projection function. In cases where dynamic phenomena are relevant, the ALM is also worth choosing over the simpler actuator disk model (ADM). In the years since it was proposed, it has become the standard

in academia. We formulated the following research question:

Research Question 2: What are the limitations of actuator line models (ALM) for wind turbines, and how can we address them?

This question stemmed from the observation that results obtained with the ALM have a strong dependence on parameters such as the width of the regularization function ϵ and on the velocity sampling method. We presented an extensive review of the actuator line model, individuating the state-of-the-art and proposing a methodology, the effective velocity model (EVM), that could advance it. The EVM was implemented in SOWFA, validated, and compared to the pre-existing approaches to velocity sampling. We showed that, by using the EVM, one of the main issues of the actuator line model, the dependency on the regularization kernel width, ϵ , is significantly reduced. The EVM consistently matched the theoretical power reference in the below-rated conditions and underestimated it for the above-rated ones. This review of the ALM methods is the last step of the methodological part of the dissertation. We decided, for the following of the thesis, to use the integral velocity sampling, as its underestimation of the thrust was less severe in our study.

In Chapters 4 and 5, SOWFA was used to create a database of uniform and turbulent simulations of the DTU 10 MW model turbine over a range of DIC excitation signals. The signal amplitude was kept constant, but we tested a set of significant frequencies and both collective and individual pitch control (so both the pulse and the helix).

As, previously mentioned, LES are computationally expensive, and they cannot be used to obtain real-time control inputs. We formulated the following research question:

Research Question 3: Can we leverage the amount of data obtainable from LES to find out how DIC works and embed this knowledge into control-oriented models?

A viable option for the characterization of manipulated wake behavior is to take time-resolved data from experiments or numerical simulations and apply modal decomposition techniques. With LES we cannot directly optimize DIC techniques, but we can easily obtain time-resolved, volumetric data. We found that with dynamic mode decomposition (DMD), we can obtain reduced-order models (ROM) for dynamically controlled wakes that can be embedded into control-oriented frameworks. In particular, we concluded that, whatever the inflow, the mean flow and one or two dynamics modes are sufficient to reconstruct the helix wake accurately enough (with a maximum relative root mean square error (RRMSE) of 8% for the turbulent cases). We were also able to show how the optimal configuration for DIC techniques varies with the turbulence intensity and the downstream position. With uniform inflow we observed again the optimum excitation frequency for the pulse ($St=0.25$) found in the literature and a higher one for the helix ($St=0.4$), in the near-wake. In the range $St \in [0.3 - 0.4]$ the gain seems to be saturated. Turbulence intensity affects the amplitudes and spatial decay of the modes, therefore it changes the optimum.

6.2 FUTURE WORKS RECOMMENDATIONS

It is in the nature of research to accompany every answer with a set of additional questions. For each chapter of the dissertation we have identified opportunities for future work. The study presented in Chapter 2 was preliminary exploration into a vast field; therefore, it had a number of limitations:

- We compared our results with experimental data collected during the UNAFLOW project, but, to consider the coupled framework validation to be completed, we would have needed sensors on the blades to actually measure deflections. Future works on the topic should be based on an ad-hoc experimental campaign.

- The non-linear structural module of OpenFAST, *Beamdyn*, was not available for coupled simulations. Future analysis should look into non-linear effects.
- The choice of avoid structural modeling in the following of the thesis was mainly dictated by the necessity to save on computational resources. Future studies should get to more precise indications of the threshold after which coupling becomes convenient. In that case it would also be worth thinking of solutions to make coupled simulations faster and more efficient.

The actuator line model has revolutionized the numerical modeling of wind turbines. Chapter 3 showed that to fully leverage its potential, we must critically reevaluate its formulation.

- The presence of a viscous core in the bound and shed vorticity of the line generated by the use of the smearing function should be considered. A future development of the EVM could consist in accounting for it in a reformulated angle correction.
- We have shown that the EVM reduces the dependency on the ϵ value. Future studies should address possible mesh dependencies introduced by the EVM itself.
- In the field of wind farm control, the priority for high-fidelity wake modeling is to reduce the thrust mismatch. It directly influences the wake deficit, and an accurate description of the wake is fundamental if we want to be able to use the actuator line for control purposes.

This thesis has shown that, although wakes are high-dimensional and nonlinear dynamical systems, for wind farm wake mixing techniques, their dynamics can be well-captured by low-dimensional linear models.

- In future works with DMD the space and time resolution should be augmented to the point where the influence of tip vortices and their interaction with the hub vortex can be assessed. This could give us a clear answer on what triggers meandering and ultimately leads to velocity deficit recovery.
- We have also clearly shown how despite the influence of turbulence intensity on the amplitude and spatial evolution of helicoidal modes, these consistently dominate the wake's dynamics. However, the modes' dependency on other inflow parameters (such as turbulence length scales) needs to be assessed for this research to contribute to engineering models.
- Data-driven models such as the one resulting from this thesis, should be used in future works to test DIC in more complex farm configurations and/or with partial wake overlap.
- DMD can and should be also applied to experimental data. Experiments could further justify the use of DIC techniques, validate our models and, with DMD, contribute to the models themselves.

BIBLIOGRAPHY

- [1] Valérie Masson-Delmotte, Panmao Zhai, Anna Pirani, Sarah L Connors, Clotilde Péan, Sophie Berger, Nada Caud, Y Chen, L Goldfarb, MI Gomis, et al. Climate change 2021: the physical science basis. *Contribution of working group I to the sixth assessment report of the intergovernmental panel on climate change*, 2(1):2391, 2021.
- [2] European Commission. State of the energy union 2023 report. Technical report, 2023.
- [3] Siemens Gamesa. Offshore wind energy. <https://www.government.nl/topics/renewable-energy/offshore-wind-energy>, 2023.
- [4] Dutch Government. Offshore wind energy. <https://english.rvo.nl/sites/default/files/2024-05/Offshore-Wind-Energy-Roadmap-April-2024.pdf>, 2024. Accessed: 2024-12-07.
- [5] NE Joukowski. Vortex theory of a rowing screw. *Trudy otdeleniya fizicheskikh nauk obshchestva lubitelei estestvoznaniya*, 16(1):1–31, 1912.
- [6] van Wingerden JW, Fleming PA, Göçmen T, Eguinoa I, Doekemeijer BM, Dykes K, Lawson M, Simley E, King J, Astrain D et al. Expert elicitation on wind farm control. In *J. of Phys.: Conf. Series*, volume 1618, page 022025. IOP Publishing, 2020.
- [7] BR Clayton and P Filby. Measured effects of oblique flows and change in blade pitch angle on performance and wake development of model wind turbines. In *Proc 4th BWEA Wind Energy Conference*, 1982.
- [8] Ángel Jiménez, Antonio Crespo, and Emilio Migoya. Application of a les technique to characterize the wake deflection of a wind turbine in yaw. *Wind energy*, 13(6):559–572, 2010.
- [9] Pieter MO Gebraad, Floris W Teeuwisse, JW Van Wingerden, Paul A Fleming, Shalom D Ruben, Jason R Marden, and Lucy Y Pao. Wind plant power optimization through yaw control using a parametric model for wake effects—a cfd simulation study. *Wind Energy*, 19(1):95–114, 2016.
- [10] Filippo Campagnolo, Robin Weber, Johannes Schreiber, and Carlo L Bottasso. Wind tunnel testing of wake steering with dynamic wind direction changes. *Wind Energy Science*, 5(4):1273–1295, 2020.
- [11] Bart M Doekemeijer, Stefan Kern, Sivateja Maturu, Stoyan Kanev, Bastian Salbert, Johannes Schreiber, Filippo Campagnolo, Carlo L Bottasso, Simone Schuler, Friedrich Wilts, et al. Field experiment for open-loop yaw-based wake steering at a commercial onshore wind farm in italy. *Wind Energy Science*, 6(1):159–176, 2021.
- [12] Siemens Gamesa. Siemens gamesa now able to actively dictate wind flow at offshore wind locations. <https://www.siemensgamesa.com/en-int/newsroom/2019/11/191126-siemens-gamesa-wake-adapt-en>, 2019. Accessed: 2018-12-06.
- [13] SH Javid, RL Hauth, TD Younkins, TW Roddoch, and PR Barnes. Method for determining how to operate and control wind turbine arrays in utility systems. Technical report, General Electric Co., Schenectady, NY (USA). Electric Utility Systems ..., 1984.

- [14] Maarten Steinbuch, WW De Boer, Okko H Bosgra, SAWM Peters, and Jeroen Ploeg. Optimal control of wind power plants. *Journal of Wind Engineering and Industrial Aerodynamics*, 27(1):237–246, 1988.
- [15] Gustav P Corten and Pieter Schaak. Heat and flux. increase of wind farm production by reduction of the axial induction. Technical report, Energy research Centre of the Netherlands, 2003.
- [16] JG Schepers and SP Van der Pijl. Improved modelling of wake aerodynamics and assessment of new farm control strategies. In *Journal of Physics: Conference Series*, volume 75, page 012039. IOP Publishing, 2007.
- [17] Filippo Campagnolo, Vlaho Petrović, Johannes Schreiber, Emmanouil M Nanos, Alessandro Croce, and Carlo L Bottasso. Wind tunnel testing of a closed-loop wake deflection controller for wind farm power maximization. In *Journal of Physics: Conference Series*, volume 753, page 032006. IOP Publishing, 2016.
- [18] Ervin Bossanyi and Renzo Ruisi. Axial induction controller field test at sedini wind farm. *Wind Energy Science*, 6(2):389–408, 2021.
- [19] Goit JP and Meyers J. Optimal control of energy extraction in wind-farm boundary layers. *J. Fluid Mech.*, 768:5–50, 2015.
- [20] Munters W and Meyers J. Towards practical dynamic induction control of wind farms: analysis of optimally controlled wind-farm boundary layers and sinusoidal induction control of first-row turbines. *Wind Energy Science*, 3(1): 409–425, 2018.
- [21] Frederik JA, Doekemeijer BM, Mulders SP and van Wingerden JW. The helix approach: Using dynamic individual pitch control to enhance wake mixing in wind farms. *Wind Energy*, 23(8):1739–1751, 2020.
- [22] JA Frederik, R. Weber, S. Cacciola, F. Campagnolo, A. Croce, C. Bottasso, and J.W. van Wingerden. Periodic dynamic induction control of wind farms: proving the potential in simulations and wind tunnel experiments. *Wind Energy Science*, 5(1):245–257, 2020. doi: 10.5194/wes-5-245-2020.
- [23] Kimura K, Tanabe Y, Matsuo Y, and Iida M. Forced wake meandering for rapid recovery of velocity deficits in a wind turbine wake. In *AIAA Scitech 2019 Forum*, page 2083, 2019.
- [24] Joeri Alexis Frederik, Robin Weber, Stefano Cacciola, Filippo Campagnolo, Alessandro Croce, Carlo Bottasso, and Jan-Willem van Wingerden. Periodic dynamic induction control of wind farms: proving the potential in simulations and wind tunnel experiments. *Wind Energy Science*, 5(1):245–257, 2020.
- [25] Daan van der Hoek, Joeri Frederik, Ming Huang, Fulvio Scarano, Carlos Simao Ferreira, and Jan-Willem van Wingerden. Experimental analysis of the effect of dynamic induction control on a wind turbine wake. *Wind Energy Science*, 7(3):1305–1320, 2022.
- [26] J Schottler, A Hölling, J Peinke, and M Hölling. Design and implementation of a controllable model wind turbine for experimental studies. In *Journal of Physics: Conference Series*, volume 753, page 072030. IOP Publishing, 2016.
- [27] LEM Lignarolo, D Ragni, C Krishnaswami, Qing Chen, CJ Simão Ferreira, and GJW Van Bussel. Experimental analysis of the wake of a horizontal-axis wind-turbine model. *Renewable Energy*, 70:31–46, 2014.

- [28] Daan van der Hoek, Bert Van den Abbeele, Carlos Simao Ferreira, and Jan-Willem van Wingerden. Maximizing wind farm power output with the helix approach—experimental validation and wake analysis using tomographic piv. *arXiv preprint arXiv:2306.12849*, 2023.
- [29] H Glauert. Aerodynamic theory: A general review of progress, volume iv, chapter division I, airplane propellers, 1963.
- [30] Jens Nørkær Sørensen and Carsten Weber Kock. A model for unsteady rotor aerodynamics. *Journal of wind engineering and industrial aerodynamics*, 58(3): 259–275, 1995.
- [31] I Katic, Jørgen Højstrup, Niels Otto Jensen, et al. A simple model for cluster efficiency. In *European wind energy association conference and exhibition*, volume 1, pages 407–410. A. Raguzzi Rome, Italy, 1986.
- [32] NREL. Nrel 2020 floris. URL<https://github.com/NREL/floris>, 2020. Accessed: 2018-12-06.
- [33] Amin Niayifar and Fernando Porté-Agel. Analytical modeling of wind farms: A new approach for power prediction. *Energies*, 9(9):741, 2016.
- [34] Majid Bastankhah, Bridget L Welch, Luis A Martínez-Tossas, Jennifer King, and Paul Fleming. Analytical solution for the cumulative wake of wind turbines in wind farms. *Journal of Fluid Mechanics*, 911:A53, 2021.
- [35] Gunner C Larsen, Helge Aa Madsen, Kenneth Thomsen, and Torben J Larsen. Wake meandering: a pragmatic approach. *Wind Energy: An International Journal for Progress and Applications in Wind Power Conversion Technology*, 11(4):377–395, 2008.
- [36] Søren Ott, Jacob Berg, and Morten Nielsen. *Linearised CFD models for wakes*. Danmarks Tekniske Universitet, Risø Nationallaboratoriet for Bæredygtig Energi, 2011.
- [37] Anders Ahlström. Influence of wind turbine flexibility on loads and power production. *Wind Energy: An International Journal for Progress and Applications in Wind Power Conversion Technology*, 9(3):237–249, 2006.
- [38] Ming-Chen Hsu and Yuri Bazilevs. Fluid–structure interaction modeling of wind turbines: simulating the full machine. *Computational Mechanics*, 50(6): 821–833, 2012.
- [39] Dong Ok Yu and Oh Joon Kwon. Predicting wind turbine blade loads and aeroelastic response using a coupled cfd–csd method. *Renewable Energy*, 70: 184–196, 2014.
- [40] M Sayed, Th Lutz, E Krämer, Sh Shayegan, and R Wüchner. Aeroelastic analysis of 10 mw wind turbine using cfd–csd explicit fsi-coupling approach. *Journal of Fluids and Structures*, 87:354–377, 2019.
- [41] Zhe Ma, Pan Zeng, and LiPing Lei. Analysis of the coupled aeroelastic wake behavior of wind turbine. *Journal of Fluids and Structures*, 84:466–484, 2019.
- [42] Steven N Rodriguez, Justin W Jaworski, and John G Michopoulos. Stability of helical vortex structures shed from flexible rotors. *Journal of Fluids and Structures*, 104:103279, 2021.
- [43] Bak C, Zahle F, Bitsche R, Kim T, Yde A, Henriksen LC, Hansen MH, Blasques JPAA, Gaunaa M and Natarajan A. The DTU 10-MW reference wind turbine. In *Danish Wind Power Research 2013*, 2013.

- [44] Jens Norkær Sørensen and Wen Zhong Shen. Numerical modeling of wind turbine wakes. *J. Fluids Eng.*, 124(2):393–399, 2002.
- [45] Wen Zhong Shen, Robert Mikkelsen, Jens Nørkær Sørensen, and Christian Bak. Tip loss corrections for wind turbine computations. *Wind Energy: An International Journal for Progress and Applications in Wind Power Conversion Technology*, 8(4):457–475, 2005.
- [46] Matthew Churchfield, Sang Lee, and Patrick Moriarty. Overview of the simulator for wind farm application (sowfa). *National Renewable Energy Laboratory*, 2012.
- [47] Martin Otto Laver Hansen, Jens Nørkær Sørensen, S Voutsinas, Niels Sørensen, and H Aa Madsen. State of the art in wind turbine aerodynamics and aeroelasticity. *Progress in aerospace sciences*, 42(4):285–330, 2006.
- [48] Jason Mark Jonkman. Modeling of the UAE wind turbine for refinement of FAST_{AD}, 2003.
- [49] Jason Mark Jonkman, Marshall L Buhl, et al. *FAST user’s guide*, volume 365. National Renewable Energy Laboratory Golden, CO, USA, 2005.
- [50] I Bayati, Marco Belloli, Luca Bernini, R Mikkelsen, and Alberto Zasso. On the aero-elastic design of the dtu 10mw wind turbine blade for the lifes50+ wind tunnel scale model. In *Journal of Physics: Conference Series*, volume 753, page 022028. IOP Publishing, 2016.
- [51] Ilmas Bayati, M Belloli, L Bernini, DM Boldrin, K Boorsma, M Caboni, M Cormier, R Mikkelsen, T Lutz, and A Zasso. Unaflo project: Unsteady aerodynamics of floating wind turbines. In *Journal of Physics: Conference Series*, volume 1037, page 072037. IOP Publishing, 2018.
- [52] HM Johlas, Luis Martinez, DP Schmidt, MA Lackner, and Matthew J Churchfield. Large eddy simulations of floating offshore wind turbine wakes with coupled platform motion. Technical report, National Renewable Energy Lab.(NREL), Golden, CO (United States), 2019.
- [53] Kelsey Shaler and Jason Jonkman. Fast. farm development and validation of structural load prediction against large eddy simulations. *Wind Energy*, 24(5):428–449, 2021.
- [54] H. Glauert. *Airplane Propellers*. Dover, New York, 1985.
- [55] Torben J Larsen, Anders M Hansen, and Thomas Buhl. Aeroelastic effects of large blade deflections for wind turbines. *Proceedings of The Science of Making Torque from Wind*, pages 238–246, 2004.
- [56] Wen Zhong Shen, Wei Jun Zhu, and Jens Nørkær Sørensen. Actuator line/navier–stokes computations for the mexico rotor: comparison with detailed measurements. *Wind energy*, 15(5):811–825, 2012.
- [57] Matthew J Churchfield, Scott J Schreck, Luis A Martinez, Charles Meneveau, and Philippe R Spalart. An advanced actuator line method for wind energy applications and beyond. In *35th Wind Energy Symposium*, page 1998. IOP Publishing, 2017.
- [58] Richard JAM Stevens, Luis A Martínez-Tossas, and Charles Meneveau. Comparison of wind farm large eddy simulations using actuator disk and actuator line models with wind tunnel experiments. *Renewable energy*, 116:470–478, 2018.

- [59] Niels Trolborg, Jens N Sorensen, and Robert Mikkelsen. Numerical simulations of wake characteristics of a wind turbine in uniform inflow. *Wind Energy: An International Journal for Progress and Applications in Wind Power Conversion Technology*, 13(1):86–99, 2010.
- [60] Luis A Martínez-Tossas, Matthew J Churchfield, and Charles Meneveau. Optimal smoothing length scale for actuator line models of wind turbine blades based on gaussian body force distribution. *Wind Energy*, 20(6):1083–1096, 2017.
- [61] Luis A Martínez-Tossas and Charles Meneveau. Filtered lifting line theory and application to the actuator line model. *Journal of Fluid Mechanics*, 863: 269–292, 2019.
- [62] Wen Zhong Shen, Jens Nørkær Sørensen, and Jianhui Zhang. Actuator surface model for wind turbine flow computations. In *Proceedings of European Wind Energy Conference and Exhibition*, volume 7. IOP Publishing, 2007.
- [63] Michael Shives and Curran Crawford. Mesh and load distribution requirements for actuator line cfd simulations. *Wind Energy*, 16(8):1183–1196, 2013.
- [64] Kaya Onur Dag. Combined pseudo-spectral/actuator line model for wind turbine applications. 2017.
- [65] H. Lamb. *Airplane Propellers*. Cambridge University Press, Cambridge, 1932.
- [66] Alexander R Meyer Forsting, Georg Raimund Pirrung, and Néstor Ramos-García. A vortex-based tip/smearing correction for the actuator line. *Wind Energy Science*, 4(2):369–383, 2019.
- [67] AR Meyer Forsting and Niels Trolborg. Generalised grid requirements minimizing the actuator line angle-of-attack error. In *Journal of Physics: Conference Series*, volume 1618, page 052001. IOP Publishing, 2020.
- [68] Vitor G Kleine, Ardeshtir Hanifi, and Dan S Henningson. Non-iterative vortex-based smearing correction for the actuator line method. *Journal of Fluid Mechanics*, 961:A29, 2023.
- [69] Eva Jost, Levin Klein, Hagen Leipprand, Thorsten Lutz, and Ewald Krämer. Extracting the angle of attack on rotor blades from cfd simulations. *Wind Energy*, 21(10):807–822, 2018.
- [70] PF Melani, F Balduzzi, L Brandetti, CJ Simão Ferreira, and Alessandro Bianchini. An experimental and numerical analysis of the dynamic variation of the angle of attack in a vertical-axis wind turbine. In *Journal of Physics: Conference Series*, volume 1618, page 052064. IOP Publishing, 2020.
- [71] Roger Bergua, Amy Robertson, Jason Jonkman, Emmanuel Branlard, Alessandro Fontanella, Marco Belloli, Paolo Schito, Alberto Zasso, Giacomo Persico, Andrea Sanvito, et al. Oc6 project phase iii: validation of the aerodynamic loading on a wind turbine rotor undergoing large motion caused by a floating support structure. *Wind Energy Science*, 8(4):465–485, 2023.
- [72] Shengbai Xie. An actuator-line model with lagrangian-averaged velocity sampling and piecewise projection for wind turbine simulations. *Wind Energy*, 24(10):1095–1106, 2021.
- [73] Paolo Schito and Alberto Zasso. Actuator forces in cfd: Rans and les modeling in openfoam. In *Journal of Physics: Conference Series*, volume 524, page 012160. IOP Publishing, 2014.

- [74] Pier Francesco Melani, Paolo Schito, and Giacomo Persico. Experimental assessment of an actuator-line simulation tool for vawts. In *Colloquium on Research and Innovation on Wind Energy on Exploitation in Urban Environment Colloquium*, pages 177–200. Springer, 2018.
- [75] Simone Mancini, Koen Boorsma, Marco Caboni, Marion Cormier, Thorsten Lutz, Paolo Schito, and Alberto Zasso. Characterization of the unsteady aerodynamic response of a floating offshore wind turbine to surge motion. *Wind Energy Science*, 5(4):1713–1730, 2020.
- [76] Simon E Gant. Reliability issues of les-related approaches in an industrial context. *Flow, turbulence and combustion*, 84:325–335, 2010.
- [77] Mattero Caccialanza and Luca Bernini. Development of the effective velocity model for wind turbines aerodynamics numerical simulation through an actuator line approach. 2014.
- [78] Carlo Luigi Bottasso, Filippo Campagnolo, Alessandro Croce, Luca Maffneni, et al. Development of a wind tunnel model for supporting research on aero-servo-elasticity and control of wind turbines. In *13th international conference on wind engineering (ICWE13)*, pages 1–8, 2011.
- [79] Jason Jonkman, Sandy Butterfield, Walter Musial, and George Scott. Definition of a 5-mw reference wind turbine for offshore system development. Technical report, National Renewable Energy Lab.(NREL), Golden, CO (United States), 2009.
- [80] Luis A Martinez-Tossas, Matthew J Churchfield, Ali Emre Yilmaz, Hamid Sarlak, Perry L Johnson, Jens N Sørensen, Johan Meyers, and Charles Meneveau. Comparison of four large-eddy simulation research codes and effects of model coefficient and inflow turbulence in actuator-line-based wind turbine modeling. *Journal of Renewable and Sustainable Energy*, 10(3):033301, 2018.
- [81] Andrei Sergeevich Monin and Aleksandr Mikhaïlovich Obukhov. Basic laws of turbulent mixing in the surface layer of the atmosphere. *Contrib. Geophys. Inst. Acad. Sci. USSR*, 151(163):e187, 1954.
- [82] Robert Mikkelsen et al. *Actuator disc methods applied to wind turbines*. PhD thesis, PhD thesis, Technical University of Denmark, 2003.
- [83] John David Albertson. *Large eddy simulation of land-atmosphere interaction*. University of California, Davis, 1996.
- [84] Marc Calaf, Charles Meneveau, and Johan Meyers. Large eddy simulation study of fully developed wind-turbine array boundary layers. *Physics of fluids*, 22(1):015110, 2010.
- [85] Pankaj Jha, Matthew Churchfield, Patrick Moriarty, and Sven Schmitz. Accuracy of state-of-the-art actuator-line modeling for wind turbine wakes. In *51st AIAA Aerospace Sciences Meeting including the New Horizons Forum and Aerospace Exposition*, page 608, 2013.
- [86] Luis A Martínez-Tossas, Matthew J Churchfield, and Stefano Leonardi. Large eddy simulations of the flow past wind turbines: actuator line and disk modeling. *Wind Energy*, 18(6):1047–1060, 2015.
- [87] P-Å Krogstad and JA Lund. An experimental and numerical study of the performance of a model turbine. *Wind Energy*, 15(3):443–457, 2012.
- [88] NREL. NREL turbine models power curve archive. https://nrel.github.io/turbine-models/NREL_5MW_126_RWT.html, 2020. [Online].

- [89] EU Commission. A european green deal, 2019.
- [90] Frederik J, Doekemeijer B, Mulders S, and van Wingerden JW. On wind farm wake mixing strategies using dynamic individual pitch control. In *J. Phys.: Conf. Series*, volume 1618, page 022050. IOP Publishing, 2020.
- [91] Lumley JL. The structure of inhomogeneous turbulent flows. *Atmospheric turbulence and radio wave propagation*, 1967.
- [92] Rowley CW, Mezić I, Bagheri S, Schlatter P and Henningson DS. Spectral analysis of nonlinear flows. *J. fluid Mech.*, 641:115–127, 2009.
- [93] Sun C, Tian T, Zhu X, Hua O and Du Z. Investigation of the near wake of a horizontal-axis wind turbine model by dynamic mode decomposition. *Energy*, 227:120418, 2021.
- [94] Cassamo N and van Wingerden JW. Model predictive control for wake redirection in wind farms: a koopman dynamic mode decomposition approach. In *2021 American Control Conf. (ACC)*, pages 1776–1782. IEEE, 2021.
- [95] Cassamo N and van Wingerden JW. On the potential of reduced order models for wind farm control: a koopman dynamic mode decomposition approach. *Energies*, 13(24), 2020. ISSN 1996-1073. doi: 10.3390/en13246513. URL <https://www.mdpi.com/1996-1073/13/24/6513>.
- [96] Fleming P, Gebraad P, van Wingerden JW, Lee S, Churchfield M, Scholbrock A, Michalakes J, Johnson K. and Moriarty P. SOWFA super-controller: A high-fidelity tool for evaluating wind plant control approaches. Technical report, National Renewable Energy Lab.(NREL), Golden, CO (United States), 2013.
- [97] Sarmast S, Dadfar R, Mikkelsen RF, Schlatter P, Ivanell S, Sørensen JN and Henningson DS. Mutual inductance instability of the tip vortices behind a wind turbine. *J. Fluid Mech.*, 755:705–731, 2014.
- [98] Schmid PJ. Dynamic mode decomposition of numerical and experimental data. *J. fluid Mech.*, 656:5–28, 2010.
- [99] Paris IEA. Iea report 2023, world energy outlook 2023. Technical report, IEA, 2023.
- [100] Vladislav Akhmatov and Hans Knudsen. An aggregate model of a grid-connected, large-scale, offshore wind farm for power stability investigations—importance of windmill mechanical system. *International Journal of Electrical Power & Energy Systems*, 24(9):709–717, 2002.
- [101] Sang Lee, Matthew Churchfield, Patrick Moriarty, Jason Jonkman, and John Michalakes. Atmospheric and wake turbulence impacts on wind turbine fatigue loadings. In *50th AIAA Aerospace Sciences Meeting including the New Horizons Forum and Aerospace Exposition*, page 540, 2012.
- [102] Johan Meyers, Carlo Bottasso, Katherine Dykes, Paul Fleming, Pieter Gebraad, Gregor Giebel, Tuhfe Göçmen, and Jan-Willem Van Wingerden. Wind farm flow control: prospects and challenges. *Wind Energy Science*, 7(6):2271–2306, 2022.
- [103] Paul Fleming, Pieter MO Gebraad, Sang Lee, Jan-Willem van Wingerden, Kathryn Johnson, Matt Churchfield, John Michalakes, Philippe Spalart, and Patrick Moriarty. Simulation comparison of wake mitigation control strategies for a two-turbine case. *Wind Energy*, 18(12):2135–2143, 2015.

- [104] Alessandro Croce, Stefano Cacciola, Mariana Montero Montenegro, Sebastian Stipa, and Roberto Praticó. A cfd-based analysis of dynamic induction techniques for wind farm control applications. *Wind Energy*, 26(3):325–343, 2023.
- [105] Amy Hodgkin, Georgios Deskos, and Sylvain Laizet. On the interaction of a wind turbine wake with a conventionally neutral atmospheric boundary layer. *International Journal of Heat and Fluid Flow*, 102:109165, 2023.
- [106] H Korb, H Asmuth, and S Ivanell. The characteristics of helically deflected wind turbine wakes. *Journal of Fluid Mechanics*, 965:A2, 2023.
- [107] Francesca Magionesi, Giulio Dubbioso, Roberto Muscari, and Andrea Di Mascio. Modal analysis of the wake past a marine propeller. *Journal of Fluid Mechanics*, 855:469–502, 2018.
- [108] C Muscari, P Schito, A Viré, A Zasso, D Van Der Hoek, and JW Van Wingerden. Physics informed dmd for periodic dynamic induction control of wind farms. In *Journal of Physics: Conference Series*, volume 2265, page 022057. IOP Publishing, 2022.
- [109] Claudia Muscari, Paolo Schito, Axelle Viré, Alberto Zasso, and Jan-Willem van Wingerden. Physics-informed data-driven reduced-order models for dynamic induction control. *IFAC-PapersOnLine*, 56(2):8414–8419, 2023.
- [110] Xuerui Mao and JN Sørensen. Far-wake meandering induced by atmospheric eddies in flow past a wind turbine. *Journal of Fluid Mechanics*, 846:190–209, 2018.
- [111] Mou Lin and Fernando Porté-Agel. Wake meandering of wind turbines under dynamic yaw control and impacts on power and fatigue. *Renewable Energy*, page 120003, 2024.
- [112] Zhaobin Li, Guodan Dong, and Xiaolei Yang. Onset of wake meandering for a floating offshore wind turbine under side-to-side motion. *Journal of Fluid Mechanics*, 934:A29, 2022.
- [113] Emily L Hodgson, Mads H Aa Madsen, and Søren J Andersen. Effects of turbulent inflow time scales on wind turbine wake behavior and recovery. *Physics of Fluids*, 35(9), 2023.
- [114] Peter J Schmid. Dynamic mode decomposition and its variants. *Annual Review of Fluid Mechanics*, 54:225–254, 2022.
- [115] Alessandro Alla and J Nathan Kutz. Nonlinear model order reduction via dynamic mode decomposition. *SIAM Journal on Scientific Computing*, 39(5): B778–B796, 2017.
- [116] Jonathan H Tu. *Dynamic mode decomposition: Theory and applications*. PhD thesis, Princeton University, 2013.
- [117] Hrvoje Jasak. Openfoam: Open source cfd in research and industry. *International journal of naval architecture and ocean engineering*, 1(2):89–94, 2009.
- [118] Wolfgang Rodi, Joel H Ferziger, Michael Breuer, Mathieu Pourquieu, et al. Status of large eddy simulation: results of a workshop. *Transactions-American Society of Mechanical Engineers Journal of Fluids Engineering*, 119:248–262, 1997.
- [119] Christopher J Greenshields et al. Openfoam user guide version 6. *The OpenFOAM Foundation*, 237:624, 2018.

- [120] Matthew J Churchfield, Sang Lee, John Michalakes, and Patrick J Moriarty. A numerical study of the effects of atmospheric and wake turbulence on wind turbine dynamics. *Journal of turbulence*, (13):N14, 2012.
- [121] Giacomo Valerio Iungo, Francesco Viola, Simone Camarri, Fernando Porté-Agel, and François Gallaure. Linear stability analysis of wind turbine wakes performed on wind tunnel measurements. *Journal of Fluid Mechanics*, 737:499–526, 2013.

ACRONYMS

FRW	fully resolved wind turbine rotor
TSR	tip-speed ratio
BEM	blade element momentum
CFD	computational fluid dynamics
CFL	Courant–Friedrichs–Lewy number
PISO	Pressure-Implicit with Splitting of Operators
NREL	national renewable energy laboratory
SOWFA	Simulator for Offshore Wind Farm Applications
FAST	Fatigue, Aerodynamics, Structures, and Turbulence
ABL	atmospheric boundary layer
CBL	convective boundary layer
SBL	stable boundary layer
ALM	actuator line model
ADM	actuator disk model
EVM	effective velocity model
CSD	computational structural dynamics
CFD-CSD	computational fluid and structural dynamics
NS	Navier-Stokes
FEM	finite elements method
LES	large eddy simulations
TI	turbulence intensity
WFC	wind farm control
WR	wake redirection
IPC	individual pitch control
DIC	dynamic induction control
CW	clock-wise
CCW	counter clock-wise
MBC	multi-blade coordinate
PIV	particle image velocimetry
FSI	fluid-structure interaction
DOFs	degrees of freedom
ROM	reduced-order models
DMD	dynamic mode decomposition
pi-DMD	physics informed dynamic mode decomposition
POD	proper orthogonal decomposition
SVD	singular value decomposition
DWM	dynamic wake meandering

CURRICULUM VITÆ

Claudia Muscari

29/05/1994 Born in Soriano Calabro (VV), Italy

EDUCATION

- 2007–
2012

High school

Liceo Scientifico "G. Berto", Vibo Valentia, Italy
- 2012–
2016

Bachelor’s degree in Mechanical Engineering

Politecnico di Milano, Milano, Italy
- 2017–
2019

Master’s degree in Energy Engineering

Politecnico di Milano, Milano, Italy
- 2019–
2024

Double Doctoral degree in Mechanical Engineering

Delft University of Technology, Delft, The Netherlands
Politecnico di Milano, Milano, Italy
Thesis title: numerical modeling of dynamically manipulated
 wind turbine wakes
Promoters: Prof. dr. J.W. van Wingerden,


LIST OF PUBLICATIONS

JOURNAL PAPERS

1. Cioffi, A., **Muscari, C.**, Schito, P., and Zasso, A.. A Steady-State Wind Farm Wake Model Implemented in OpenFAST. *Energies*, 13(23), 6158.
2. **Muscari, C.**, Giordani, R., and Schito, P. On Wind Turbine structural stiffness influence on wake flow. *Journal of Fluids and Structures*, 118, 103862.
3. Ribeiro, A. F., and **Muscari, C.** Sliding mesh simulations of a wind turbine rotor with actuator line lattice-Boltzmann method. *Wind Energy*, 2023. DOI: <https://doi.org/10.1002/we.2821>
4. **Muscari, C.**, Schito, P., Viré, A., Zasso, A. and van Wingerden, J.W. The effective velocity model: An improved approach to velocity sampling in actuator line models. *Wind Energy*, 2024, 27:5: 447-462. DOI: <https://doi.org/10.1002/we.2894>
5. **Muscari, C.**, Schito, P., Viré, A., Zasso, A. and van Wingerden, J.W. An analysis of the helix wake and its properties via dynamic mode decomposition. Submitted to *Wind Energy Science*.

CONFERENCE PAPERS

1. **Muscari, C.**, Schito, P., Viré, A., Zasso, A. and van Wingerden, J.W. Physics informed DMD for periodic dynamic induction control of wind farms. *Journal of Physics: Conference Series*. IOP Publishing, 2022. p. 022057. DOI: <https://doi.org/10.1088/1742-6596/2265/2/022057>
2. Gutknecht, J., Becker, M., **Muscari, C.**, Lutz, T. and van Wingerden, J.W. Scaling DMD modes for modeling Dynamic Induction Control wakes in various wind speeds. In: 2023 IEEE Conference on Control Technology and Applications (CCTA). IEEE, 2023. p. 574-580. DOI: <https://doi.org/10.1109/CCTA54093.2023.10252400>
3. **Muscari, C.**, Schito, P., Viré, A., Zasso, A. and van Wingerden, J.W. Physics-informed data-driven reduced-order models for Dynamic Induction Control. *IFAC-PapersOnLine* 56 (2), 8414-8419. DOI: <https://doi.org/10.1016/j.ifacol.2023.10.1036>

 Included in this thesis.

ACKNOWLEDGMENTS

I am not sure why I started a PhD. I am sure it was not because of how good a student I am. I did really well up until middle school without even trying. Then I guess that my smart attempt at teen rebellion consisted of deciding that professors were just frustrated authoritarian people who had nothing to teach me (and the fact that a few of them actually were probably didn't help). So, high school was a struggle. The bachelor was a struggle. The master was a struggle. In Italy, grades are an obsession: you compare them, retake exams at university over and over to improve them, and end up associating your self-worth with them. Another thing is that we cannot separate learning from suffering or teaching from humiliation. This is the environment that shaped me, and I did not exactly graduate with flying colours, so it was a surprise when Paolo and Alberto decided to take a bet on me, and one I will always be grateful for. So, the first acknowledgments of this long list go to them.

One instinct that has guided a lot of my life choices, was to surround myself with people I believed to be better than me. I think this instinct is intrinsically good but it means I often end up thinking I am really stupid.

When I entered the PhD office in November 2019 and met my colleagues I felt really stupid. Just to give some context, among them were Giacomo who had started in May, just back from JPL, and Luca who had already scored a paper at the IIT. I just listed achievements, but, as if it weren't enough, the people behind these achievements are truly brilliant, curious, and kind.

Very soon I convinced myself that everyone thought as little of me as I did and by January 2020, the decision to go to the office was often the outcome of a long internal debate. Then COVID came, and there was not much to debate anymore. I think that decades from now, we will still be discovering new ways in which the pandemic fucked us up. The macro-effect it had on me was that the first two years of my PhD remain quite blurry in my mind. What I remember and want to remember are the people.

Giacomo per essere stato il mio primo amico al DMECC e per le sessioni di lettura durante i weekend. Luca, orso di merda, per la musica, i video scemi le discussioni sulle serie trash. Davide, per aver provato a prepararmi un minimo ad affrontare gli studenti, e per quelle due ore di spiegazione del dannato scatolotto andate completamente sprecate. Jacopo per le chiacchierate sui nostri interessi comuni, primo su tutti, gli scrittori morti. Federico, per quelle due settimane a Reggio, i frittini, il recap di Elite, per essere un'icona di stile. Beatrice, che vorrei aver incrociato prima. E poi Simone, Carlo, Giovanni, Luigi, Nicola, Giulia, Ombretta, Lorenzo, Elia, Federico, Ivano, Qian Qian, Stefano, Antonio, Cesare, Fabio, Giuseppe e tutte le altre persone con le quali ho interagito tra il DMECC e la galleria del vento.

In August 2021, I moved to Delft, and my life changed in many ways. If I had to pick one single reason to do this all over again, it would be coming here.

For that, I want to thank Jan-Willem, who welcomed me into his group knowing I had no control background and guided me with lots of patience. I want to thank Axelle for being a much-needed role model and showing me that there are many ways of being a successful researcher and that some are compatible with prioritizing empathy. Before I go any further, now that I have mentioned all of my promoters, I wish to thank the other members of my doctoral committee: Sebastiaan, Alessandro, Simon, Dominic. Your advice and the discussions we had made my thesis better.

Lately, I have been complaining a lot about how my heart is shattered. In my first year in Delft, I would use any excuse to fly back to Milan (sorry environment). At the moment of writing this part of the acknowledgments, I am in the weird situation

of having most of my support network here but not for long. My life in Delft is not something I can ever go back to. I have been grieving it. Now I want to celebrate it, beginning with my two paranympths.

Léo, I wish you could see yourself the way I see you, and treat yourself with the same kindness you show everyone else. Thank you for always keeping me grounded. Andrea, ho una stima sconfinata della tua intelligenza, curiosità e sensibilità. Grazie per avermi reso una persona migliore in più modi di quanti ne possa elencare.

Having these two next to me at the finish line gives me courage, but many other people helped carry me there. Manoel, dude, you are such a good friend; you listen, you are caring, opening up to you is easy, and time with you is fun. Emilio, grazie per avermi aiutato a scegliere la mia bellissima chitarra, per le dimostrazioni di affetto esplosive e spontanee, per la tua sconfinata fiducia nell'umanità. The brief period with you, Andrea, Tércio (*Tércio!*) and Lars (♡) in the nameless band was real fun. I want to thank all of the (flex)aeroacoustics PhDs group, especially the veterans: Hugo, Edo, Gabriel and Fernanda. Cristina e Rossella per il rewatch di Nana, per Sanremo, per le partite di calcio. A big thank you also to all of the other people from wind energy: Sylvia, Donatella, Deepali, Likhitha, Frits, Dani, Dylan, Abhratej, Rishi, David, Guanqun, Jingna, Kiran, Mehtab, Mihir, Adhyanth, Erik, Matteo, Jelle, Ricardo, Jenna, Evert, Flavio, Oriol, Sebastiano. Thank you André for the fun time in Porto, and for our long, if a little turbulent (haha), friendship.

Abi, you are the first TU Delft person I met, in the most random situation. I really miss your cynicism and our long, deep talks. Frida, you are sweet and pure and loving and incredibly strong (a bit scarily so). Thank you for making the most delicious hot chocolate in the world. Suad, sometimes I think I am too idealistic, but then I think of you and almost feel apathetic. My idealism makes me want to set the world on fire; yours seems to make you content and give you purpose. Thank you for the movie nights, the three ingredients cake, the memes. Alex, grazie per la cura che hai degli altri, per la pasta e fagioli, la pizza, gli abbracci. Victoria for your contagious energy. Eva, for how open both your heart and mind are. Clara and Coen, for being creative and positive and fun, wish we had spent more time playing music together. Livia, per le mie prime settimane, per come mi hai accolto. Per la tua risata assurda. Sander, my kicker partner. My casa Menno people, especially Lada (simply the best flatmate EVER) and Fernando.

To the people I met at X, Evi and the community she built, Annika and Marvin, and Jun for teaching me so much, to the Vocalzz choir, to Kevin to Ata. To coffee company, my weekend home, with its armchairs and couches and its light and its people. To coffee star, for keeping me and Léo and many more alive and awake. To the Bebop.

To all of Jan-Willem's group, present and past, but with special mentions for Marcus (I am grateful for the virtual coffees and for all the times you came to me with ideas), Amr for being so encouraging and nice to me when I first arrived, Maarten, I am so sorry for the times I misspelled your name! Emanuel, for sharing my confusion about control. David, for the bands tips and for helping me move to Rotterdam, and Jonas, for the Brussels trip. Marion, whom I wish I had met sooner, for always asking how I was and wanting to hear the answer. Sebastiaan, Rogier, Mees, Daniel, Zhixin, Unai, Jean, Atin, Guido, Matteo, Tim, Bert, Uwe, Jesse and Daan, you are good researchers and very nice people. Bart Doekemeijer, who I knew to be inspiring from a distance and found to also be a genuinely good person the few times we met. Literally everyone else a DCSC, whether or not you find your name in the following list: Sam, Francesco, Giampo, Alessandro, Filippo, Rudi, Georgios, Mattia, Leila, Mo, Steven, Shahzeb, Athina, Frederik, Max, Pedro, Roger, Paul, Maarten, Lotfi, Max, Maria, David, Edoardo, Luca, Manon, Riccardo, Kim, Dimitri. Thank you Francy, Marieke, Helen, Bo, Sandra, Renate, Erica, Anna.

There are, of course, a lot of people outside of Academia that deserve my gratitude. They might not have directly contributed to the thesis but they gave me love and support, listened to complaints, took my mind off of things.

Vorrei iniziare ringraziando la maestra Mina per avermi fatto amare la matematica e dirle che la penso sempre. Il professor Carrera per avermi restituito quel briciolo di fiducia nelle mie capacità che mi serviva per provare il test al Politecnico. Gli amici di Vibo. Anna Paola, perché semplicemente non so che persona sarei se non ti avessi conosciuto. Per le ore al telefono, le passeggiate, le teorie strambe, i nomi in codice dei ragazzi che ci piacevano, i dischi e i libri che abbiamo scoperto insieme. Grazie a Marica, mia maestra Jedi, Giorgio, Stella, Davide, Valentina, Cecilia, Elisa. A Isa che ha sempre avuto il coraggio delle sue passioni, per tutte le volte che me ne ha prestato un pochino. A Susy, zia Dany, Valentina, zia Ada che son state le prime, tra le persone che mi conoscono fin da bambina, a vedermi e ad apprezzarmi come una persona adulta. A Valeria, Sandro, Cristina, Cesare, Maria. Mia cugina Angelina, per le volte che mi ha truccato, piastrato i capelli, per i top che le ho rubato, per i passaggi sulla panda a sgolarci sulle canzoni di Beyoncé, per avermi fatto vivere, seppur di riflesso, un'adolescenza normale. Mio cugino Sanny, di cui mia madre non avrebbe assolutamente dovuto fidarsi quando mi ha mandato a Milano. Gli amici dell'università. Valeria per i film brutti, i dragoni sui navigli, le serate più folli degli anni universitari, le foto dal cesso. Andre, il pelatino, il primo selezionato per quel gruppo di studio che si è disperso in fretta ma mai sciolto. Grazie per essere il mio compagno di montagna e di capatine in questura e per l'affetto, per avermi fatto conoscere quelle cuorone di Ty e Ale. Antonello, per il prog, Nietzsche e gli alieni. Per C++, ovviamente. Grazie a Carlo, per l'opera, le grigliate, le sbornie tristi e quelle felici. Tommaso, per essersi ricreduto sul mio conto. Luca per le infinite sessioni di studio in triennale, per essere stato forse l'unico che non volevo uccidere durante i progetti di fine terzo anno, per aver guidato da Zurigo per esserci al mio trentesimo compleanno (mica come Carlo). Katia, che mi aiuta a tollerare questi tre quando sono insieme. Roberto, Yuri, Lorenzo, Francesco, Luca, Alessandra. I *bambini*: Laura (piccola sac a poche, compagna di bevute, giornate di studio, pipì nei parchi, figlia della possente Cinzia, sorella di Elena la buona), Gianluca (le colazioni e i *Sabadi*), Gabri (l'uomo che contava le piastrelle), Matteo, che è stato bello ritrovare, Federico. Il Galilei, per qualche anno, è stato casa mia e voi siete stati la mia famiglia. Della gente del Galilei vorrei menzionare anche 'mbare Giuliano, Kat, Lenuccia, Attilio, Giovanni, Davide, i due Giulio, Chloe, Melania, Luca. Barbara, per la bellezza, per vederla sempre, per avermela mostrata. Emanuele, che come molti ha pensato come cazzo ci fossi finita a fare il dottorato, solo che l'ha pensato ad alta voce. Fabri e Marco, che stimo tantissimo e questa follia l'hanno anche in parte ispirata. Camillo che ci ha creduto in tempi non sospetti. Zeynep, che mi ha detto di non farlo e Gian, che mi ha detto di non darle retta. Federica, per l'empatia e la pazienza. Giulia, sei una forza della natura. Grazie per le nostre lunghissime telefonate, per avere condiviso con me le fatiche del dottorato e dell'eterosessualità, questa condanna. Emily per le pizze morte, i sushini dell'essellunga, per condividere il mio destino di andare a vivere sempre più a nord. Alberto per la montagna e le serate giochi. Gli amichetti di Monza: ma e pa Tia e Miri, quella figona di Virgi, Marti, Gino, Kler, sorella calabra, mio Virgilio in cruccolandia. My Erasmus people: Patrick, Livia, Anneke, Ala, Lolo, Sibora, Daniel, Ian, Carlos, Chichi, Mario. La gente di Colibri, il Bestiario letterario e Chiara, che senza, forse, non avrei conosciuto. Veronica, anche lei regalo di un club letterario. The people I met this past year in Hamburg, who gave me tons of encouragement and understanding in this last mile before the defence: Claudia, Eleonora, Veronica, Robin, Eric, Chris, Hoda, Mike, Debora, Fatice, Kat e Louis.

Grazie alla mia famiglia. Nonno Santo per avermi viziato, coccolato e palesemente adorato per tutto il tratto di strada che abbiamo condiviso. Quel poco di autostima che ho probabilmente la devo a lui. Nonna Sina che si è sempre assicurata che mangiassi. Nonna Maria per le nutelline. Nonno Pino che tutte le volte che

gli faccio una telefonata mi ringrazia, mi chiede dov'è che vivo adesso, mi dice che mi vuole bene e butta giù. Mamma per avermi trasmesso la passione per la lettura. Da lì viene tutto il resto: quello che so, le cose in cui credo, la curiosità di avventurarmi in posti e situazioni lontani. Se mamma mi ha dato la voglia di conoscere e capire, papà probabilmente mi ha dato quella di creare ed esprimermi. Non riesco a pensare a strumenti migliori per affrontare la vita. Oltre a questi strumenti mi hanno dato anche due mirabili compagni di viaggio. Bros, mi avete sconvolto l'esistenza ma vi voglio bene e sono stra-orgogliosa di voi.

Claudia Muscari
Delft, April 2024
Hamburg, September 2025

